Title
RF-Interconnect for High-Speed Intra/Inter Data Communications

Author
Kim, Yanghyo

Publication Date
2017

Peer reviewed|Thesis/dissertation

UNIVERSITY OF CALIFORNIA

Los Angeles

RF-Interconnect for High-Speed Intra/Inter Data Communications

A dissertation submitted in partial satisfaction of the

requirements for the degree Doctor of Philosophy

in Electrical Engineering

by

Yanghyo Kim

2017

ABSTRACT OF THE DISSERTATION

RF-Interconnect for High-Speed Intra/Inter Data Communications

by

Yanghyo Kim

Doctor of Philosophy in Electrical Engineering

University of California, Los Angeles, 2017

Mau-Chung Frank Chang, Chair

In the earlier days of the Complementary Metal Oxide Semiconductor (CMOS) industry, much effort was dedicated to the performance of device speed and number of transistors per processor core in response to Gordon Moore's law. However, the attention has gradually migrated to the system-level design, such as signaling and timing conventions for efficient data transactions. This is because the system clock speed is no longer limited by CMOS device cutoff frequencies, and the system performance becomes limited by either on- or off-chip interconnects. In order to overcome such difficulties, various ideas have been proposed including pre-distortion, equalization, and multi-level signaling. However, the burden on transferring data becomes dominant in overall system design as the demands for higher computing capabilities ever increase. My research focuses on maximizing the bandwidth efficiency by exploiting RF/Wireless techniques and minimizes the interconnect complexity. I explored 3 different hypotheses.

The first case is an on- and off-chip communication through copper wires. When a point-to-point or point-to-multi-point communication is established, the data signal experiences discontinuities through vias and connectors. Then, it affects the channel frequency response with deep notches where the signal undergoes resonances. A typical solution would equalize the channel based on the worst case notch, but the penalty is the reduced signal to noise ratio (SNR).

Instead of sacrificing SNR, I accept the channel impairments and send data where there is no such notches using RF modulation on top of baseband signal.

The second case is a short-range wireless data communication through the air. Data connectors are everywhere in our daily lives. For instance, USB connectors in computers and cell phones, HDMI connectors in monitors and TVs. The mechanical parts are not only expensive but also bulky in size. Just as in first case, the high speed signal suffers discontinuities as well. Instead of struggling with mechanical parts, the wireless interconnect utilizes the abundant free-license band at 60GHz and provides giga-bits-per second (Gb/s) data rate with a minimum complexity and power efficiency because of its nature in short-range communication.

The last one is a mid-range (1meter to 10meter) data communication through plastic cables. In an example of data server communication market, the fiber optics has been a dominant solution because of the long-distance capability and large data bandwidth. However, it requires electrical to optical, and optical to electrical conversion with a strict temperature control. Keeping the advantage of low-loss channel characteristic, modulated RF signals can propagate through plastic tubes or strips without the cost of conversion process.

The dissertation of Yanghyo Kim is approved.

Tatsuo Itoh

Jason Cong

Xiaochun Li

Mau-Chung Frank Chang, Committee Chair

University of California, Los Angeles

2017

TABLE OF CONTENTS

LIST OF FIGURES AND TABLES

Dedicated to my wife and parents

VITA

2007	Bachelor of Science in Electrical Engineering
	University of Mississippi
2010	Master of Science in Electrical Engineering
	University of California, Los Angeles

Chapter 1

RF-Interconnect Wireline Communication

1.1 Introduction

In the earlier days of the semiconductor industry, much effort was dedicated to only the performance of device speed and number of transistors per processor core (in response to Moore's scaling law). However, attention has gradually migrated to system-level design, such as signaling and timing conventions for efficient data transaction [1]. This is because the system clock speed is no longer limited by complementary–metal–oxide semiconductor (CMOS) device cutoff frequencies due to fundamental thermal limitations and the system performance becomes limited by either on- or off-chip interconnects. For instance, one system bottleneck arises from the available data rate of off-chip printed circuit board (PCB) channels [2]. As the data rate increases, the response of the wire to each frequency is different, generally with increased attenuation and phase lag for higher frequencies. This means that the voltage swing and delay are different for slow and fast changing signals, resulting in inter-symbol interference
(ISI). In order to overcome such difficulties, various ideas have been proposed in the past: predistortion in transmitters [3], equalization in receivers [4], and multi-level signaling [5]. These baseband-only (BB) techniques increase available channel bandwidth by utilizing inverse channel effects and spectral compression effects of BB signaling. However, with a given fixed baseband that is not scalable in bandwidth, they eventually meet the practical upper limit regarding expansion of the bandwidth density [6].

As a next step, the concept of simultaneous baseband and multi RF-bands for next generation interconnect was introduced to solve the fundamental limit of BB-only signaling [7]–[11]. Recently, a dual-band (BB+RF) interface (DBI) has been implemented in mobile memory interfaces [12]–[14] to enable point-to-point simultaneous bidirectional (SBD) communications.

The trend of memory interface turns to a point-to-point channel instead of multi-drop bus communication due to the poor signal integrity caused by discontinuities on channel [15]. In addition, to maximize bandwidth efficiency, the SBD communication which realizes concurrent read/write operations [5], [15] becomes increasingly popular. This is because the demand for higher power efficiency and bandwidth increases as consumer-oriented digital products continue to enhance graphic computing and media processing capabilities; accordingly, the aggregate bandwidth is projected to reach 12.8 GB/s in the near future [16]. The proposed RF-I fits into the aforementioned demands naturally. It also provides the needed SBD communication through the use of a coupling network between the BB and RF-band. Compared to conventional BB-only signaling, the proposed DBI, as shown in Fig. 1, utilizes both BB and RF-band for SBD dual-data-stream communication through a shared transmission line (T-Line). The typical BB-only signaling-based SBD memory interface usually subtracts transmitting and receiving signals at transmitters and receivers by replica circuits.

Such interconnects encounter challenges from a reduced input signal noise margin due to the increased number of voltage references [12]. Instead, the proposed DBI exploits the simple architecture of noncoherent amplitude shift keying (ASK) modulation, on-chip transformer for inductive coupling, and spectral separation between the BB and RF-band to accomplish the SBD communication. As shown with power spectral density (PSD) in Fig. 1, data (D1) is transmitted from the controller to memory by using the RF-band; data (D2) is transmitted from the memory to controller by using the BB.

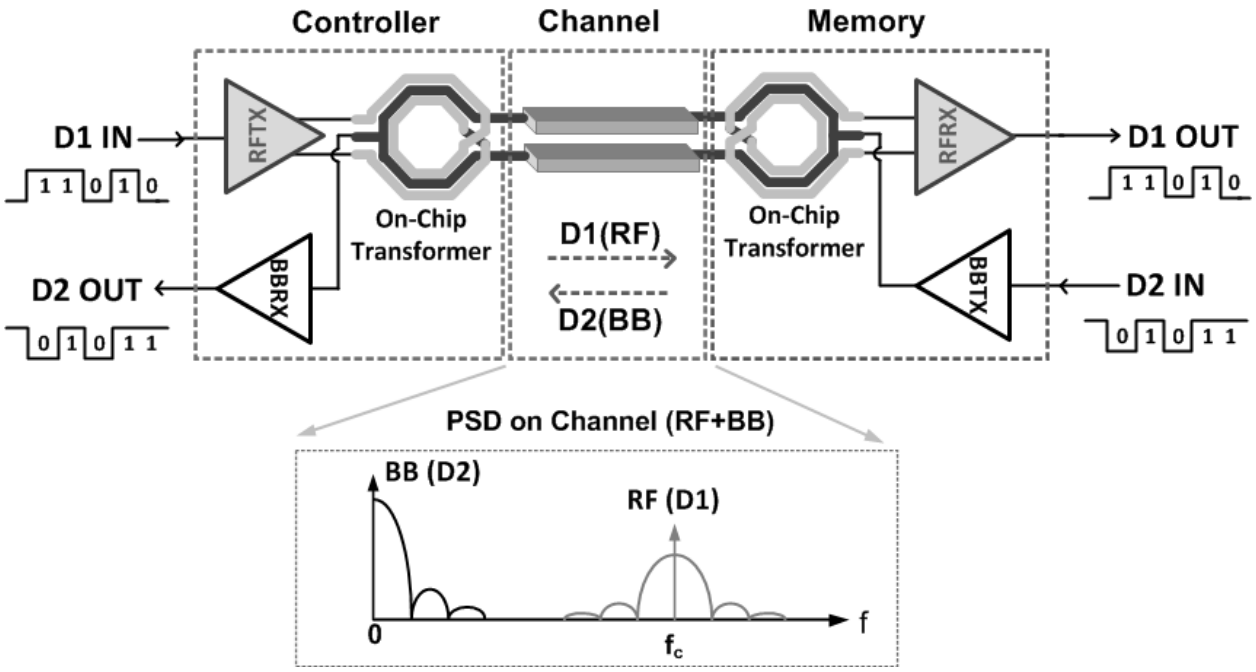

Fig. 1. DBI-based simultaneous bidirectional memory I/O interface, and dual-band power spectral density on transmission line.

Through a shared T-Lin, RF-band, and BB transmit/receive data concurrently but in opposite directions. In this paper, we first address the benefit for adapting noncoherent ASK-based dual-band interconnect by comparing different types of digital modulation. Second, we explain how we establish a system-level design for the RF-band transceiver, and study the transient behavior of RF-band data streaming with a given physical T-Line.

Finally, an inductive coupling scheme for SBD communication is introduced based on differential and common mode signaling, and the filter effects of on-chip transformers.

1.2 SNR and BER Analysis of RF-Band Transceiver

1.2.1 Theoretical BER Study

In this section, we will first review the signal-to-noise ratio requirement for the desired low BER memory interface; we will then discuss the rationale for choosing the noncoherent ASK modulation in the intended RF-I system. For the purpose of easy comparison, we limit the

range of discussion to one bit per symbol modulation. The most well-known digital modulation schemes are ASK, binary phase shift keying (BPSK), and frequency shift keying (FSK). On the receiving side, either the coherent or noncoherent communication may be implemented. Considering symbol-to-symbol distance in signal vector space, BPSK features the largest margin for error probability. In other words, the ratio of signal power to noise power is larger than the other two modulations. Therefore, BPSK can achieve the best bit error rate (BER) with the same signal-to-noise ratio (SNR). Nevertheless, a coherent BPSK communication system must provide carrier signals for demodulation in a receiver; this leads to the implementation of a high-frequency synthesizer with a large power consumption as well as large die area [17]. A coherent ASK system faces the same issue with even worse SNR conditions than BPSK [18]. In the case of FSK, it leads to either complicated synthesizer systems [19] or a large number of passive devices for multiple carrier generation. What remains is a noncoherent ASK communication system, which is the most compact solution because the demodulation is simply performed through self-mixing and subsequently detecting the envelope of the modulated signal. The objective of proposed RF-I system is to enhance the total aggregate bandwidth without adding too much power or complexity to the existing system. It is generally believed that the noncoherent ASK system is inferior to the other modulation schemes. This is however unnecessarily true for all of the different types of transceiver designs. From the digital communication theory, the BER of each modulation scheme can be expressed as

$$BER_{BPSK} = Q\left(\sqrt{\frac{2E_b}{N_0}}\right) \quad (1)$$

$$BER_{ASK,FSK} = Q\left(\sqrt{\frac{2E_b}{N_0}}\right) \quad (2)$$

$$BER_{Noncoherent,ASK} = \frac{1}{2}e^{-\frac{E_b}{2N_0}} + \frac{1}{2}Q\left(\sqrt{\frac{E_b}{N_0}}\right) \quad (3)$$

where is the average bit energy and is the noise power spectral density under additive white Gaussian noise [20]. Since each bit represents the symbol itself, the ratio of bit energy to the noise power is directly translated to the SNR. Equations (1) and (2) indicate that ASK and FSK modulations require twice as much signal power as BPSK to achieve the same BER. Fig. 2 shows that the noncoherent ASK modulation needs around 1 dB higher SNR for the same BER. For the BER of less than , BPSK, ASK/FSK, and the noncoherent ASK system must supply the SNR of 14, 17, and 18 dB, respectively.

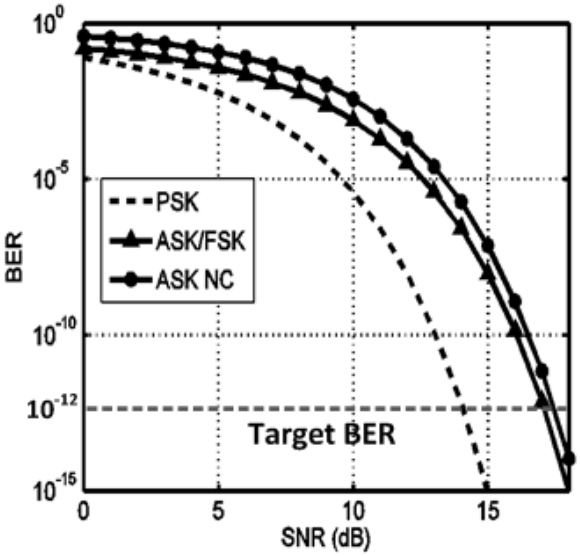

Fig. 2. Theory-based BER comparison of BPSK, ASK/FSK, and noncoherent ASK modulation.

1.2.2 SNR Estimation of Proposed RF-I Transceiver

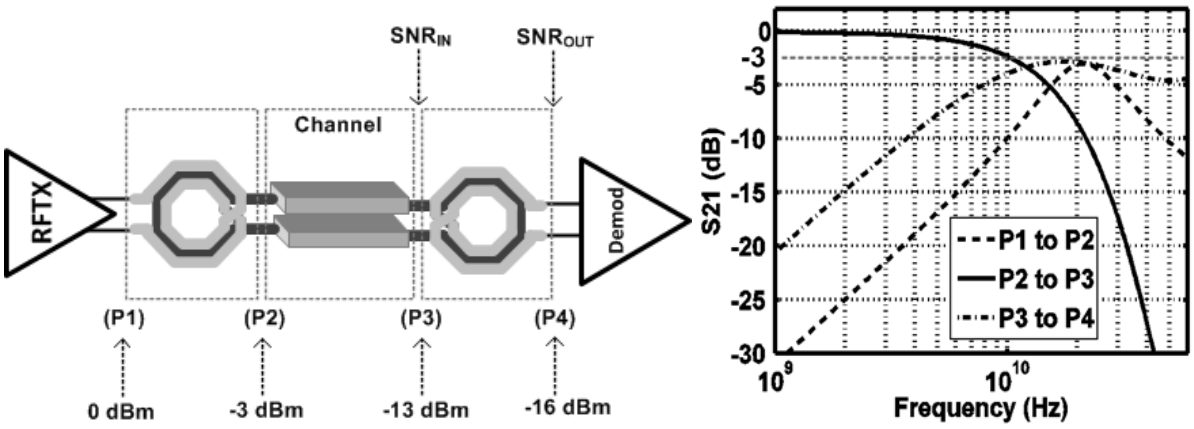

(a) (b)

Fig. 3. (a) Signal power estimation at RFTX and RFRX, and (b) simulated insertion loss (S21) through controller side transformer, off-chip channel, and memory side transformer.

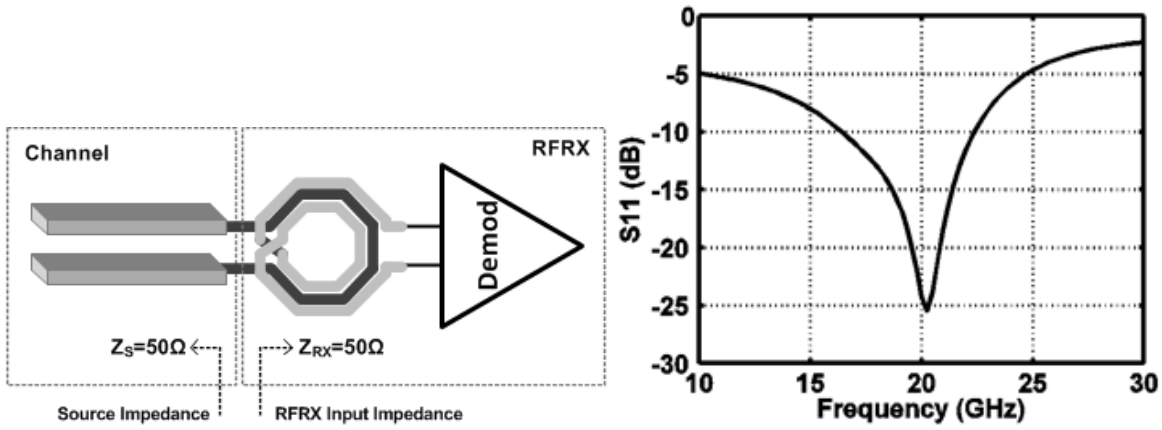

(a) (b)

Fig. 4. (a) Impedance matching using a transformer network at the input of RFRX, and (b) its return loss (S11).

The above study reveals that the noncoherent ASK RF-I receiver requires at least more than 18 dB of SNR to achieve the specified BER. Now, the SNR of proposed system can be estimated and compared to the minimum SNR calculated from the theoretical model. The first step is to approximate the signal power at each node [as shown in Fig. 3(a)]. We assume that the signal

power of RFTX at the primary coil of an on-chip transformer is 0 dBm, and this signal is inductively coupled to the off-chip channel through an on-chip transformer. A nonideal transformer will experience loss when the signal is delivered from one point another point, and this applies to both transformers in the transmitter and the receiver regardless of turn ratio. As shown with simulated insertion loss (S21) in Fig. 3(b), the power loss at a desired carrier frequency (20 GHz) through the transmitter side transformer, off-chip channel (5 cm), and receiver side transformer is around 3, 10, and 3 dB, respectively.

Therefore, the demodulator senses the signal power of 16 dBm. Since the receiver directly demodulates at the secondary coil of the transformer, the noise figure (NF) becomes approximately the power loss through the on-chip transformer on top of the noise contribution from the demodulator. The noise figure is defined as the SNR at the input of a transformer divided by the SNR at the input of a differential mutual mixer. This is because there is no further amplification or intermediate frequency down-conversion through the receiving chain. The noise contribution from the demodulator is assumed to be 10 dB, so the receiver noise figure becomes 13 dB. Again, our target is to find the minimum required signal power at the input of the receiver. Since the input SNR is defined as signal power divided by noise power , the input signal power is expressed as

$$P_{SIG,IN} = P_{NOISE,IN} \cdot BW \cdot NF \cdot SNR_{OUT} \quad (4)$$

where BW indicates RF-channel bandwidth. As shown in Fig. 4(b), the input impedance of RFRX is matched to the source impedance by using the transformer network [12]–[14], so the available thermal noise power at the receiver input port is K (Boltzmann constant) times (temperature), which is 174 dBm [21]. Finally, from thematching point of view in Fig. 4, the receiver absorbs most of the incoming energy in the span of 5 10 GHz, which corresponds to the

available bandwidth for the receiver. Putting all the pieces together thus far, the minimum signal power at the input of the receiver is calculated as

$$P_{SIG,IN}(dBm) = -174(dBm) + 10\log BW\ (dB) + NF(dB) + SNR_{OUT}(dB) \quad (5)$$

$$P_{SIG,IN} = -174(dBm) + 97(dB) + 13(dB) + 18(dB)$$

$$P_{SIG,IN} = -46(dBm) \quad (6)$$

Since the signal power is already estimated as -16dBm at the receiver input, the system has at least 30dB of noise margin for the specified BER. This study explains that the proposed RF-I is not limited by thermal noise, but possibly by other factors such as switching noise (inter-channel interference) from BB and supply noise.

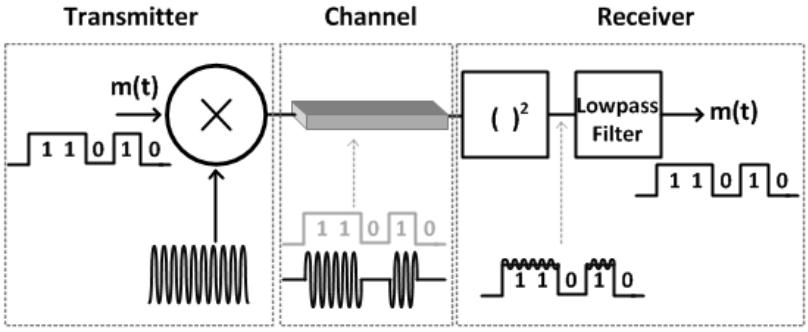

(a)

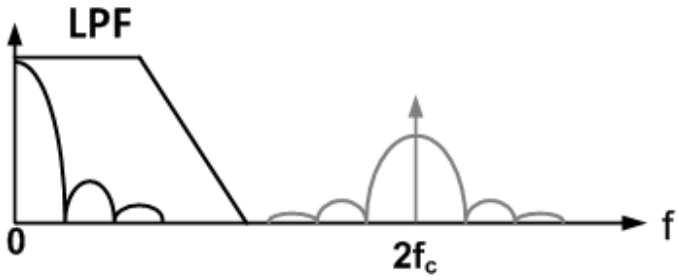

(b)

Fig. 5. (a) Block diagram of noncoherent ASK transceiver, and (b) demodulation described by power spectral density.

1.3 NON-COHERENT ASK SYSTEM DESIGN

1.3.1 Non-Coherent ASK Transceiver System Design

Based on the analysis so far, a non-coherent ASK system is designed with the block diagram shown in Fig. 5(a). One advantage of ASK communication is that an incoming random data signal does not require a bit-to-symbol conversion. Therefore, on the transmitter side, a random data stream and a carrier signal are directly multiplied and up-converted to RF-band.

$$x_{ASK}(t) = m(t)\cos(\omega_c t) \quad (7)$$

The incoming BB signal is a random sequence, so m(t) is expressed as,

$$m(t) = \sum_{n=0}^{\infty} a_n rect(t - nT_B) \quad (8)$$

where a_n is a random value of 1 or 0 with equal probabilities, and rect(t) is a box car function (single pulse) with a bit period of T_B. The modulated signal $x_{ASK}(t)$ travels through a channel and arrives at the receiver with attenuation factor A_C and a phase shift. The constant phase shift only appears in a carrier frequency, and we show that the high-frequency carrier signal is filtered out. The PSD of the arrived signal is derived as,

$$P_{RX}(f) = \frac{A_c^2}{16}\left(\frac{\sin^2(\pi(f-f_c)T_B)}{\pi^2(f-f_c)^2T_B} + \frac{\sin^2(\pi(f+f_c)T_B)}{\pi^2(f+f_c)^2T_B} + \delta(f-f_c) + \delta(f+f_c)\right) \quad (9)$$

Instead of using another local oscillator signal for demodulation in the receiver, the arrived signal is multiplied by itself (i.e. mutual mixing), resulting in a baseband data signal and modulated signal with carrier frequency that is twice that of the original carrier signal.

$$y(t) = x_{ASK}^2(t) = A_c^2 \cdot m^2(t)cos^2(\omega_c t) \quad (10)$$

$$= \frac{A_c^2 \cdot m^2(t)}{2}\left(1 + \cos(2\pi f_c t)\right) \quad (11)$$

Therefore, the second harmonic signal is superimposed on the baseband signal shown as a ripple in Fig. 5(a), and it will be filtered out by a low-pass filter in the following stages. The low-pass filter can be implemented using a differential pair with resistor loaded amplifier, because the amplifier has a limited gain bandwidth. Therefore, the unity gain bandwidth can be designed by the ratio of the device trans-conductance and loading capacitance. The part that remains is $m^2(t)$. In an old analog amplitude modulation system (AM), the squared signal $m^2(t)$ has to be further processed with a square-root operation; but for digital ASK modulation, the squared signal recovers, and reverts back to its original signal without the square-root process. Assuming logic level 0 corresponds to 0 (V) and 1 (V) represents level 1, multiplying m(t) itself will not change the logic level as long as the amplitude is higher than a threshold voltage. The data stream is a random signal, so the demodulated signal can be evaluated with its power spectral density. From (11), m(t) is the only random signal, and the following PSD is derived.

$$P_s(f) = \frac{A_c^4}{16}\left(\frac{\sin^2(\pi f T_B)}{\pi^2 f^2 T_B} + \delta(f)\right) + \frac{A_c^4}{64}\left(\frac{\sin^2(\pi(f-2f_c)T_B)}{\pi^2(f-2f_c)^2 T_B} + \frac{\sin^2(\pi(f+2f_c)T_B)}{\pi^2(f+2f_c)^2 T_B} + \delta(f-2f_c) + \delta(f+2f_c)\right) \quad (12)$$

Comparing this PSD to the original PSD as in (9), the exact same spectral is shifted to BB with a constant scale factor of A_c^2, and it also creates another signal energy at $2f_c$ with constant factor of $A_c^2/4$. Again, this portion of power will be filtered out, and the main signal is preserved after demodulation with a constant amplitude scale.

1.3.2. Transient Response Through T-Line

For transmission line systems, wires with a well-defined return path provide a guiding structure for wave propagation. Besides frequency domain analysis studied so far, it is worthwhile to evaluate the time-domain transient response of the ASK modulated signal through an off-chip channel. Provided the T-Line is lossless, an incoming signal will only experience a

phase shift. However, as operating frequency and wire length increase, dielectric loss and conductive loss would typically dominate signal attenuation. The corresponding propagation constants (γ) are given as in [22],

$$\gamma_{dielectric}(j\omega) \approx \frac{1}{2} tan\delta \cdot \omega\sqrt{LC} + j\omega\sqrt{LC} \quad (13)$$

$$\gamma_{conductor}(j\omega) \approx \frac{1}{2}\frac{R}{Z_0} + j\omega\sqrt{LC} \quad (14)$$

where $tan\delta$, Z_0, R, L and C are denoted by the loss tangent of dielectric material, characteristic impedance, series resistance of wire, series inductance of wire and capacitance between wire and return path, respectively. The real part represents signal attenuation, while the imaginary part indicates the amount of phase shift.

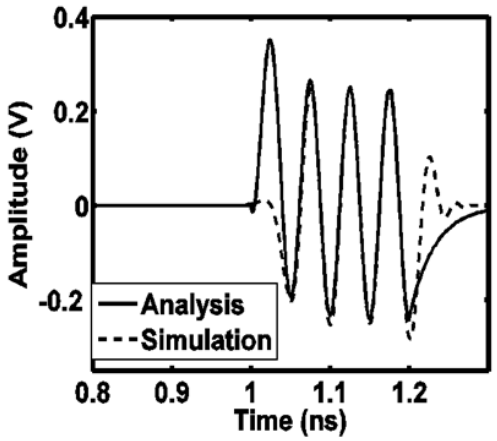

Fig. 6. Analysis-based transient channel response exhibits good agreement with the simulation-based result.

Interestingly, the dielectric loss can be modeled as a one-pole low-pass filter, since it rolls off 20dB per decade. In reality, as the length of the channel increases, the conductive part contributes more loss, including skin effect [22], thereby redering the channel response a multi-pole system. However, the proposed system specifically targets a short channel within 5cm for board-level communication such that we can approximate the channel as a one-pole system (*H*),

$$H(s) = \frac{\omega_L}{s+\omega_L} \quad (15)$$

where w_L, is a 3dB cut-off frequency. From Fig. 5(a), if a single pulse with the period of 'T_B' is mixed with a carrier signal, the input signal of the channel will be described as,

$$x(t) = [u(t) - u(t - T_B)] \cdot \sin(\omega_c t) \quad (16)$$

In order to utilize the property of convolution, (16) is converted in the Laplace domain.

$$X(s) = [1 - e^{-T_B \cdot s}] \cdot \frac{\omega_c}{s^2+\omega_c^2} \quad (17)$$

Therefore, the output of the channel becomes a multiplication of channel response and modulated input signal.

$$Y(s) = [1 - e^{-T_B \cdot s}] \cdot \frac{\omega_L}{s+\omega_L} \cdot \frac{\omega_c}{s^2+\omega_c^2} \quad (18)$$

Converting (18) back to a time domain, we can derive the following behavior,

$$y(t) = u(t) \cdot \left[\frac{\omega_c \omega_L}{\omega_c^2 + \omega_L^2} e^{-\omega_L t} - \frac{\omega_L}{\sqrt{\omega_c^2 + \omega_L^2}} \cos(w_c t + \varphi)\right]$$
$$-u(t - T_B) \cdot \left[\frac{\omega_c \omega_L}{\omega_c^2+\omega_L^2} e^{-\omega_L (t-T_B)} - \frac{\omega_L}{\sqrt{\omega_c^2+\omega_L^2}} \cos(\omega_c (t - T_B) + \varphi)\right] \quad (19)$$

where Φ accounts for the phase shift given in (13).

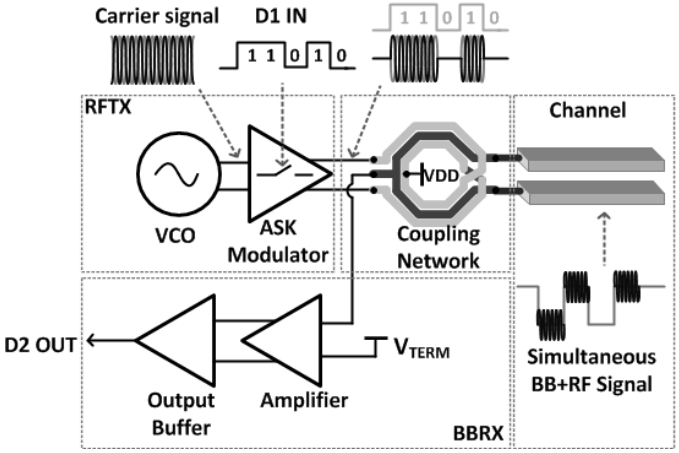

Fig. 7. Transceiver diagram for concurrent data transmission (D1) and reception (D2) in memory controller side.

The exponential behavior in (19) is not surprising because the initial condition-associated natural response will appear when a stimulus is applied, and it will eventually die out. Since an input pulse is decomposed into two modulated step functions, the output will resemble these two forcing functions. In a decomposed view by linear super-position, each source consists of a step function and carrier signal; thus, each will respond to the channel in the manner of a sinusoidal steady state. In addition, as expected, a higher frequency signal undergoes more attenuation. Setting 5GHz of cut-off frequency, 20GHz of carrier frequency, and 5Gb/s of data rate, the analysis-based result is in agreement with the schematic-based simulation described in Fig. 6.

1.4 INDUCTIVE COUPLING FOR SIMULTANEOUS BIDIRECTIONAL COMMUNICATION

1.4.1. Inductive Coupling on the Memory Controller Side

A transformer is commonly used as an isolation, impedance matching, and power transfer device. The proposed RF-I transceiver takes advantage of these properties to realize concurrent communication between BB and RF-band data transmission. First, an inductive coupling scheme on the memory controller side is illustrated with the block diagram shown in Fig. 7. The memory controller side consists of RFTX and BBRX. The RFTX sends out an ASK modulated differential signal (D1) to the primary coil (light grey) of the transformer, and the signal is inductively coupled to the T-Line via a secondary coil (dark grey), while the center tap provides a supply voltage to the ASK modulator. On the BBRX, a BB signal coming from the memory side is directly extracted at the center tap of the secondary coil with a common mode signaling. The following question may arise: Can an ASK modulated signal be coupled to the BBRX such

that D2 is no longer distinguishable? The answer can be found in differential and common mode signaling. As mentioned above, the RF-band communication utilizes a differential signaling, whereas BB communication follows a conventional common mode signaling [5], [15].

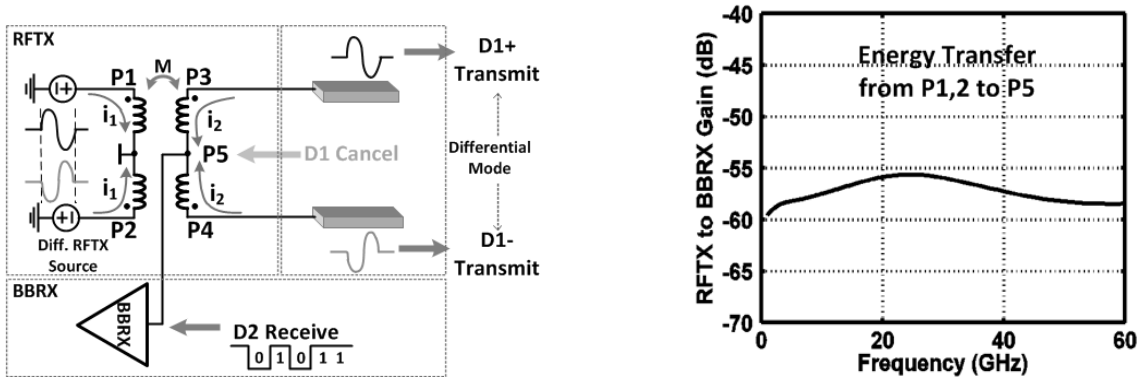

Fig. 8. (a) Equivalent coupling network on the memory controller side, and (b) frequency response from P1,2 to P5.

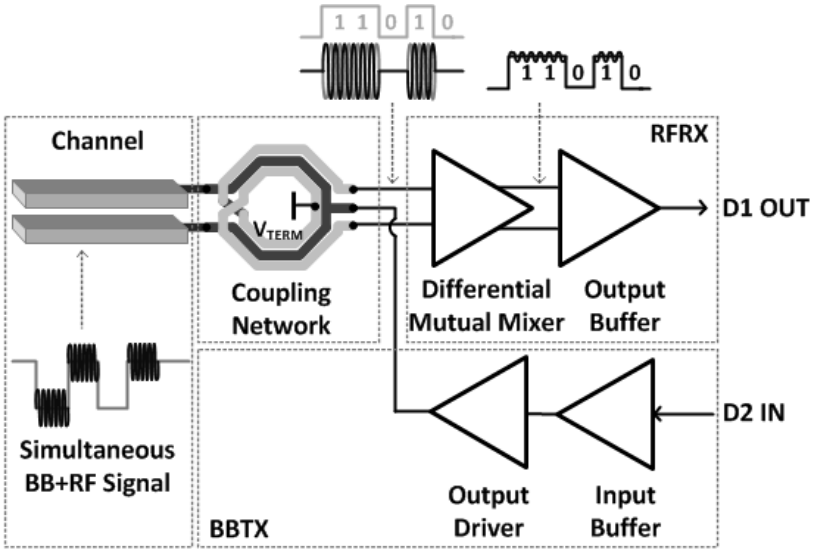

Fig. 9. Transceiver diagram for concurrent data transmission (D2) and reception (D1) on the memory side.

The differential on-chip transformer can isolate between common mode and differential mode signals, because the differential signal is seen as virtually ground at the center of each coil. This

is more clearly visualized with an equivalent coupling network shown in Fig. 8(a). The ASK modulated differential signal is injected into P1 and P2 with the center tap connected to a supply voltage, and it is inductively coupled to P3 and P4 by way of mutual inductance M. Observing P5, this node senses the same magnitude, but with an opposite polarity voltage, so that it has the effect of virtual ground in the view of RFTX differential signaling. Since there is no disturbance from RFTX, the BBRX can accept an incoming baseband signal from the T-Line. In order to quantify the actual signal flow from RFTX to BBRX, the frequency response from P1,2 to P5 is depicted in Fig. 8(b). As shown, the isolation from RF-band to BB is more than 55dB within the operating frequency. Therefore, we can achieve SBD communication on the memory controller side.

1.4.2 Inductive Coupling on the Memory Side

A similar analysis applies to the memory side. As shown in Fig 9, the RF-band signal travels through the T-Line, and it is fed into the primary coil (dark grey) of an on-chip differential transformer. The signal is now inductively coupled to the secondary coil (light grey) and injected into a differential mutual-mixer detecting envelope of incoming RF signals. Notice that there is no amplification in-between the coupling network and demodulator (as stated earlier). The differential mutual-mixer demodulates by squaring its own signal, and its output signal is amplified and filtered through following buffer chains [12]–[14]. The center tap of the secondary coil is connected to V_{TERM} to provide a bias voltage for the differential mutual-mixer. On the BBTX side, a single-ended output signal flows into the center tap of the primary coil and launches on the off-chip T-Lines.

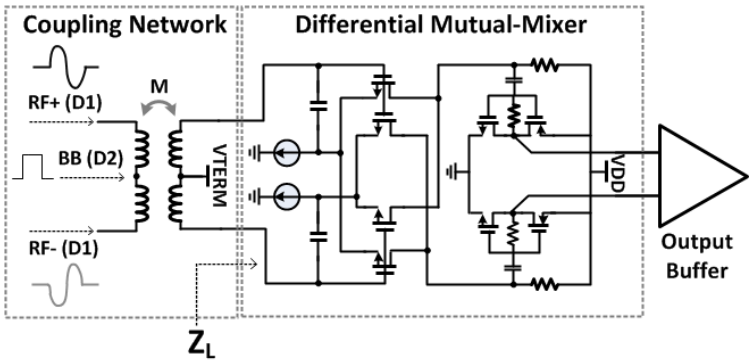

(a)

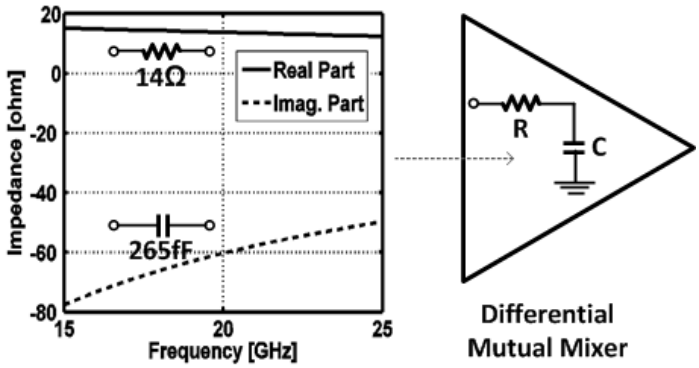

(b)

Fig. 10. (a) Schematic of differential mutual-mixer, and (b) its input impedance estimation.

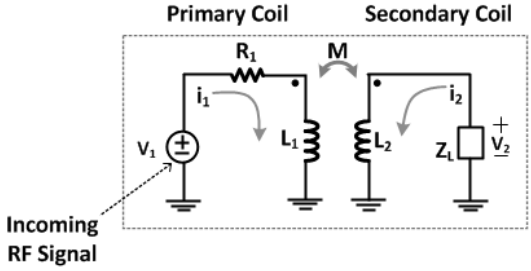

(a)

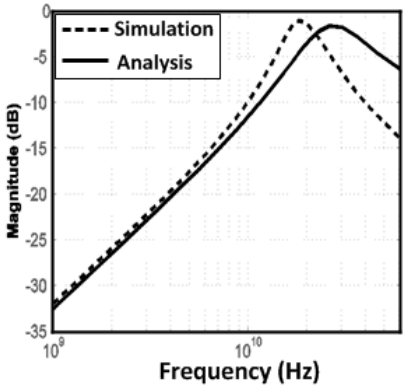

(b)

Fig. 11. (a) Simplified network for incoming RF signal, and (b) comparison of simulated and analyzed voltage gain frequency response.

Therefore, all three ports of the primary coils are occupied by incoming signals of RF (D1) and BB (D2) as shown in Fig. 10(a). In other words, both of the RF and BB signals will appear on

the secondary coil. Consequently, contrary to the inductive coupling of the controller side, the BB signal causes inter-channel interference (ICI). The amount of ICI must be minimized to enable SBD communication on the memory side. The following analysis discusses the coupling mechanism at the input of the differential mutual-mixer. First, the loading of the secondary coil is estimated as a series connection of resistor and capacitor [12], as shown in Fig. 10. Strictly speaking, the driving point impedance cannot be defined for non-linear systems, but we assume the differential mutual-mixer behaves linearly around the bias point of V_{TERM} for the purpose of network analysis. As shown in Fig. 10(b), the input impedance Z_{IN} consists of real and imaginary parts, and the real part remains relatively constant, while the magnitude of the imaginary part decreases as the frequency increases. The constant real part resembles a resistor, and the decreasing imaginary part acts as a capacitor. Thus, within the range of frequency interest, the resistance is around 14Ω, and the capacitance is estimated to 265fF using the value of 60Ω at 20GHz. With the loading condition prepared, an equivalent network for the incoming RF signal is established (as shown in Fig. 11(a)).

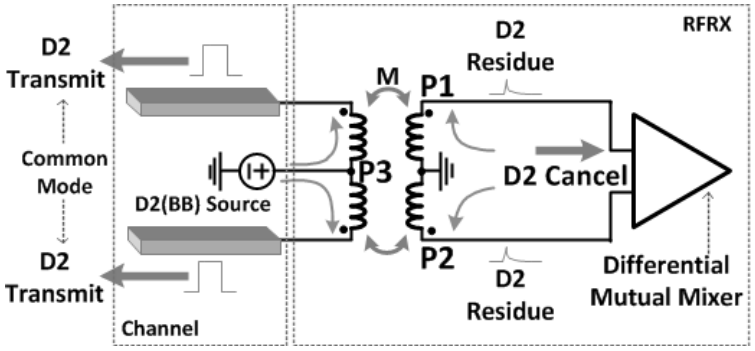

Fig. 12. Equivalent coupling network on the memory controller side.

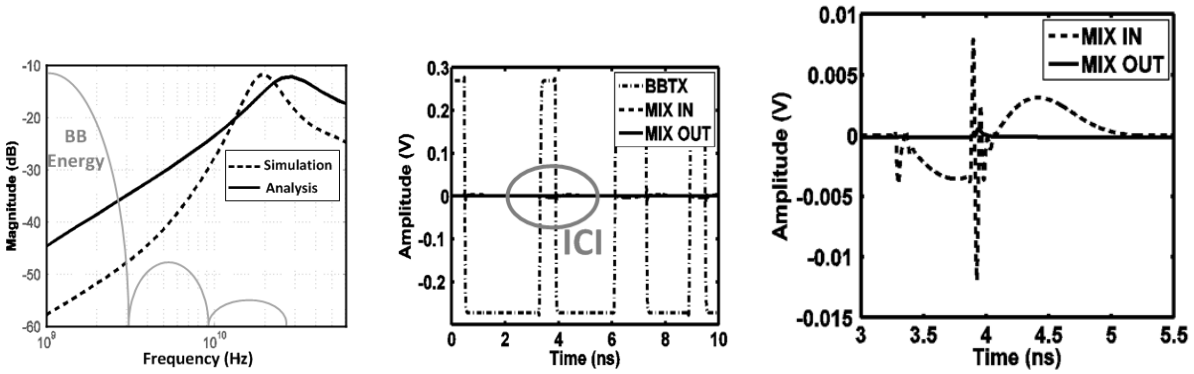

(a) (b) (c)

Fig. 13. (a) Frequency response of simulated and analyzed gain from BBTX to RFRX, (b) simulated transient waveform at the input and output of differential mutual-mixer, and (c) magnified ICI transient waveforms.

In the view of RF signals, the center tap of the primary coil becomes virtual ground for the same reason that it does on the controller side, and the center tap of secondary coil also becomes AC-short because of constant voltage V_{TERM}. Therefore, the differential circuits can be analyzed by a half circuit. Although a transformer model is much more complicated than the model in Fig. 11(a), considering all the substrate loss, capacitive coupling, and series resistance of metal line, we only focus on the main core inductance in order to achieve the rough estimation of transfer characteristics. On the primary coil side, V_1 and R_1 model the incoming source and its resistance; on the secondary coil side, the series connection of resistor and capacitor of loading is expressed as Z_L. Between the primary and secondary coils, there will be magnetic flux coupling, and this is denoted as M in its expression,

$$M = k\sqrt{L_1 L_2} \quad (20)$$

where k is the coupling coefficient. To find signal transfer characteristics from the primary coil to secondary coil, the following relationships can be derived.

$$\begin{pmatrix} v_1 \\ 0 \end{pmatrix} = \begin{pmatrix} R_1 + sL_1 & sM \\ sM & sZ_L + sL_2 \end{pmatrix} \begin{pmatrix} i_1 \\ i_2 \end{pmatrix} \quad (21)$$

$$v_2 = -i_2 Z_L \quad (22)$$

$$A_v = \frac{v_2}{v_1} = \frac{R_2 M s \cdot \left(s + \frac{1}{R_2 C_2}\right)}{(L_1 L_2 - M^2)s^3 + (R_2 L_1 + R_1 L_2)s^2 + \left(R_1 R_2 + \frac{L_1}{C_2}\right)s + \frac{R_1}{C_2}} \quad (23)$$

It is obvious that there is no coupled energy at DC since there is no induced magnetic flux, and as the operating frequency increases, the coupling network transfers more energy to the other side. The RF signal confines most of the energy at its carrier frequency, which is around 20GHz, so the network must provide the highest energy transfer at this frequency. From (23), two zeros are located at origin and $-1/R_2C_2$, and there exists three poles in total. As expected, the network picks up more signal as the operating frequency increases, and it will lose transfer capability as the frequency further increases. Instead of solving a full cubic algebraic solution, voltage transfer characteristics are directly illustrated in Fig. 11(b) using component values in Table I.

TABLE I
COMPONENT VALUES IN COUPLING NETWORK

$\mathbf{R_1}$	$\mathbf{R_2}$	$\mathbf{C_2}$	$\mathbf{L_1}$	$\mathbf{L_2}$	**k**
50Ω	14Ω	265pF	125pH	125pH	0.75

In this table, R_1 simply represents channel impedance, and L_1, L_2, and k are extracted using 3-dimensional full-wave electromagnetic simulations.

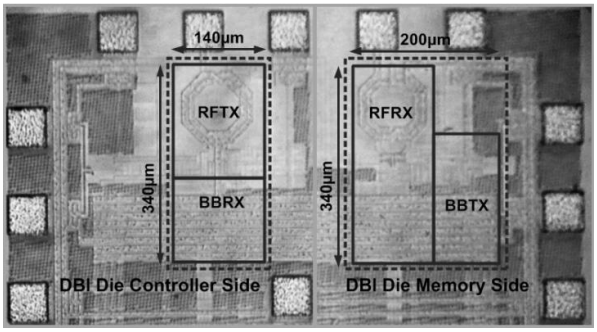

(a)

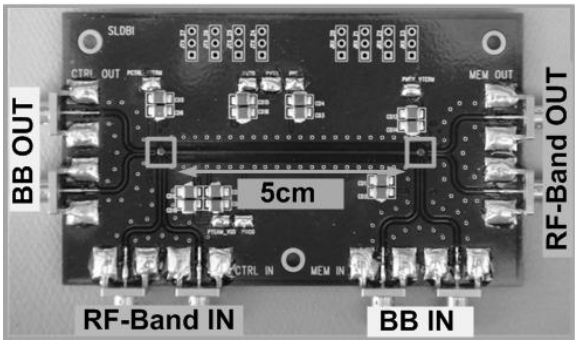

(b)

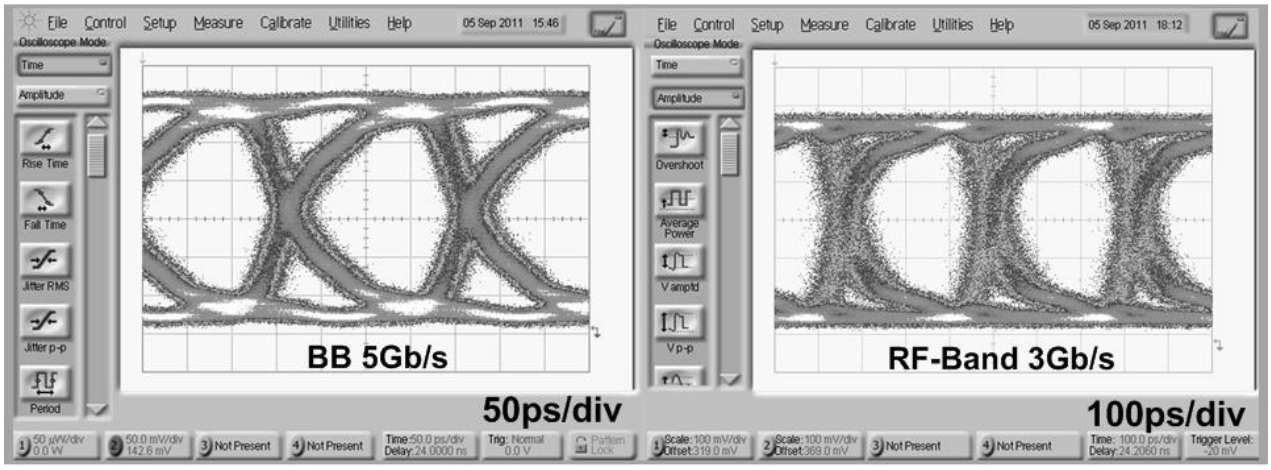

(c)

Fig. 14. (a) DBI transceiver die photo, (b) 5cm off-chip test board, and (c) BB and RF-band eye test results.

The results in Fig. 11(b) indicate that the coupling network indeed passes through the highest energy around the carrier frequency, and it decreases the amount of energy for higher frequency of operation. It is also compared to schematic-based simulation results, and the dotted line shows that there is a good agreement with the analytic result.

Turning our attention to the coupling between BBTX and RFRX, coupled BB signals at the input of the differential mutual-mixer are detrimental for RF (D1) communication. The BB signal may leak through either high-pass or band-pass filtering with its residue remaining as a

common mode signal at the differential mutual-mixer (as shown in Fig. 12). Just like the RFTX signal at the primary coil, an equivalent circuit can be simplified to its half circuit. Since the BB signal is fed into the center tap of primary coil, its signal power will be equally distributed to each leg of coil. Again, the center tap of secondary coil is terminated with V_{TERM} such that this is treated as AC-short for the analysis. Interestingly, the simplified network looks exactly the same as in Fig. 11(a), except R1 becomes 100Ω considering its own source resistance and channel impedance in the primary coil side. Therefore, (21)–(23) are still valid for the BBTX signal at the input of the differential mutual-mixer. Similar to the previous case, instead of delving into equation solving or parametric study, we observe the behavior of how the energy is transferred from center tap of the primary coil to the secondary coil. As shown in Fig. 13(a), the hand-analysis achieves a close approximation to the schematic-based simulation. In the same figure, a solid grey line is added to represent the spectral separation between BB and RF communication. Just as shown, as the data rate of BB increases, its impact on the RFRX becomes higher, and it eventually limits the total aggregate bandwidth on the memory side. This is more clearly visualized with the simulated time domain transient waveforms in Fig. 13(b) and (c). The BBTX output buffer feeds square-wave random data, and filtered signals appear at the input of the differential mutual-mixer. It seems as if the amplitude is so small that the effect of ICI is negligible, but in a zoomed-in view, the peak-to-peak amplitude of residue reaches almost 20mV. The mixer responds to this perturbation, and it creates a glitch at the output, as shown in Fig. 13(c). There are a few ways to reduce the ICI. First, assuming the BBRX is capable of sensing low-swing incoming signals after channel attenuation, the BBTX output signal can be intentionally lowered to reduce the amount of coupled signals at the secondary coil. Second, a simple pulse shaping can be applied to BBTX to minimize glitches. Third, even if RFTX outputs

enough power, the sensitivity of RFRX can be reduced intentionally. Therefore, using the simple coupling network studied above, we can achieve simultaneous bidirectional communication on the memory side.

1.5. DUAL-BAND EXPERIMENTS

A dual-band RF-I transceiver is implemented using 65nm general-purpose CMOS process as shown in Fig. 14(a). The active die area is $0.12mm^2$. A printed circuit board (PCB) is also designed to demonstrate the SBD communication through a 5cm single-ended off-chip trace as shown in Fig. 14(b). The fabricated chips are assembled using a flip-chip bonding technology to reduce the inductance of chip-to-board wire-bonds. Fig. 14(c) exhibits a concurrent data communication through a shared off-chip T-Line; 5Gb/s of BB and 3Gb/s of RF-band. When each of BB or RF-band is transmitted alone, it operates up to 6Gb/s and 4Gb/s, respectively. However, the ICI limits the performance of RF-band operation if the data rate of BB exceeds 5Gb/s.

In summary, we have analyzed, designed and characterized the DBI transceivers for mobile DRAM I/O interface. We obtained an aggregate data throughput of 4.2Gb/s/pin with power consumption of 23mW (BB:12mW, RF-band: 11mW) on differential T-Lines; and we also achieved 8Gb/s/pin with power consumption of 32mW (BB:14.4mW, RF-band:17.6mW) on a single T-Line. The BER is measured as $<10^{-23}$ with 2^{23}-1 and $<1\times10^{-12}$ with 2^{15}-1 pseudo random bit pattern for differential T-Lines and single T-Line respectively. The power consumption is measured higher for the single T-Line RF-I link, because higher power supply was used to support the high-frequency operation of a ring oscillator [14]. However the energy-per-bit-per-pin is still measured lower because of the single-ended solution.

1.6 CONCLUSION

A non-coherent ASK modulation-based RF-I system is presented for memory interface design. The proposed system is not limited by thermal noise, which leads to a compact and energy-efficient transceiver architecture design. Our analysis on the DBI communication network and channel proves that the RF-I can help to enhance an aggregate data rate without substantial overhead to the entire system. In order to realize simultaneous bidirectional communication, both on the controller and memory sides, an inductive coupling using on-chip transformers is introduced. On the controller side, the nature of signaling and differential transformer geometry isolates BB and RF-band communications nearly perfectly; whereas on the memory side, the BB signal couples through the transformer network and creates inter-channel interference. However, the amount of coupled signal can be minimized with the transformer's filter effect.

Chapter 2

Impulse Response Analysis of Carrier-Modulated Multiband RF-Interconnect (MRFI)

2.1 Introduction

Over the years, systems such as asymmetric digital subscriber lines (ADSL) and very high-speed digital subscriber lines (VHDSL) have proven the vital role of passband signaling in the area of wireline data communication. Accordingly, academia/industry has conducted numerous research to study the performance of information carrying passband signals through wires/cables [25-32]. As part of the continuing evolution aimed at multi-gigabit per second (Gb/s) wireline communication, a similar passband signaling, also known as Multiband RF-interconnect (MRFI), has been proposed to transfer multiple baseband data simultaneously by way of carrier-modulated RF channels [33-39]. As a common approach, previous works have adopted an on-off keying (OOK) modulation with self-mixing down-conversion architecture for RF channels and demonstrated data rate of multi-Gb/s through shared on-chip or off-chip transmission lines. An OOK with self-mixing non-coherent architecture benefits energy efficiency because a receiver does not require additional synthesizer or carrier synchronization. Unfortunately, the non-coherent system lacks the ability to split signal space into in-phase (I) and quadrature-phase (Q) domains for RF channels. In order to maximize spectral efficiency, recent research has developed multi-level, multi-band, and IQ processing coherent transceiver architecture, which is the main interest of this paper [38-43]. A generalized block diagram of coherent MRFI system is illustrated in Fig. 15. Note that the number of RF channels and selection of carrier frequency are flexible, and multi-level signaling can be applied to each data path by adding digital-to-analog converter (DAC) in transmitter (TX) and analog-to-digital converter (ADC) in receiver (RX).

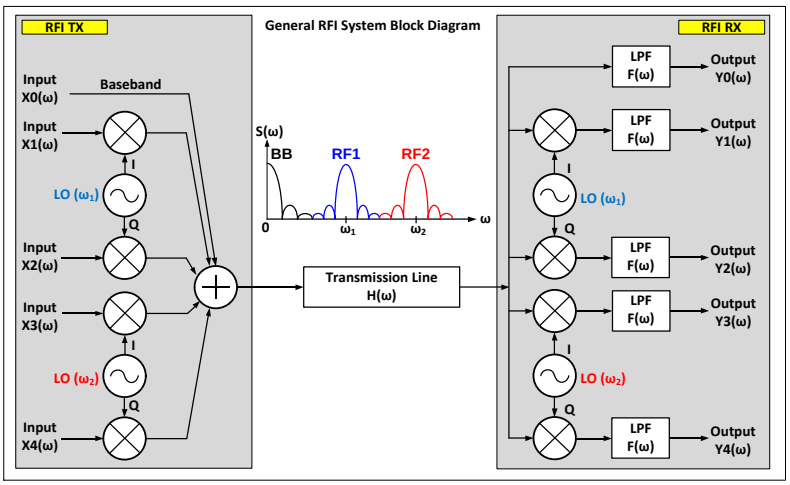

Fig. 15. Generalized block diagram of coherent MRFI system.

Although previous research has suggested the potential of deploying MRFI system in wireline data communication platform, no theoretical background has been provided to evaluate the information capacity of given transmission line. Transmission lines are known to be dispersive or band-limited mainly because conductive loss and dielectric loss increase as frequency of operation increases. Typically, the frequency where loss is 3dB~6dB offers a rough estimate of how much data transmission line can convey. This 3~6dB estimation can change depending on system requirements, but this paper assumes -3dB frequency as the bandwidth of transmission line. More advanced methods include sending a short pulse and measuring pre/post cursor, or one step further, evaluating an eye-diagram by transmitting random bit sequences. The underlying assumption to the methods above is that either a scattering parameter or linear time-invariant (LTI) impulse response of transmission line is readily available.

One of the major goals of this paper is to come up with an exact expression of baseband-equivalent impulse response in frequency domain when coherent MRFI transceivers communicate through transmission lines that support transverse electromagnetic (TEM) mode of propagation.

A baseband-equivalent impulse response fully captures the physical characteristics of carrier frequency dependent passband signals through physical channels and translates as if the system functions in baseband domain. Because of its baseband equivalency, direct frequency response comparison between various carrier frequencies, or comparison between baseband-only signaling versus MRFI signaling, is possible for a given transmission line. The proposed impulse response analysis will not consider performance of electronics but focus only on physical properties of transmission lines including loss, non-idealities, signal-to-noise (SNR) trade-off, and eye-diagram characteristics.

2.2 Baseband-Equivalent Impulse Response

One of the RF channels from Fig. 15 is emphasized with annotations in Fig. 16(a). The system diagram in Fig. 16(a) contains only an in-phase path, but a quadrature path could always be added for the same analysis. Also, time domain and frequency domain symbols are written with lower case and upper case letters, respectively.

An input data $x(t)$ modulates carrier (ω_0) via up-converter and travels through a transmission line $h(t)$. A down-converter then de-modulates an incoming signal with receiver side local oscillator (LO). A fixed amount of extra LO phase, which is directly calculated from transmission line delay at the carrier frequency, is added to receiver LO to synchronize phase between transmitter and receiver. A method of synchronization is beyond the discussion of this paper, and the phase and frequency between transmitter and receiver are assumed to be synchronized. In the last stage, a low-pass filter (LPF) filters out the residue of $2\omega_0$ component generated from the down-conversion process. An ultimate objective is to capture the non-linear property of transmission line frequency response and translate to baseband-equivalent impulse response $i(t)$ or $I(\omega)$ model in Fig. 16(b). With an impulse response defined, an output

becomes,

$$Y(\omega) = X(\omega)I(\omega) \quad (1)$$

$$y(t) = x(t) * i(t) \quad (2)$$

where $*$ operator indicates a convolution.

Based on the system block diagram, the process of frequency domain computation is built in Fig. 16(c). After solving Maxwell's equations with boundary conditions of a given transmission line, a governing frequency response of electromagnetic field propagating in z-direction can be readily evaluated as,

$$H_+(\omega) = \begin{cases} e^{-\alpha(\omega)z}e^{-j\beta(\omega)z} & (\omega > 0) \\ 0 & (\omega < 0) \end{cases}$$
$$H_-(\omega) = \begin{cases} 0 & (\omega > 0) \\ e^{-\alpha(\omega)z}e^{+j\beta(\omega)z} & (\omega < 0) \end{cases}$$
$$H(\omega) = H_+(\omega) + H_-(\omega) \quad (3)$$

where α is an attenuation constant, β is a propagation constant, and z is length of transmission line [22]. $H(\omega)$ divides into (+) and (-) components to process a conjugate symmetric property of frequency response. Attenuation constant α and propagation constant β are frequency-dependent, geometry-dependent, and transmission-line-type-dependent. A key message in this figure is to include and calculate the negative frequency spectral portion throughout the procedure. To summarize the process at each node, following frequency domain expressions are written.

$$\text{A: } X(\omega) \quad (4)$$

$$\text{TX LO: } \frac{1}{2}[\delta(\omega + \omega_0) + \delta(\omega - \omega_0)] \quad (5)$$

$$\text{B: } \frac{1}{2}[X(\omega + \omega_0) + X(\omega - \omega_0)] \quad (6)$$

$$\text{C: } \frac{1}{2}[X(\omega+\omega_0)H_-(\omega)+X(\omega-\omega_0)H_+(\omega)] \qquad (7)$$

$$\text{RX LO: } \frac{1}{2}\left[\delta(\omega+\omega_0)e^{+j\beta(\omega)z}+\delta(\omega-\omega_0)e^{-j\beta(\omega)z}\right]$$

$$=\frac{1}{2}\left[\delta(\omega+\omega_0)e^{+j\beta(-\omega_0)z}+\delta(\omega-\omega_0)e^{-j\beta(\omega_0)z}\right] \qquad (8)$$

$$\text{D: } \left\{\frac{1}{2}[X(\omega+\omega_0)H_-(\omega)+X(\omega-\omega_0)H_+(\omega)]\right\}$$

$$*\left\{\frac{1}{2}\left[\delta(\omega+\omega_0)e^{+j\beta(-\omega_0)z}+\delta(\omega-\omega_0)e^{-j\beta(\omega_0)z}\right]\right\} \quad (9)$$

In (8), only a fixed phase portion is extracted from $H(\omega)$ without the amplitude contribution and accumulated to a receiver LO for phase synchronization. Next, (9) can be further expanded to,

$$\begin{aligned}&\frac{1}{4}X(\omega)\left[H_-(\omega-\omega_0)e^{-j\beta(\omega_0)z}+H_+(\omega+\omega_0)e^{+j\beta(-\omega_0)z}\right]\\&+\frac{1}{4}X(\omega+2\omega_0)H_-(\omega+\omega_0)e^{+j\beta(-\omega_0)z}\\&+\frac{1}{4}X(\omega-2\omega_0)H_+(\omega-\omega_0)e^{-j\beta(\omega_0)z} \qquad (10)\end{aligned}$$

The first term in (10) reveals that a baseband spectrum is multiplied by the sum of two frequency shifted transmission line frequency responses. For the latter two terms, it is clear that they are $2\omega_0$ components, and they make the system in (10) linear time-variant (LTV). Thus, from a mathematical standpoint, an LPF must fully reject the $2\omega_0$ residue in order for a baseband-equivalent frequency response to remain as an LTI system. Practically speaking, the above statement is a reasonable assumption (a consequence of ignoring residue will be explained in the following section), because an LPF needs to be sharp enough to reject inter-channel interference (ICI) between multiple RF channels. Therefore, an output spectrum can be written as,

E:

$$Y(\omega)=\frac{1}{4}X(\omega)F(\omega)\left[H_-(\omega-\omega_0)e^{-j\beta(\omega_0)z}+H_+(\omega+\omega_0)e^{+j\beta(-\omega_0)z}\right]$$

(11)

As indicated above, a choice of LPF could greatly affect a baseband-equivalent impulse response. Since the expression of output spectrum is ready, following the definition of impulse response, $x(t) = \delta(t)$, which is $X(\omega) = 1$, can be inserted into (11), and finally a baseband-equivalent impulse response in frequency domain is derived as,

$$I(\omega) = Y(\omega)|_{X(\omega)=1} = \frac{1}{4}F(\omega)\left[H_{-}(\omega - \omega_0)e^{-j\beta(\omega_0)z} + H_{+}(\omega + \omega_0)e^{+j\beta(-\omega_0)z}\right] \tag{12}$$

There are two important things to highlight. First, a baseband-equivalent impulse response in frequency domain consists of positively shifted and negatively shifted $H(\omega)$ around a carrier frequency. Second, a baseband-equivalent impulse response depends heavily on a carrier frequency.

2.3. MICROSTRIP LINE

Microstrip lines are an essential part of a high-speed data communication system because of its capability of easy fabrication and integration with other components. Throughout the study, specific dimension, transmission line length, and frequency range will be used because of relation to pulse behavior in time domain. Detailed parameters and geometry of microstrip line are summarized in Fig. 17(a). A common FR4 will be used as substrate material. Note that the same analysis can be applied to any other types of transmission lines such as stripline, co-planar waveguide, twisted pairs, and coax cables, as long as α and β can be provided by analytical calculation, software-aided simulation, or measurement.

2.3.1 Attenuation and propagation constant

Instead of repeating the procedure of solving boundary conditions for Maxwell's

equations, readily available attenuation and propagation constants of microstrip line are brought from [49],

$$\text{Free Space Wavenumber: } k_0 = \omega\sqrt{\mu_0\epsilon_0} \qquad (13)$$

$$\text{Propagation Constant: } \beta = \omega\sqrt{\mu_0\epsilon_0\epsilon_r} \qquad (14)$$

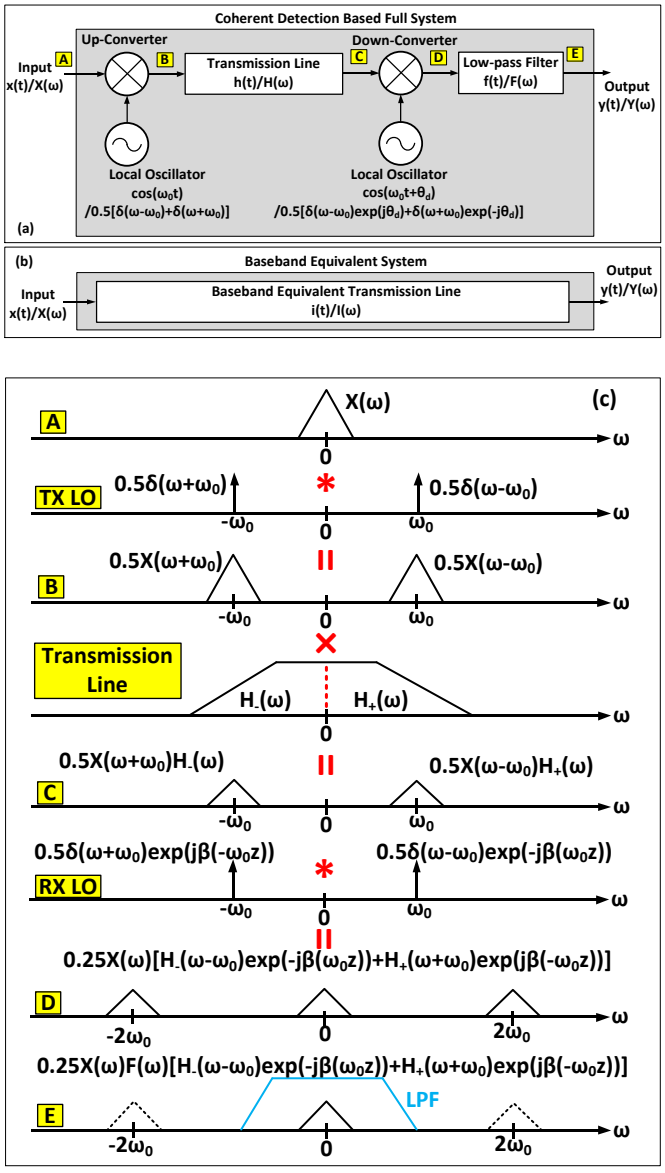

Fig. 16. (a) Coherent based full transmitter and receiver system includes up-converter, down-converter, local oscillators, and low-pass filter. Two local oscillators are assumed to be phase

and frequency synchronized in the transmitter and receiver side. (b) The full system is replaced by a baseband-equivalent transmission line channel as an impulse response. (c) The process of frequency domain calculation is shown in alphabetical order that was listed in Fig. 16(a). Note from the property of LTI system that time domain multiplication becomes frequency domain convolution, and time domain convolution becomes frequency domain multiplication.

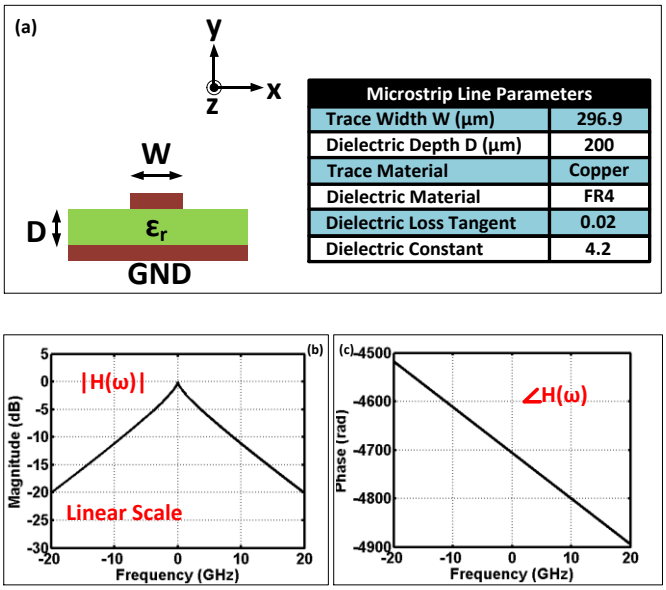

Fig. 17. (a) Cross-section of microstrip line is shown with its parameters. Wave propagates along z-direction. (b) Magnitude response of 10-inch microstrip line in linear scale. (c) Phase response of microstrip line.

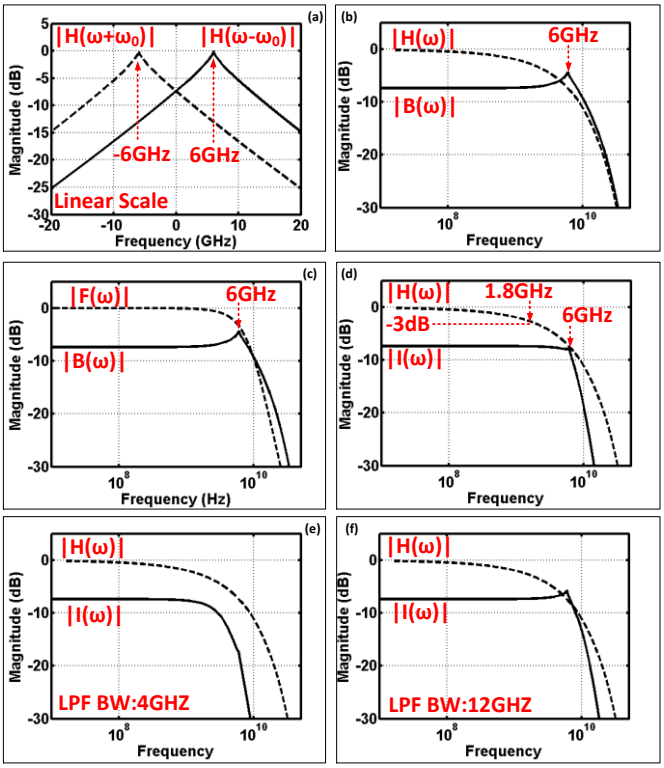

Fig. 18. (a) Positively and negatively shifted magnitude response. (b) Frequency response $H(\omega)$ of 10-inch microstrip line and its baseband-equivalent impulse response $B(\omega)$, one without LPF, in log scale when carrier frequency is 6GHz. (c) Bessel 3rd order LPF frequency response and magnitude response of $B(\omega)$. (d) Final magnitude response of $I(\omega)$ is plotted with LPF bandwidth of 8GHz and compared to magnitude response of $H(\omega)$. (e) Impulse response when LPF bandwidth is 4GHz. (f) Impulse response when LPF bandwidth is 12GHz.

$$\text{Surface Resistivity: } R_S = \sqrt{\frac{\omega\mu_0}{2\sigma}} \qquad (15)$$

$$\text{Effective Dielectric Constant: } \epsilon_e = \frac{\epsilon_r+1}{2} + \frac{\epsilon_r-1}{2}\sqrt{\frac{1}{1+\frac{12D}{W}}} \qquad (16)$$

$$\text{Conductive Atten. Constant: } \sigma_c = \frac{R_S}{Z_0 W} \qquad (17)$$

$$\text{Dielectric Atten. Constant: } \sigma_d = \frac{k_0\epsilon_r(\epsilon_e-1)tan\delta}{2\sqrt{\epsilon_e}(\epsilon_r-1)} \qquad (18)$$

where μ_0 is permeability in air, μ_r is permeability in medium, ϵ_0 is permittivity in air, ϵ_r is permittivity in medium, σ is conductivity of trace material, D is depth of microstrip line, W is

width of microstrip line, and $tan\delta$ is loss tangent of medium. An attenuation constant is the sum of conductive and dielectric attenuation constant. Using the parameters in Fig. 17(a) and transmission line frequency response in (3), phase and magnitude responses of a 10-inch microstrip line are plotted in Fig. 17(b) and (c). Notice how the phase is asymmetric and magnitude is symmetric around DC. In a general complex number domain, when a system or signal is a real number, the Fourier transform of it becomes conjugate symmetric. A transmission line in time domain is also a real number system, which is why the frequency domain phase and magnitude response appears as conjugate symmetric.

2.3.2 Baseband equivalent impulse response in frequency domain

As a reminder from (12), an impulse response in frequency domain is a combination of two frequency responses of microstrip line: one positively shifted, and the other negatively shifted, around a carrier frequency. After applying the frequency response in (3) to (12), each of shifted frequency response over 10-inch length (z_1) and resulting baseband-equivalent impulse response are derived as,

$$\frac{1}{4}H_{-}(\omega-\omega_0)e^{-j\beta(\omega_0)} = \frac{1}{4}e^{-\alpha(\omega-\omega_0)z_1}e^{+j\beta(\omega-\omega_0)z_1}e^{-j\beta(\omega_0)z_1} \tag{19}$$

$$\frac{1}{4}H_{+}(\omega+\omega_0)e^{+j\beta(-\omega_0)} = \frac{1}{4}e^{-\alpha(\omega+\omega_0)z_1}e^{-j\beta(\omega+\omega_0)z_1}e^{+j\beta(-\omega_0)z_1} \tag{20}$$

$$I(\omega) = \frac{1}{4}F(\omega)\left[e^{-\alpha(\omega+\omega_0)z_1}e^{-j\beta(\omega+\omega_0)z_1}e^{+j\beta(-\omega_0)z_1} + e^{-\alpha(\omega-\omega_0)z_1}e^{+j\beta(\omega-\omega_0)z_1}e^{-j\beta(\omega_0)z_1}\right] \tag{21}$$

In order to de-embed the effect of LPF, another impulse response expression $B(\omega)$ without LPF is also written as,

$$B(\omega) = \frac{1}{4}\left[e^{-\alpha(\omega+\omega_0)z_1}e^{-j\beta(\omega+\omega_0)z_1}e^{+j\beta(-\omega_0)z_1} + e^{-\alpha(\omega-\omega_0)z_1}e^{+j\beta(\omega-\omega_0)z_1}e^{-j\beta(\omega_0)z_1}\right]$$

(22)

In the following section, the impact of carrier frequency will be studied in conjunction with the length of transmission line, but for a concept demonstration at the moment, the carrier frequency is deployed at 6GHz. As shown in Fig. 18(a), a down-conversion by a carrier frequency shifts the frequency response of transmission line around (+) and (-) 6GHz while preserving its original response. Then, from (22), the magnitude response of $B(\omega)$ is constructed in Fig. 18(b). Interestingly, a frequency peaking at 6GHz is observable as if the impulse response works as a linear equalizer. Indeed without even solving (22), the peaking behavior can be deduced from Fig. 18(a). Again, a baseband-equivalent impulse response is the sum of two frequency responses (not multiplication), which means the positively shifted frequency response dominantly rises after DC. In Fig. 18(c), frequency response of 3rd order Bessel filter is plotted to implement a linear in-band group delay LPF [39]. The cutoff frequency of LPF in this figure is 8GHz, but it needs to be adjusted depending on bandwidth of RF channel and ICI.

Using (21), the final magnitude of impulse response $I(\omega)$ is plotted in Fig. 18(d). First of all, the -3dB bandwidth of $I(\omega)$ is increased to 6.5GHz from the original channel bandwidth of 1.8GHz. Second, DC gain is reduced to -7.4dB in exchange of bandwidth, which is exactly how pre-emphasis is performed. Third, one can also expect that an LPF would eventually determine the bandwidth of impulse response $I(\omega)$ as cutoff frequency of $F(\omega)$ goes below the carrier frequency as shown in Fig. 18(e) and (f). Lastly, one should keep in mind that a baseband data bandwidth of RF channel cannot be larger than carrier frequency. For instance in Fig. 18(d), the -3dB bandwidth is higher than 6GHz, which is the carrier frequency, but it does not mean that an input data rate can be as high as 6Gb/s bandwidth. Based on the arguments above, higher carrier frequency can achieve higher bandwidth, but at the same time, it loses signal-to-noise ratio

(SNR) depending on the length of microstrip line.

As stated in (1), after having established the impulse response of transmission line, an output spectrum can be calculated instantly by multiplying input spectrum and impulse response in frequency domain, as shown in Fig. 19. For instance, imagine 250ps of single pulse, which is up-converted by carrier frequency of 6GHz, travels down to a 10-inch microstrip line, and gets down-converted by receiver LO of 6GHz. In frequency domain, it means a sync function is multiplied by the impulse response calculated in Fig. 18(d). Notice the output spectrum rolls off quickly after 6GHz influenced by the impulse response bandwidth of 6GHz. Based on the development in (21), this efficient multiplication process in frequency domain can be applied to any carrier frequency or length of microstrip line.

2.3.3 Time domain impulse response and simulation

In Fig. 20(a), the impulse response of microstrip line in time domain is first calculated by taking an inverse Fourier transform of (21) in MATLAB software. Interestingly, a finite delay of modulated wave through a microstrip line is also reflected in the baseband-equivalent impulse response while the causality condition is kept for the impulse response operable. As suggested in (2), impulse response in time domain is now convoluted with an input pulse to generate an output pulse shown in Fig. 20(c).

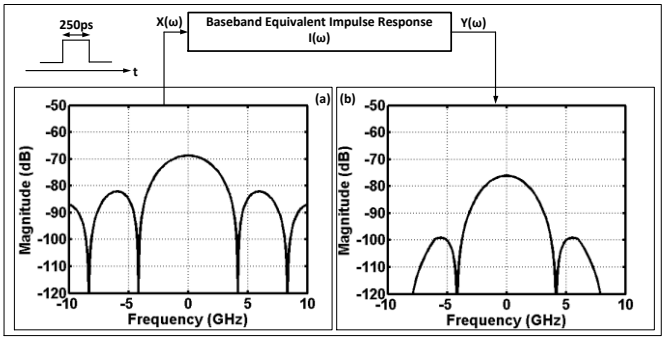

Fig. 19. (a) A 250(ps) baseband pulse is generated at the input of microstrip line. (b) After taking Fourier transform, input spectrum is fed into the baseband-equivalent impulse response of microstrip line, and the output spectrum of pulse is generated instantly by multiplying two spectrums.

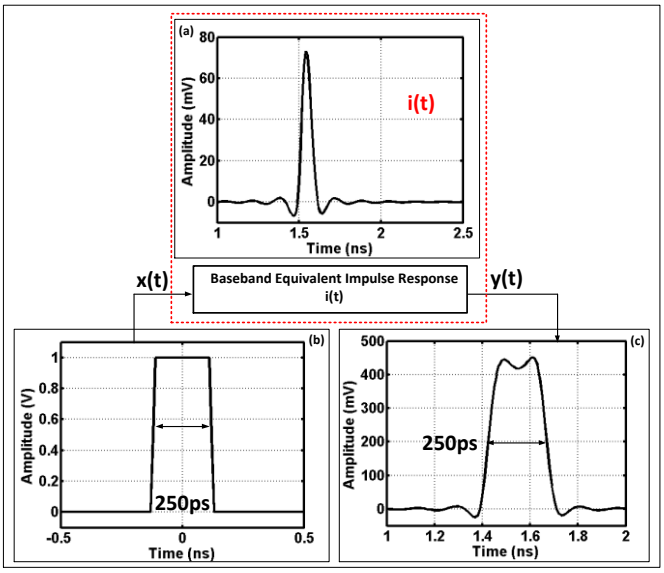

Fig. 20. (a) Time domain impulse response is calculated on MATLAB from (23). (b) A 250(ps) baseband pulse is generated. (c) Two are convoluted in time domain. A resulting output pulse generated.

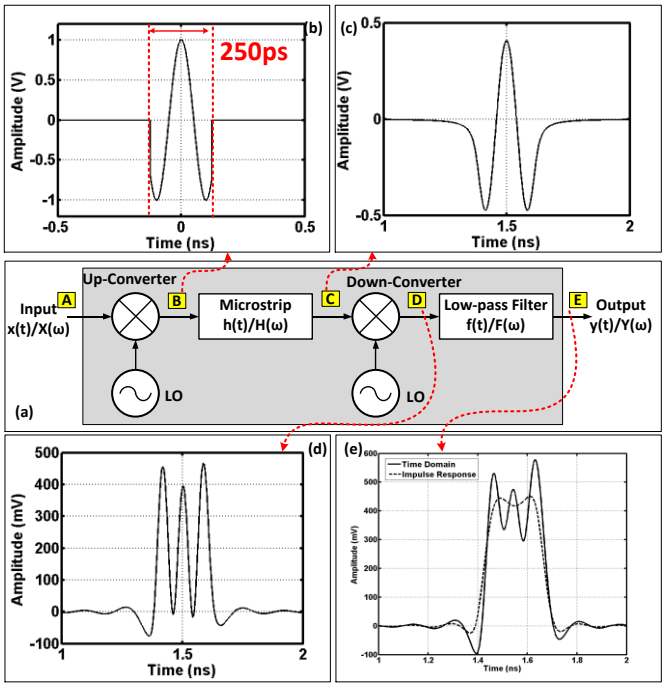

Fig. 21. (a) Block diagram. (b) Modulated pulse with 6GHz carrier frequency. (c) Carrier modulated signal after transmission line. (d) Down-converted baseband pulse with $2\omega_0$ residue. (e) Baseband pulse after LPF and comparison to pulse output calculated by impulse response.

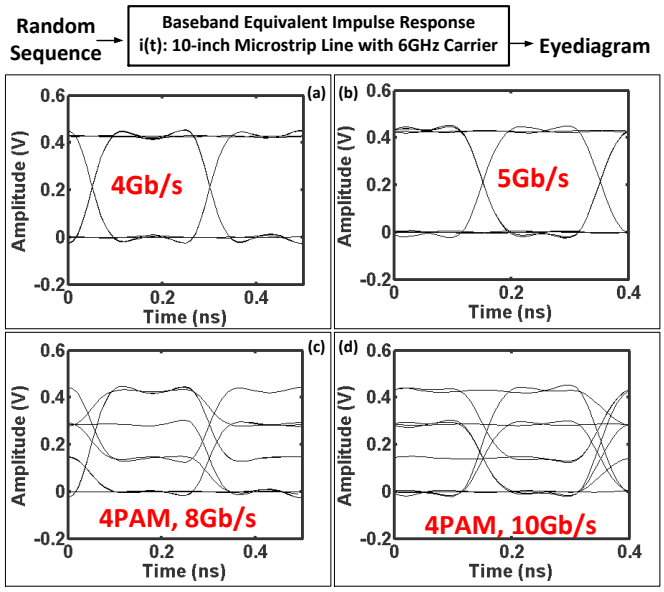

Fig. 22. (a) 4Gb/s eye-diagram. (b) 5Gb/s eye-diagram. (c) 4PAM, 8Gb/s eye-diagram. (d) 4PAM, 10Gb/s eye-diagram.

In order to prove the validity of frequency domain impulse response expression in (21), a time domain simulation is conducted by stepping through each stage in Fig. 21(a). An up-converter multiplies 250ps input pulse and 6GHz carrier signal at node B, and the modulated signal undergoes microstrip line at node C. A down-converter translates to a baseband with $2\omega_0$ residue remained at node D, and a 3rd Bessel filter with 8GHz cutoff frequency filters out the $2\omega_0$ component at node E. Comparing the output pulse in Fig. 20(c) and the output pulse from time domain simulation in Fig. 21(e), two baseband output signals are almost identical except the fact that there is a slight residue of $2\omega_0$ component left. Therefore, one can expect that the discrepancy would decrease as the cutoff frequency of LPF decreases.

Another crucial advantage of the baseband-equivalent impulse response in time domain is a capability to simulate random bit sequences as input and generate an eye-diagram. A single pulse informs on a degree of dispersion or distortion, but the measure of inter-symbol interference (ISI) requires a random bit pattern. Once impulse response is created, a sequence of randomly combined ones and zeros convolve with the impulse response and produce an eye-diagram by overlapping the output data pattern every bit period. For the given microstrip line in Fig. 17(a) and carrier frequency of 6GHz, it is clear that 5Gb/s of data stream is feasible without any equalization, as shown in Fig. 22(b). Provided SNR is high enough, 4 pulse amplitude modulation (4PAM) can double the bandwidth as shown in Fig. 22(c) and (d). Additionally, considering I and Q complex signaling at 6GHz carrier frequency, which is equivalent to 16 quadrature amplitude modulation (QAM), an aggregate data rate can reach up to 20Gb/s.

2.3.4 Effect of carrier frequency

When microstrip line parameters are fixed, conductive and dielectric loss increase as carrier frequency increases. As indicated in the frequency domain study, there is a direct trade-

off between achievable bandwidth and system SNR. In Fig. 23(a), an effective baseband bandwidth is increased to 10GHz with 10GHz of carrier frequency, but the loss magnitude is also increased to 11.2dB. In time domain, eye-diagrams of 9Gb/s random sequence in Fig. 23(b) and 18Gb/s of 4PAM random sequence in Fig. 23(d) prove the available bandwidth when the carrier frequency is 10GHz. According to this simulation, a system power budget has to be considered when choosing carrier frequency, as illustrated in Fig. 24. In the diagram, a receiver sensitivity RX_S is calculated as

$$RX_S(dBm) = -174 + 10\log(BW) + NF + SNR_{MIN} \quad (23)$$

where BW is a target data bandwidth, NF is a receiver noise figure, and SNR_{MIN} is the minimum SNR required to achieve bit error rate of less than 10^{-12} for different types of modulation scheme [44]. In order for a system to be functional under target BER, the power level after loss factor (L_{ω_0}) at particular carrier frequency has to be always larger than RX_S with enough SNR margin.

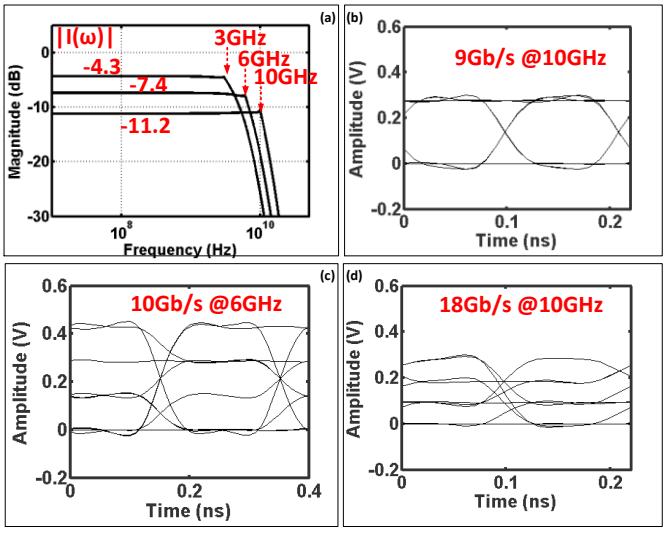

Fig. 23. (a) Impulse response with various carrier frequency. (b) 9Gb/s of eye-diagram when carrier frequency is 10GHz. (c) 4PAM, 10Gb/s eye-diagram when carrier frequency is 6GHz. (d) 4PAM, 18Gb/s eye-diagram when carrier frequency is 10GHz.

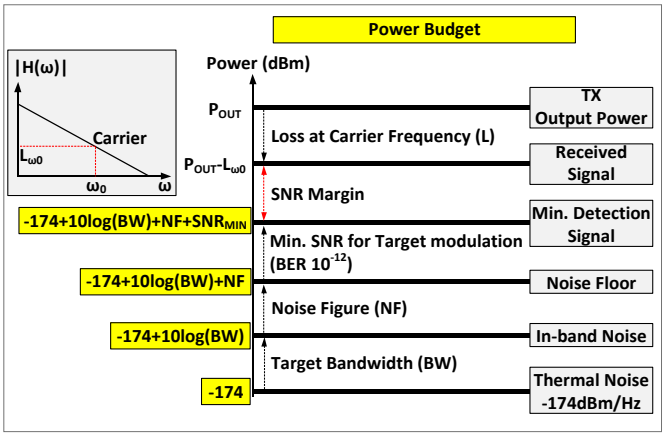

Fig. 24. System power budget calculation.

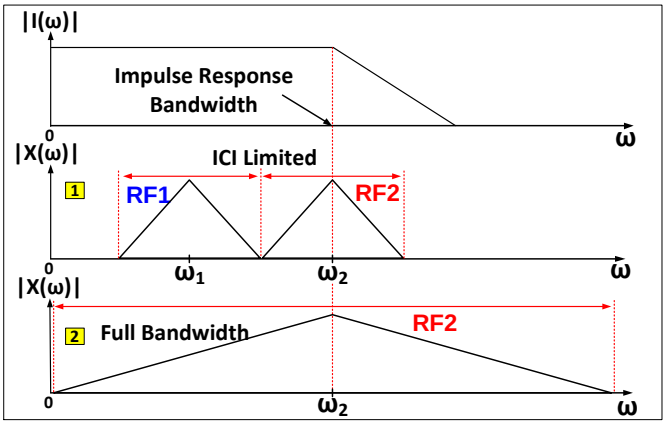

Fig. 25. Two RF channel versus one RF channel comparison when frequency response of transmission line has no discontinuity. The two RF channel case has bandwidth limitation based on ICI, but the one RF channel case can fully utilize the available bandwidth of baseband-equivalent impulse response.

Up till now, it is assumed that the frequency response of microstrip line has no discontinuity. The above study suggests the following. First, it makes no sense to increase carrier frequency indefinitely; it is preferable to increase within the system power budget to maximize available baseband-equivalent bandwidth. Second, for a system architecture perspective under this transmission line condition, as long as SNR is allowed at the highest possible carrier frequency, it is more *spectrally* efficient to utilize only one carrier frequency instead of multiple RF carriers. This concept is depicted in Fig. 25. For instance, one could decide to generate 5GHz

(ω_1) and 10GHz (ω_2) carrier frequency. However, because of ICI, each carrier may only carry a maximum bandwidth of 2.5Gb/s data, total of 5Gb/s, which is already 4Gb/s short of what single 10GHz carrier can offer. Therefore, it is more spectrally efficient to serialize data in baseband domain instead of frequency domain when a frequency response of microstrip line has no non-ideal factors such as frequency notches or ripples.

2.3.5 Microstrip line length and baseband-only signaling bandwidth consideration

Increasing communication distance will limit the bandwidth of microstrip line. The longer the channel, the smaller the bandwidth. As shown in Fig. 26(a), the loss increases as distance increases and the rate of increment in loss also increases as frequency increases because of exponential dependency in frequency response.

Using (3) and expressions from (13) to (18), frequency responses of 2,6,10-inch microstrip line are plotted in Fig. 26(b), and the bandwidth of each length is estimated at -3dB loss frequency. From the baseband-only signaling point of view, the frequency response in (3) is already impulse response in frequency domain. Thus, just as in Fig. 20(a) and Fig. 22, an inverse Fourier transform is taken from (3) first, and then random sequences are convolved with the generated impulse response in time domain to create eye-diagrams. For the case of a 2-inch microstrip line, the 3dB bandwidth reaches 14GHz, and the channel is capable of sending 14Gb/s of random sequence without any help of equalization. Therefore, in this case, there is no reason to produce a carrier frequency below 14GHz. The same principle applies to longer channels. For 6-inch and 10-inch case, baseband-only signaling is able to transfer 3.7Gb/s and 1.8Gb/s, respectively. In Fig. 26(f), the eye-diagram is almost closed when 18Gb/s of baseband-only signaling is passed through a 10-inch microstrip line, while the IQ based RFI system with carrier frequency at 10GHz can successfully transfer 18Gb/s of data as studied in Fig. 23(b).

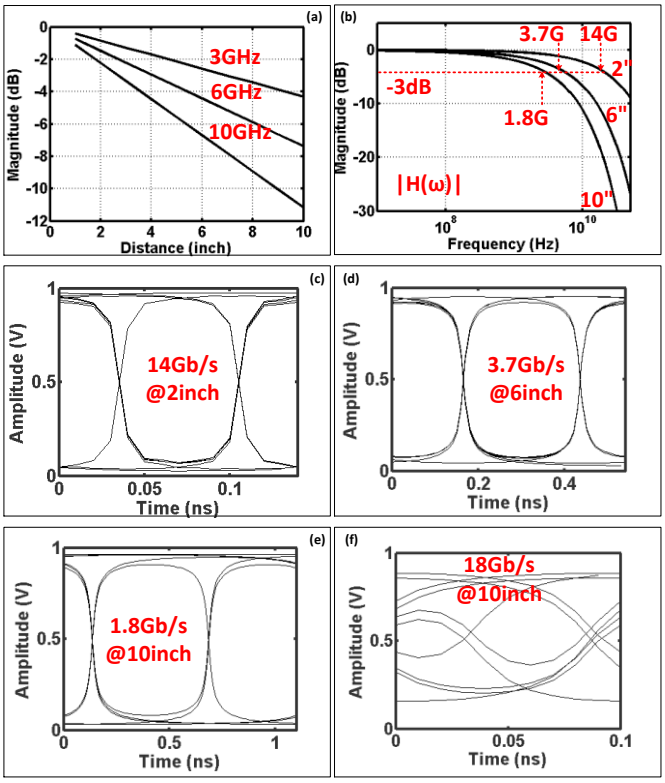

Fig. 26. (a) Loss versus distance at various frequency. (b) Frequency response of microstrip line with various length. The bandwidth of each length is estimated at -3dB loss frequency. (c) 14Gb/s baseband-only signaling over 2inch microstrip line. (d) 3.7Gb/s baseband-only signaling over 6inch microstrip line. (e) 1.8Gb/s baseband-only signaling over 10inch microstrip line. (f) 18Gb/s baseband-only signaling over 10inch microstrip line.

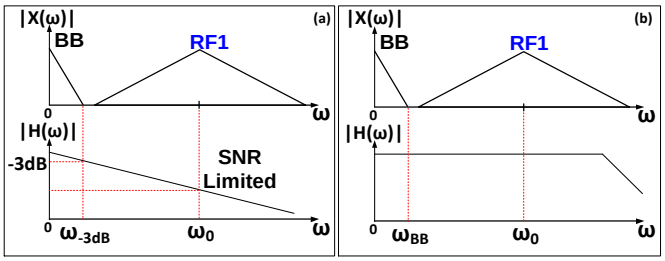

Fig. 27. Two possible cases of employing MRFI. (a) Bandwidth of baseband signaling is limited at 3dB loss frequency, then carrier modulated RF channel is generated at the maximum possible frequency where SNR is limited. (b) If channel bandwidth is so wide, there is possible case when

baseband electronics itself may cause bandwidth limitation depending on device technology. The baseband bandwidth is limited at this frequency and RF channel is employed additionally.

In order to achieve wide-open eye-diagrams, one can choose either equalization scheme based on baseband-only signaling or RFI scheme. Many equalization schemes have been proposed and are being widely exploited in industry and academia for high-speed data communication applications [45-48]. It is not the interest of this paper to compare the two system architectures nor determine at what point equalization is required, because the figure of merit, which is energy spent per achieved data bandwidth, heavily depends on device technology scaling, type of equalization, length of transmission line (loss at target bandwidth), SNR, discontinuity condition, system boundary where power consumption of components are counted in energy calculation, and more. Rather, the above studies prove that 1.8Gb/s of baseband signaling and possibly 16Gb/s (because of ICI) of I and Q signaling at 10GHz carrier frequency can be simultaneously transferred through a 10inch microstrip line without any aid of equalization scheme.

Based on this observation, two possible scenarios are drawn in Fig. 27 where MRFI can be deployed spectrally efficient. The first case is that, when the frequency response of channel rolls off, the data bandwidth of baseband signaling is limited at -3dB loss frequency, and on the top, an RF channel is inserted based on the power budget calculation. The second case assumes a channel exhibits much wider bandwidth than device technology can achieve (which would not occur very often). In other words, the bandwidth is limited by the bandwidth of device or particular circuit topology (e.g. -3dB bandwidth of amplifier) itself. In this case, depending on the bandwidth of transmission line and bandwidth of RF channel, multiple RF carriers can be also deployed.

2.4 Frequency Response With Non-Idealities

A baseband-equivalent impulse response of transmission line with non-idealities is studied in this section. As drawn with diagrams in Fig. 28(a) and measured frequency response of low-cost channel in Fig. 28(b), integrating transmission lines with circuit components requires connectors, vias, and wire-bonds that can create non-ideal effects such as destructive interference or impedance mismatch [49]. In typical situations, they limit the bandwidth of channel more definitively than conductive and dielectric loss. To study such effects, emulation and extraction of non-ideal characteristic is performed with the aid of HFSS (High-Frequency Structural Simulator) software.

2.4.1 Baseband equivalent impulse response of frequency response with non-idealities

Although the proposed method is equally valid for measured frequency responses, simulation based calculations will be introduced because of flexibility in choosing parameters of transmission line. In order to emulate non-ideal channel conditions, particularly notches and ripples, a 10-inch microstrip line (same parameters as Fig. 17(a)) is designed in HFSS with an intentional open-stub and intentional impedance mismatch at the input and output as shown in Fig. 28(c). Though not exactly same as the measured frequency response in Fig. 28(b), a similar frequency response is created from HFSS simulation in Fig. 28(d). The location of notch frequency is adjusted by the length of open-stub, and the amount of ripple is controlled by the impedance mismatch between input/output port (Z_P) and characteristic impedance (Z_0). In this simulation, notches are created at 4GHz and 12GHz, and consequently, 6GHz of 3dB bandwidth is observed centered around 8GHz.

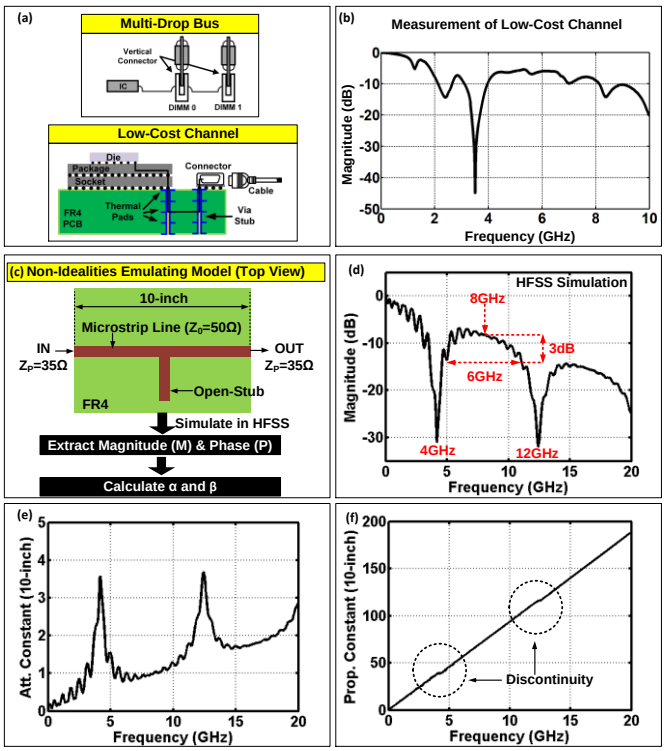

Fig. 28. (a) Diagram of multi-drop bus, and low-cost channel configuration with chip integration. (b) Measured frequency response of low-cost channel. (c) HFSS model to emulate frequency notch. Impedance mismatch is added to have ripple effect in frequency response. (d) Magnitude response simulated from HFSS. (e) Calculated attenuation constant for 10-inch distance. (f) Calculated propagation constant for 10-inch distance.

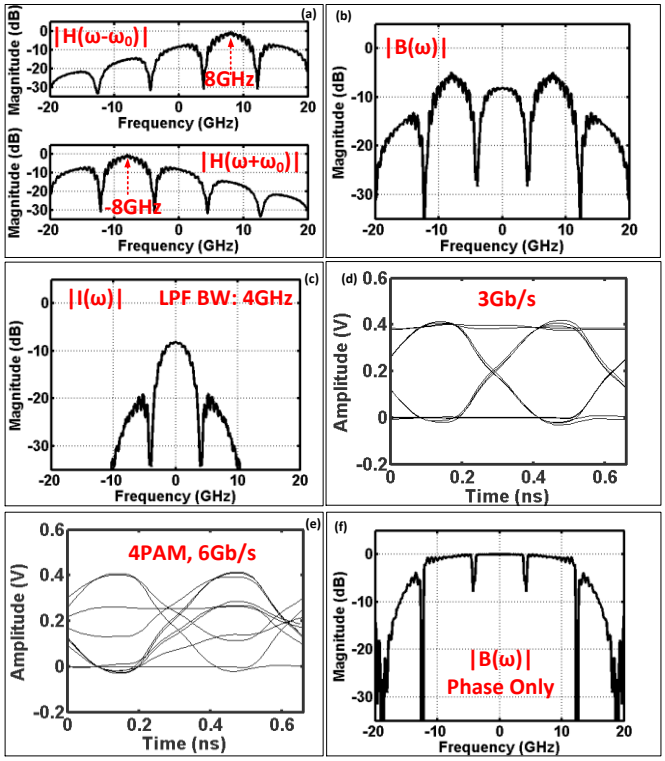

Fig. 29. (a) Frequency response shifted around carrier frequency 8GHz. (b) Baseband-equivalent impulse response without LPF. (c) Baseband-equivalent impulse response with 4GHz cutoff LPF. (d) Eye-diagram of 3Gb/s. (e) Eye-diagram of 6Gb/s with 4PAM. (f) Baseband-equivalent impulse response without LPF when only phase contribution is counted.

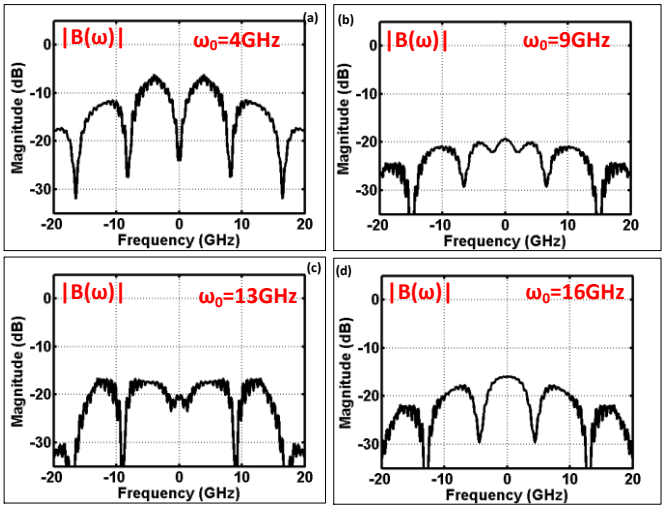

Fig. 30. Various carrier frequency. (a) Impulse response without LPF at 4GHz carrier. (b) Impulse response without LPF at 9GHz carrier. (c) Impulse response without LPF at 13GHz carrier. (d) Impulse response without LPF at 16GHz carrier.

In order to come up with a baseband-equivalent impulse response of transmission line with non-idealities, attenuation constant and propagation constant are first calculated from the HFSS simulation by following method. From the definition of electromagnetic wave propagation in (3), each of magnitude and phase contribution can be written separately as,

$$e^{-\alpha(\omega)z1} = M \quad (24)$$

$$e^{-j\beta(\omega)z1} = P \quad (25)$$

$$\alpha(\omega)z_1 = -\frac{\log(M)}{\log(e)} \quad (26)$$

$$\beta(\omega)z_1 = -P \quad (27)$$

where M is the simulated magnitude in linear scale, and P is the simulated phase both extracted from HFSS. Then, using (26) and (27), the attenuation constant and propagation constant of 10-inch microstrip line with non-idealities are plotted in Fig. 28(e) and (f). Notice that discontinuities can be found in the propagation constant around notch frequencies, which have profound effects after down-conversion for coherent systems (explained shortly).

Next, to utilize the maximum RF bandwidth for this non-ideal transmission line, a carrier frequency of 8GHz is selected and its corresponding shifted frequency responses are plotted in Fig. 29(a). In this figure, the calculated attenuation and propagation constants in Fig. 28(e) and (f) are inserted into (19) and (20). Then using (22), a baseband-equivalent impulse response without the effect of LPF is plotted in Fig. 29(b). Also, the final baseband-equivalent impulse response is shown in Fig. 29(c) after applying LPF with 4GHz cutoff frequency. As indicated with 6GHz of double-side bandwidth in Fig. 29(d), random sequences of 3Gb/s and 6Gb/s with 4PAM signaling can be successfully transferred using 8GHz carrier frequency in Fig. 29(d) and

(e). In order to study the impact of phase discontinuity mentioned in Fig. 28(f), a new baseband-equivalent impulse response is written without the contribution of attenuation constant and LPF as if the transmission line is lossless.

$$B(\omega) = e^{-j\beta(\omega+\omega_0)}e^{+j\beta(-\omega_0)} + e^{+j\beta(\omega-\omega_0)}e^{-j\beta(\omega_0)} \quad (28)$$

Interestingly in Fig. 29(f), the magnitude response of (28) also contains notches at 4GHz and 12GHz. In the case of 4GHz baseband-equivalent notch, 12GHz and 4GHz signal components will land at 4GHz and add themselves after down-conversion while carrier frequency is 8GHz. In RF signal domain, because of the phase discontinuity in Fig. 28(f), the phase of combined 12GHz and 4GHz signals becomes close to 90 degrees out of phase in relation to the phase of carrier frequency.

To study the effect of carrier frequency associated with notch frequencies, impulse responses without LPF for various carrier frequencies are plotted in Fig. 30. As expected, when carrier frequency is employed at the center of notch frequency, the baseband-equivalent impulse response would act as a high-pass filter as shown in Fig. 30(a). Impulse responses in Fig. 30(b), (c), and (d) basically point out the importance of carrier frequency. Here, only (d) appears to be feasible for high-speed data transmission within available 3dB bandwidth provided SNR is high enough.

2.4.2 Tri-band RFI system implementation using 28nm CMOS process for memory interface

A tri-band RFI system is implemented to enable 10Gb/s data communication over 2-inch microstrip line for memory interface, as shown in Fig. 31(a) [40]. In this design and experiment, notches are assumed to be generated at 1.5GHz and 4.5GHz considering practical dimension (~1-inch length) of multi-drop bus. Under this constraint, the baseband-signaling carries data strobe (DQS) and data mask (DM) signals by way of 4PAM modulation, and DQ1 through DQ8 are

transmitted by 3GHz and 6GHz carrier using 16QAM modulation with each DQ carrying 1.25Gb/s of data bandwidth.

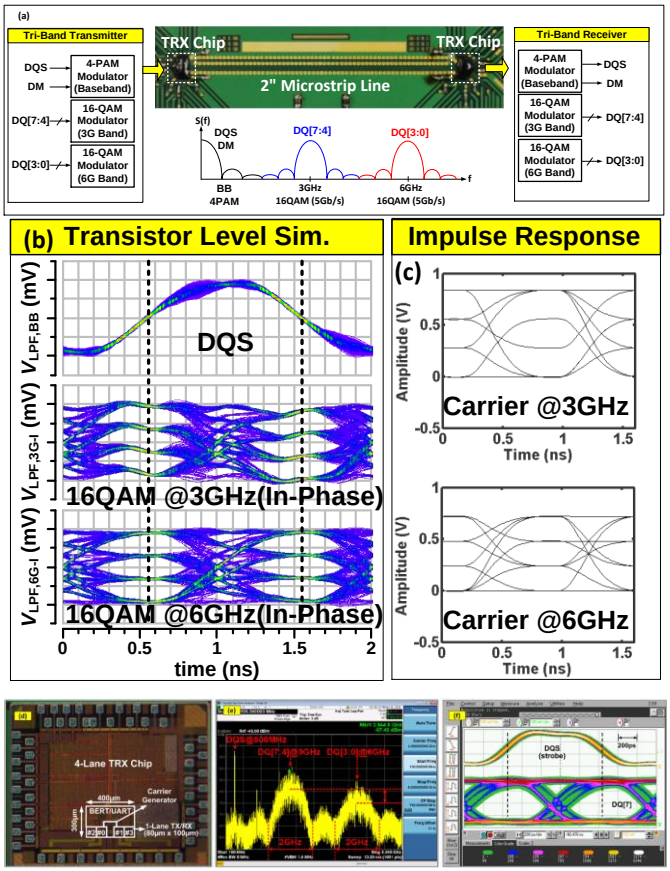

Fig. 31. (a) Tri-band (baseband, 3GHz RF, 6GHz RF) system implementation over 2-inch PCB transmission line for memory interface application. Each 3GHz and 6GHz carrier transfers 5Gb/s data rate using 16QAM modulation. Data mask and data synchronization clock is transmitted using baseband signal with 4PAM modulation. (b) Transistor level 4PAM simulation for DQS, 3GHz channel (in-phase), and 6GHz channel (in-phase). (c) Impulse response based 4PAM simulation for 3GHz channel and 6GHz channel. (d) Implemented die-photo in 28nm CMOS process.(e) Measured tri-band RFI spectrum. Data rate is 1G-baud, and the DQS clock speed is 500MHz in this spectrum. (f) Measured eye-diagram after analog-to-digital converter.

The target of the proposed system is to transfer 1-byte (8-bit) of high-speed data simultaneously over shared channel to reduce the number of pins while minimizing latency

(maximum 1 DQS period) between transmitter and receiver for memory sub-systems [50]. Regardless of spectral efficiency, one could have chosen to serialize baseband data in baseband domain using serializer and de-serializer (SerDes) to transfer 1-byte of simultaneous data, but the latency penalty caused by clock and data recovery (CDR) becomes especially challenging as data rate increases. Instead, the proposed system serializes data strobe signal, data mask signal, and data all in frequency domain to remove the necessity of CDR such that the latency requirement is satisfied for memory sub-systems.

From a system hardware requirement point of view, even if the channel does not possess notches in frequency response, multiple RF channels may still be preferred over one RF channel in this 1-byte memory bus design. For instance, as opposed to the spectral efficiency argument of multi-band MRFI in section III-D, although 1 carrier is spectrally more efficient for transmission lines without non-idealities, the ultimate question becomes whether to design 64QAM with 1 carrier or 16QAM with 2 carriers for 1-byte transmission system. Arguably, the burden on circuit implementation for 64QAM is significant enough such that one may prefer to implement a 2 carrier based RFI system.

Transistor-level simulation results (captured before ADC) show wide-open eye-diagrams of 4PAM signaling at each in-phase domain of 3GHz and 6GHz carrier in Fig. 31(b). Impulse response based 4PAM simulations agree with the transistor level simulations except the fact that $2\omega_0$ component does not exist in the impulse response as shown in Fig. 31(c). The proposed architecture is fabricated in 28nm CMOS process shown with a die-photo in Fig. 31(d). The measured spectrum of simultaneous tri-band transmission in Fig. 31(d), and eye-diagram and recovered DQS signal in Fig. 31(e) prove the concept and utility of the RFI system.

2.5 CONCLUSION

An explicit expression of baseband-equivalent impulse response in frequency domain for general transmission lines that support TEM mode of propagation is analytically derived. The frequency domain impulse response as a function of carrier frequency renders the estimation of equivalent bandwidth with indication of SNR trade-off. The impulse response reveals an equivalent pre-emphasis effect when the cut-off frequency of LPF after down-conversion is chosen properly.

Based on our explicit derivation in frequency domain, a time domain impulse response is established by taking an inverse Fourier transform. By way of time domain convolution, eye-diagrams are constructed with incoming random data sequences. In case of transmission lines without non-idealities, both frequency and time domain study suggests that only one carrier should be employed at the highest possible frequency within the SNR limit to achieve the most spectrally efficient MRFI architecture.

In order to study the baseband-equivalent impulse response of transmission lines with non-idealities, an emulation model is built in HFSS software by introducing intentional open-stub and impedance mismatch. The analysis guides how to compute attenuation and propagation constants with the help of HFSS simulations such that baseband-equivalent impulse response can be constructed by the same procedure developed in this paper. Impulse responses prove that the selection of carrier frequencies is crucial to achieve spectrally efficient multiband interconnect architecture.

Chapter 3

Ultra-Short Distance mm-Wave Wireless Communication

3.1 Introduction

Because of the increasing demand in the data bandwidth for multimedia applications, the industry has come up with new interconnect solutions such as Thunderbolt, USB3.0, Display Port, HDMI, and Gigabit Ethernet. The data rate of 10Gb/s per channel is no longer uncommon in the consumer market. However, as each interconnect standard evolves, serious challenges remain in its bandwidth scalability, power, and other fundamental physical limitations such as mechanical reliability, thermal constraints, and overall system form-factor. Often times, connectors play important role in each generation because of its non-scalable nature and inherent discontinuities between physical layers. The non-ideal behavior makes the high-speed signal undergoing distortion, inter-symbol interference (ISI), and reduced signal-to-noise ratio (SNR). Although, one can invest more resource in packaging and connector technologies [51], much effort is focused on the digital signal processing based pre-emphasis and equalization, which leads to a complicated transceiver architecture requiring calibration, software, and more power.

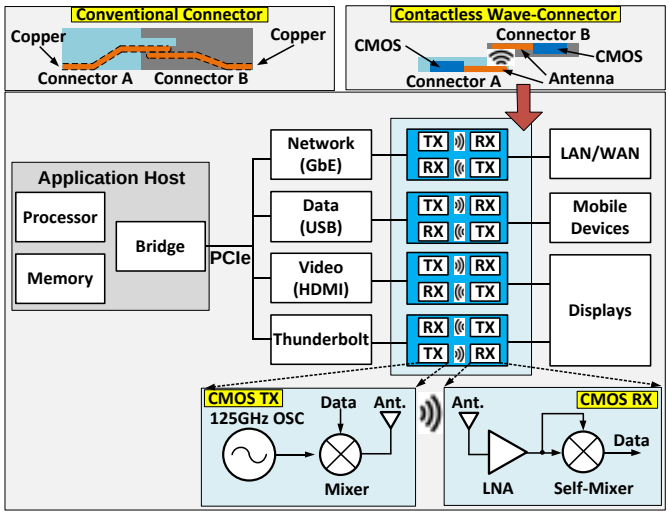

Fig. 32. Conceptual diagram of conventional connector, contactless wave-connector, and block diagram of overall system where the contactless wave-connectors can replace conventional mechanical connectors.

Meanwhile, a recent research suggested to remove the physical connection and replace it with short-distance wireless connectors [52]. The fundamental advantage comes from an available wide fractional bandwidth around a carrier frequency and its non-contacting air-interface. The contactless wave-connector (CWC) can be installed essentially anywhere in a given network topology as illustrated in Fig. 32, for instance, between network port and LAN/WAN cables, USB port and mobile devices, and HDMI port and display monitors. In the proposed approach, the CMOS TX chipset generates an OOK modulated 125GHz carrier signal, and the TX PCB antenna radiates electromagnetic energy to the reciprocal RX PCB antenna. Then, similar to [44], the CMOS RX chipset amplifies the modulated signal and down-converts to the baseband signal through a self-mixer without using frequency-synthesizer/carrier-synchronization.

3.2 125GHz ANTENNA DESIGN ON FR4 PCB AND CHIP-to-ANTENNA FLIP-CHIP ASSEMBLY

Before designing the antenna structure, we first characterized the FR4HR substrate by designing transmission line (TL) calibration structure [53]. By measuring scattering parameters of different length of TL through a vector network analyzer, we extracted the dielectric constant of 3mil and10mil thickness substrate up to 67GHz and extrapolated up to 200GHz as shown in Fig. 33(a). For the loss tangent, we used a manufacturer provided data up to 10GHz and again extrapolated up to 200GHz shown in Fig. 33(b).

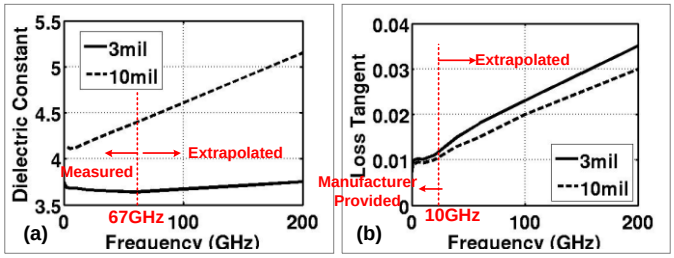

Fig. 33. (a) Measured and extrapolated dielectric constant of FR4HR substrate used for simulation. (b) Manufacturer provided and extrapolated loss tangent of FR4HR substrate.

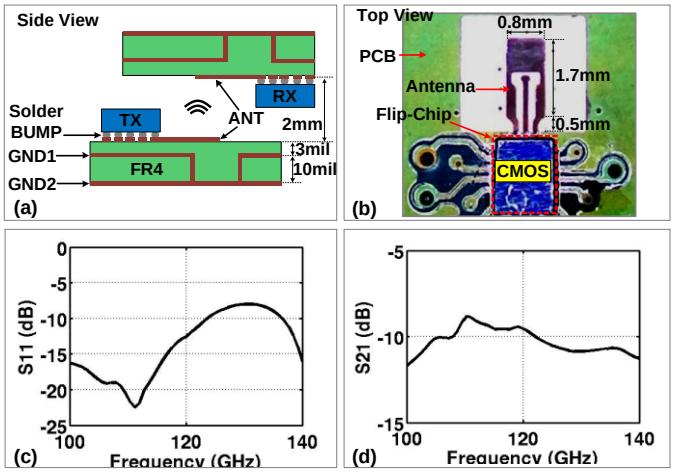

Fig. 34. (a) Side view of TX to RX air-coupling, chip-to-antenna flip-chip assembly, and illustration of ground plane for impedance matching. (b) Top view of assembled module. (c) Simulated S11 looking into the antenna port. (d) Simulated one antenna to the other side of antenna air-coupling loss performance.

The TX to RX air-coupling scheme is depicted in Fig 3(a). A 125GHz folded-dipole antenna is designed on the substrate that was measured above. A ground plane (GND2) is placed 13mil underneath the antenna to act as a reflecting surface (close to the quarter lambda at 125GHz). With the ground plane specified, the antenna dimension is designed to match with 100Ω differential impedance. Then, a 1.7mm by 0.8mm rectangular cavity is formed by a via-wall to provide a higher directivity.

The CMOS chips are directly mounted by a flip-chip process, and a 0.5mm length of TL connects the chip and antenna with a 3mil-depth ground plane (GND1) to maintain 100ohm

differential characteristic impedance. The top view of assembled module is shown in Fig. 34(b) emphasizing the chip and antenna together can fit within 1mm by 3mm area. Looking into the antenna port, the return loss (S11) maintains below -8dB over 40GHz bandwidth. In addition, the transmission performance (S21) between the TX antenna to the RX antenna through 2mm air-coupling experiences no worse than 12dB loss over 40GHz bandwidth. Notice how the amplitude variation is confined within 4dB as opposed to the conventional mechanical connector may induce more than 30dB of notch in frequency response [54]. The above study indicates that the proposed air-coupling channel can transmit more than 20Gb/s of baseband data without requiring power hungry equalization or pre-emphasis.

3.3 125GHz CMOS TRANSMITTER

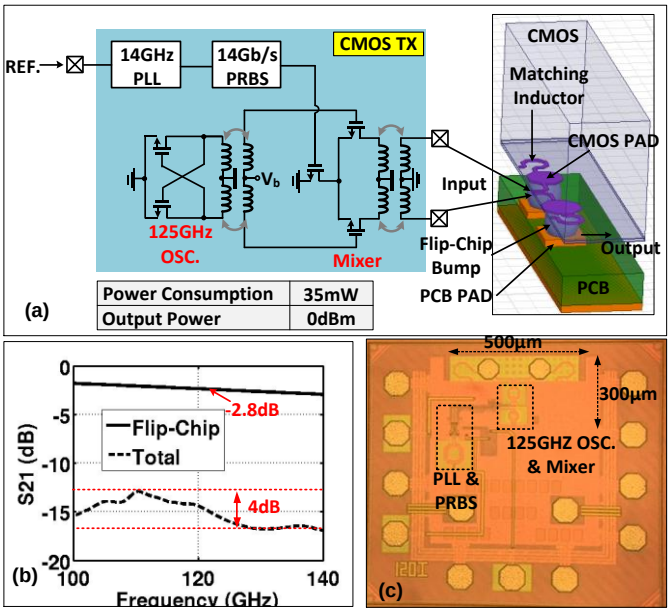

Fig. 35. (a) Schematic of proposed transmitter and flip-chip 3D model. (b) Flip-chip transmission loss, and complete link transmission performance including TX and RX side of flip-chip/antenna and 2mm air-coupling channel. (c) Transmitter die-photo.

The TX adapts an OOK modulation to enable an energy-efficient architecture. An on-chip Pseudo Random Bit Sequence (PRBS) (2^7-1) generates 14Gb/s data stream, which is

clocked by an on-chip 14GHz phase-locked loop (PLL), and drives a mixer's tail current device. In order to perform the up-conversion, a free-running oscillator first generates 125GHz carrier signal and drives the mixer's differential pair through a transformer. After the up-conversion, the mixer directly drives the off-chip feed-line and antenna through a transformer without using an additional power amplifier (PA) as shown in Fig. 35 (a). From the link budget study explained in the next section, we intentionally avoided designing PA. That is, the oscillator generates enough power to transfer energy to the RX through an air-coupling channel. For the CMOS-to-PCB flip-chip assembly, we had to increase the on-chip pad size to 100μm diameter, in return adding significant amount of capacitance compared to a design library based pad. To perform an output matching with this constraint, we implemented a pad-tapped shunt inductor. From the HFSS simulation, CMOS-pad/flip-chip-bump (80μm diameter)/PCB-pad contributes 2.8dB loss. Adding from the result of TX antenna to RX antenna in Fig. 34(d), the final end-to-end transmission efficiency becomes 16dB at 125GHz. Here again, the amplitude of S21 maintains within 4dB variation over 40GHz span. The TX generates 0dBm output power at the input of on-chip pad while consuming 35mW of power. A die-photo is taken in Fig. 35(c).

3.4 125GHz CMOS RECEIVER

The RX starts with a matching transformer and provides 10dB of gain via a 1-stage low-noise amplifier (LNA) as shown in Fig. 36(a). The link budget analysis in Fig. 36(b) reveals that the noise floor of RX begins at -70dBm considering the 28GHz bandwidth (double-side band of 14Gb/s data). Going through 15~19dB transmission loss, -20dBm signal arrives at the RX front-end. The LNA amplifies the signal up at -10dBm, and the front-end adds 10dB of noise figure. In addition, a 15dB of minimum SNR is added to the floor to achieve a bit-error-rate (BER) of 10^{-12} for the non-coherent OOK de-modulation. Although the -10dBm modulated signal further

undergoes 21dB of self-mixing conversion loss (Fig. 36(d)), with the updated noise floor at -45dBm, the system has room for another 14dB of SNR margin. Unlike the resistor loaded self-mixer design in [44], we employed a feedback amplifier based self-mixer in order to deliver a wider down-conversion bandwidth. Lastly, high-speed buffers amplify the down-converted 14Gb/s baseband signal and drive a scope for an eye-diagram measurement. The RX consumes 25mW, and its die-photo is shown in Fig. 36(e).

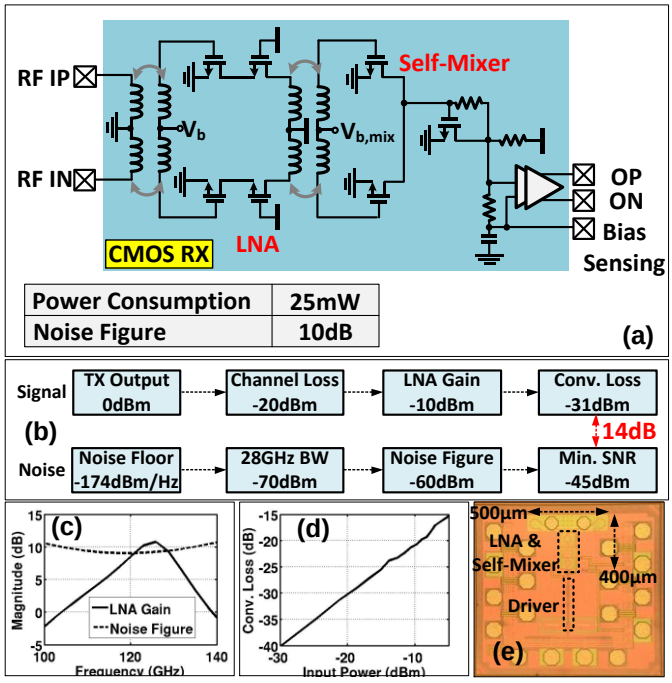

Fig. 36. (a) Schematic of proposed receiver including 1-stage low-noise amplifier and feedback based self-mixer. (b) Link budget analysis. (c) LNA gain. (d) Self-mixer conversion loss. (e) Receiver die-photo.

3.5 TX 125GHZ OUTPUT SPECTRUM AND TRANSCEIVER DATA LINK MEASUREMENT RESULTS

To demonstrate the radiated power from the TX, first we measured the modulated output spectrum using W-band horn antenna and harmonic mixer shown in Fig. 37(a). Although, 125GHz is actually not within the W-band region, given the output power from the TX and the

conversion loss from the harmonic mixer, we were able to capture the TX output spectrum and confirmed that indeed there is carrier signal power at 124.7GHz and modulated sideband as shown in Fig. 37(b). After confirming radiated power with modulation, we setup the TX and RX data link as shown in Fig. 37(c). First, 55MHz reference clock is provided for the 14GHz PLL to be locked. The same 55MHz reference clock is used for triggering an oscilloscope. Then, the RX is placed underneath the TX with a 2mm air-gap. The down-converted and amplified signal is fed into the scope to measure the 14Gb/s of eye-diagram as shown in Fig. 37(d). As the wide-opened eye-diagram indicates, there is a margin to go beyond 14Gb/s.

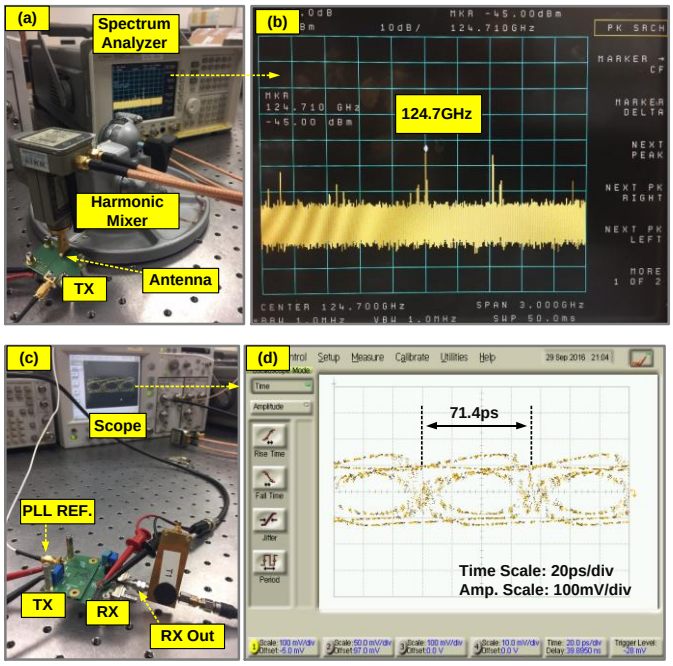

Fig. 37. (a) TX output spectrum measurement setup. (b) Captured TX output spectrum. (c) TX and RX data link setup with 2mm air-gap. (d) Measured 14Gb/s eye-diagram.

3.6 CONCLUSION

In this work, we have demonstrated a contactless wave-connector for consumer oriented interconnect solutions to provide wide-bandwidth and reduce form factor and power consumption. The demonstrated 125GHz TX and RX module combined with a PCB antenna

achieves 14Gb/s of data rate without using complex and power hungry equalization circuits. The TX and RX chips are implemented in TSMC 65nm CMOS technology and occupies 0.5mm x 0.3mm of TX and 0.5mm x 0.4mm of RX silicon area. The TX and RX consumes 35mW and 25mW of DC power, respectively, achieving 4.28pJ/bit energy efficiency.

Chapter 4

mm-Wave-Guide Communication Using Hollow Tube

4.1 Introduction

Global Data Centers continue to demand better energy efficiency (in terms of pJ/bit/m) data links for short range (1-100m) inter-server/container communications. Optical fiber links dominate current markets for high data rates and flexible deployment. However, they are hardly energy-efficient because they necessitate electrical-to-optical (E2O) and optical-to-electrical (O2E) operations by using discrete and temperature-constrained III-V compound lasers and detectors [55]. Copper-based active cable standards, such as Thunderbolt and 10GBASE-T, are rapidly replacing optical fibers for short distance communications by eliminating E2O/O2E in such markets, but still dissipate from hundreds of milli-watts to a few watts by adapting power-hungry DSP with pre-distortion/equalization [56–57]. On the other hand, dielectric waveguides have been investigated in the past for mm-Wave communications even before the invention of fiber-optical communications [58]. However, those investigations did not lead to any useful data link development due to the following reasons: 1) the cut-off frequency of electronic devices (especially the silicon-based technologies) was too low to reach the required mm-wave transceiver implementation with sufficiently wide communication bandwidth; 2) the dielectric loss for mm-Wave transmission was substantially higher than that of optical fiber for long haul communications. However, such disadvantages no longer hold true due to the rapid development of mm-Wave CMOS transceiver technology in recent years and the fast market growth of Data Centers which require vastly on inter-server/container communications mostly within 100 meters. In this work, we propose an energy/cost-efficient (<1pJ/bit/m) data link by using low-power mm-Wave transceivers and low-cost hollow plastic cable (or “Wave Cable”). Such data link would

eliminate O2E/E2O conversion processes and pave the road for greener and fully silicon based data links for short distance (1-100meter) inter-server/container communications within fast growing worldwide Data Centers.

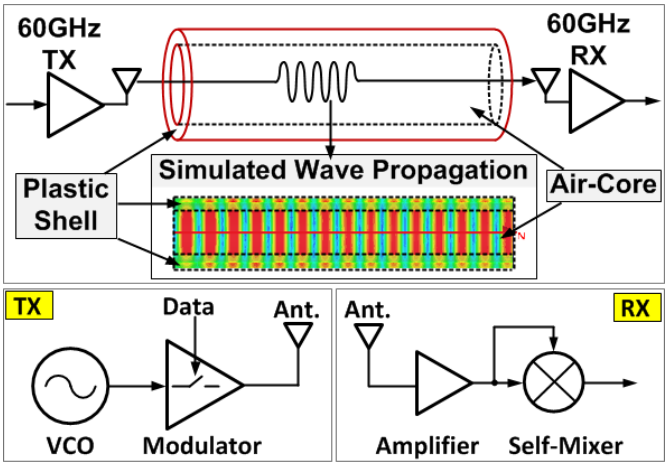

Fig. 38. Wave Cable transceiver diagrams with an air-core hollow plastic waveguide.

4.2 Proposed System Architecture

The revival of mm-Wave communications through wires (or waveguides) originated from the development of very short distance (up to 30cm for example) RF-Interconnect (RFI). Although previous works mainly focused on communications over copper wires, which exhibit a low-pass characteristic, the carrier-modulated communication is better-suited for transmission media with high-pass channel characteristics. Consequently, Sony researchers have started the use of solid plastic waveguide for very short distance interconnects on board (up to 30cm) for multiband mm-Wave communications [57]. Nevertheless, their proposed solid plastic waveguide was rectangular which was not intended for the single-mode operation and was limited in link-distance due to the high dielectric loss of polyethylene at mm-Wave frequencies. To alleviate such disadvantages, we propose to 1) replace the solid rectangular waveguide with a hollow plastic cable to transmit energy mostly within the air-core; 2) maintain mm-Wave signal through

a cylindrical cable under a circular HE11 single-mode operation [58-59]. The proposed data link via a hollow plastic cable is explained in Fig.38. It contains 60GHz CMOS transceivers based on non-coherent amplitude shift keying (ASK) with off-chip but in-package wire-bonded dipole antenna as part of the signal coupling device (Fig.38). The antenna is designed with emphasis on efficient near-field coupling. Due to the lower dielectric loss/dispersion of the air-core, the Wave Cable can achieve a longer communication range with substantially improved link efficiency.

4.3 POWER BUDGET AND IMPLEMENTATION

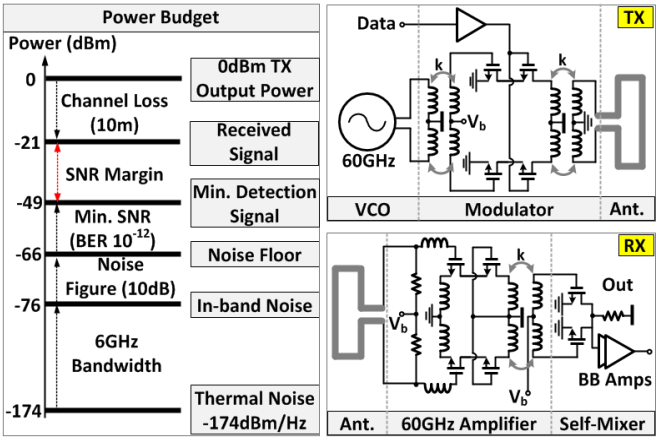

Fig. 39. Wave Cable system power budget and transceiver schematics.

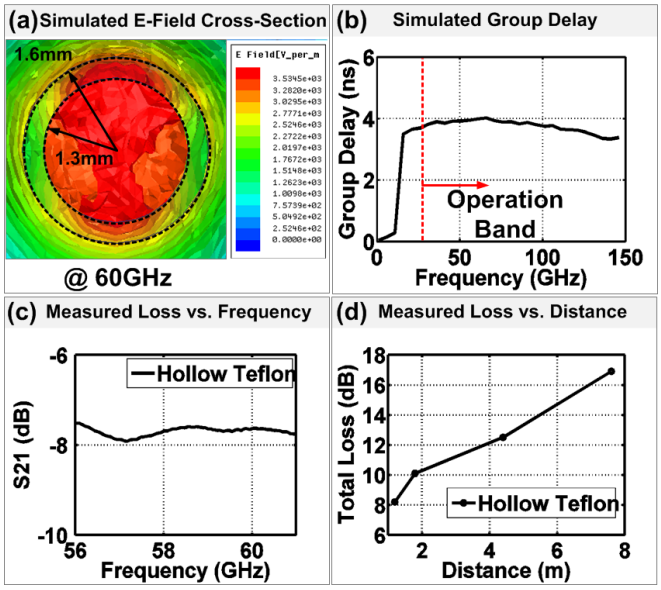

Fig. 40. (a) Simulated cross-section E-Field. (b) Attenuation factor ratio vs. inner/outer radius ratio. (c) Measured insertion loss comparison. (d) Measured total loss for incrementing distance.

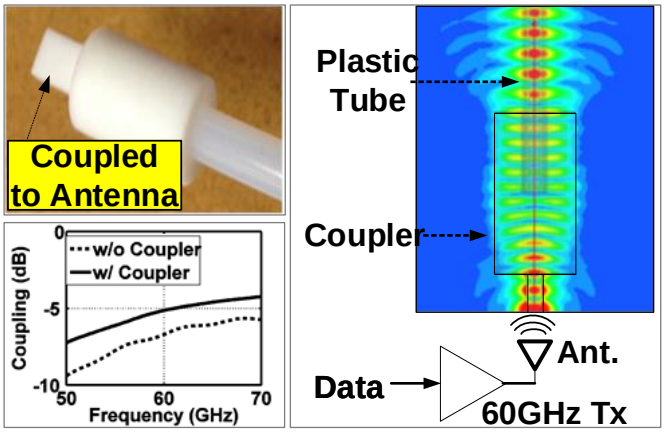

Fig. 41. Hollow tube transition-coupler design, simulated coupler loss, and transition diagram with simulated E-field result.

Fig. 39 describes the system power budget and corresponding Tx/Rx schematics. For the first prototype, we aim for the communication distance within 10m. First of all, the Tx delivers 0dBm of output power, and the receiver senses -21dBm assuming the channel undergoes 1.5dB loss per meter. Significant part of the channel loss is caused by Tx-to-cable and cable-to-Rx couplings, primarily due to Omni-directional Tx/Rx antenna designs. With 6GHz of system bandwidth and 10dB of noise figure, the Rx in-band thermal noise floor is -66dBm. To acquire the bit error rate (BER) of less than 10^{-12}, the non-coherent ASK Rx requires a minimum 17dB of signal-to-noise ratio (SNR). The minimum detectable power is now -49dBm. Therefore, the SNR margin becomes 28dB, which indicates that the system is not limited by the thermal noise. The Tx contains an LC-based oscillator free-running at 60GHz, an ASK modulator, an on-chip transformer, and an off-chip coupling antenna. The oscillator drives the current generating device via an on-chip transformer, and the switch device turns the current flow on and off to complete the ASK modulation. The Rx begins with a reciprocal antenna as a coupling device with the

measured return loss of -10dB within the bandwidth, and the 60GHz amplifier provides the voltage gain of 18dB. Next, the self-mixer cancels the carrier signal to extract the envelope of the modulated signal, and baseband amplifiers boost up the demodulated signal before the output driver.

4.4 CHARACTERISTICS OF HOLLOW PLASTIC WAVEGUIDE

To understand the channel behavior, the dispersion relation and power loss are discussed. As shown in Fig. 40(a), from the cross-section view, the boundaries are divided into 3 regions; a hollow air-core (radius of 1.3mm), a plastic shell (radius of 1.6mm), and an outermost side of air. We examined the property of field propagation using a 3D full-wave simulator. With the diameter of ~λ/2 at 60GHz, the hollow plastic fiber can guide the most energy through the center air-core area. The cable's dispersion behavior is implicated by its group delay as shown in Fig. 40(b). As the frequency of operation increases beyond 30GHz, the group velocity becomes relatively constant and suits broadband communications well. Fig. 40(c) and (d) summarize the signal transmission characteristics of hollow Teflon cable. We first measure the insertion loss of a 1.2m cable with a network analyzer. Including the calibrated 6dB antenna coupling loss, the cable exhibits a total loss of 7.5dB at the frequency of 60GHz, and the in-band ripple is measured to be less than 1dB. We also estimate the power loss for various cable distances, and data shows total 17dB loss for 7.6m long cable.

4.5 COUPLER DESIGN AND MEASUREMENT

Fig. 41 illustrates the physical structure of the chip-to-cable transition-coupler made of the same plastics (Teflon) as that of the hollow cable. On the transmitter side, its rectangular tip would receive electromagnetic energy from the Tx-antenna via the near-field coupling and then

pass that to the Teflon cable. On the receiver side, it would work reciprocally to convey energy from the cable to Rx-antenna. Such EM-energy transition behavior is clearly depicted through Ansoft HFSS simulations. Since the chip-to-cable (or cable-to-chip) transition occurs via the near-field coupling, the coupler can be simply placed atop in-package antenna as indicated in Fig.41. The simulated coupler loss is 5~6dB. It is due to the use of Omni-directional antenna and can be further reduced with more directional designs. Unlike the optical fiber, the chip to coupler alignment can be conducted straightforwardly without using special equipment. The data link prototype exhibits a data rate of 6Gb/s at the distance of 2m, and degrades to 3.3Gb/s at the distance of 7.6m. This is validated according to received eye-diagrams of 2^{15}-1 PRBS data with measured Rx sensitivity (-17dBm) in Fig. 42. The data rate reduction primarily comes from 1) additional signal dispersion caused by longer transmission distance; 2) long plastic cable needed to be bent with extra 1~2dB power loss for the convenience of BER testing. The aforementioned issues can be further improved by implementing Tx signal pre-distortion and/or surrounding the Teflon cable shell with cladding dielectric structures for better focused energy within the air-core.

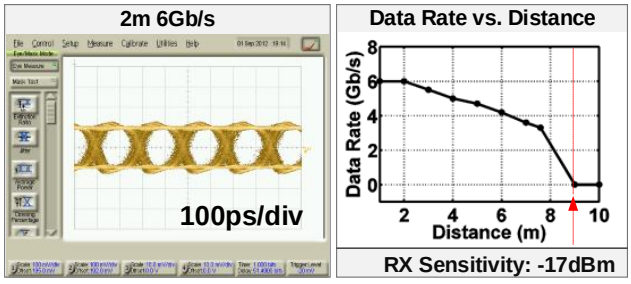

Fig. 42. Measured eye-diagram and Rx sensitivity under 2^{15}-1 PRBS with BER < 10^{-12}

	This Work	ISSCC 2012 [1]	Thunderbolt (Intersil) [2]	ISSCC 2012 [3]	ISSCC 2012 [4]
Distance (m)	7.6	N/A	3	100	0.12
Channel	Plastic (Hollow)	Fiber	Copper	UTP	Plastic (Solid Rect.)
Data Rate (Gb/s)	3.3	23	10	10	26
Link Type	P2P	P2P	P2P	P2P	P2P
Power (mW)	28	1830	450	2000	137
FoM (pJ/b/m)	1.11	N/A	15	2	43.9
Technology	65nm CMOS	40nm CMOS	40nm CMOS	40nm CMOS	40nm CMOS
Technology Scaled FoM	0.69	N/A	15	2	43.9

Fig. 43. Performance summary and comparison with prior arts.

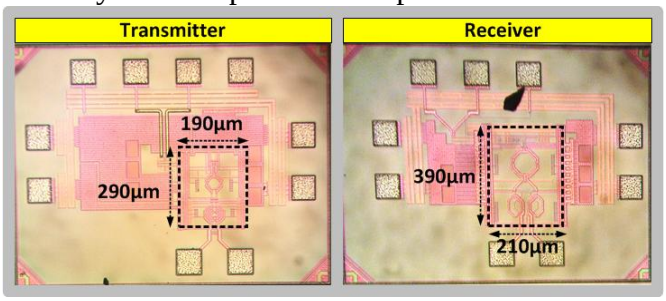

Fig. 44. Die photo of (a) Wave Cable transmitter and (b) Wave Cable receiver.

4.6 CONCLUSION

We have designed and characterized the Wave Cable transceiver systems for short distance data links. The entire transceiver and channel characteristics have been simulated and agrees well with the measurement results. We have achieved the maximum data throughput of 6Gb/s at 2m and the maximum communication distance of 7.6m with 3.3Gb/s while the BER is less than 10^{-12}. The TRX consumes 28mW (Tx:12mW, Rx:16mW), and have accomplished a Figure-of-Merit (energy per bit per meter) by a factor of 2.9~63 better than that of prior arts, as compared in Fig. 43. The die-photos for both Tx and Rx are shown in Fig. 44(a) and (b), respectively. The demonstrated silicon-only CMOS transceiver is also more adaptable for green data center operations due to its wider temperature tolerance (in contrast to $<5^{o}$C operation window for typical III-V lasers) and higher system integration which lead to more compact link systems.

Chapter 5

Metal-Coated Flexible Dielectric Waveguide for Millimeter-Wave Multi-Lane Wireline Communication

5.1. Introduction

Dielectric waveguides have gained attention in recent years because of their low-loss characteristic at millimeter-wavelengths (mm-wave) and their potential deployment in high-speed wireline communication applications [60-61]. Popular dielectric materials for these links include Polyethylene (PE), Polystyrene (PS), and Teflon (PTFE). These non-polar polymer materials exhibit loss tangents of 0.0003~0.001 and dielectric constants (ε_r) of 2.1~2.6 [62]. Additionally, they are flexible. In order to improve the loss factor, various waveguide cross-sectional configurations have been suggested: circular hollow-tubes, rectangular ribbons, and rectangular hollow-tubes. The common idea of these approaches is to transfer electromagnetic (EM) energy by means of a leaky-wave along the waveguide in a fashion where the majority of the EM wave's energy propagates through dry-air. However, such a waveguide cannot confine the EM energy and thus, becomes vulnerable to the surrounding environment.

One possible solution is to incorporate low-loss Styrofoam cladding around the waveguide; however, the diameter of cross-section turns out to be impractical (explained shortly). Another potential approach is to insert high-dielectric constant and low-loss materials into a dielectric tube (PE, PS, PTFE) so that EM field is concentrated in the core. Sample materials are alumina ($\varepsilon_r = 9.7$), sapphire ($\varepsilon_r = 9.3\sim11.7$), and quartz ($\varepsilon_r = 3.8\sim4.8$). Unfortunately, these crystalline materials are brittle, and tend to break when the cable is flexed. Another approach reported in [63] was to fill a dielectric tube with high-dielectric constant powder so that the waveguide remains flexible while EM field is focused at the center. The major challenge of this

approach is that the effective dielectric constant heavily depends on the density of powder, and is extremely sensitive to discontinuities in density throughout the powder within waveguide. In other words, the waveguide cannot be considered homogeneous, and will exhibit scattering losses and multi-mode propagation.

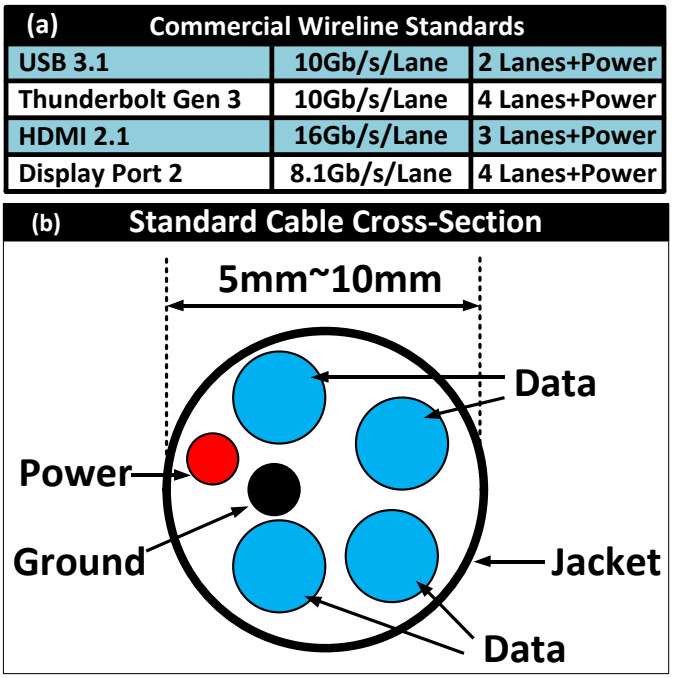

Fig. 45. (a) Several popular commercially available wireline standards. (b) Diagram of typical cable cross-section for these wireline standards.

In order for waveguides to be adopted by the wireline communication market, they must offer compatibility with the existing standards and physical infrastructure. Examples of commercially available wireline standards (USB, Thunderbolt, HDMI, Display Port) are summarized in Fig. 45(a). Each of these standards carries multiple data lanes in order to increase aggregate data rate as well as provides a power lane to support mobile electronics. For instance, as shown in Fig. 45(b), all of the data and power lanes are packed within 5mm~10mm cross-sectional form-factor, which means that each data lane's cross-sectional diameter must be within

1mm~2mm. The Styrofoam cladding approach fails to address this important requirement, limiting its applicability in replacing existing copper-wire based standard cables.

In this work, we propose a metal-coated flexible dielectric waveguide operating at millimeter-wavelengths to address the field confinement while still providing the physical flexibility required for wireline cables. Metal-plating has been widely employed in low-cost filters and antennas constructed using 3-dimensional printing technology, as it offers excellent compatibility with the underlying fabrication process [64-65]. This metal-plating method is applied to the proposed waveguides to demonstrate their potential in high-speed wireline communication while remaining compatible with large volume manufacturing.

5.2 Metal Skin Depth and Implementation of Copper-Coated Dielectric Waveguide

The skin-depth (δ_s) of a non-ideal conductor, which is defined as depth of EM field penetration, and the corresponding EM field magnitude (E) inside conductor over the metal thickness are expressed as the following [22].

$$\delta_s = \frac{1}{\alpha} = \sqrt{\frac{2}{\omega\mu\sigma}} \qquad (1)$$

$$E = e^{-\alpha x} \qquad (2)$$

where α is attenuation constant, ω is radian frequency, σ is conductivity, μ is magnetic permeability, and x is metal thickness. The expression (2) specifies that the EM field magnitude becomes 36.8% at 1 skin-depth thickness. According to (1), and as illustrated in Fig. 46(a), the skin-depth of commonly available conductors (aluminum, copper, gold, silver) are in the range of 0.1μm~0.5μm from 30GHz to 300GHz. Using the data at 60GHz from Fig. 46(a) and expression (2), the percentage of EM field magnitude is plotted over the metal thickness in Fig.

46(b). At the thickness of 3μm, which is roughly 10~20 skin-depth, only 0.001% of the EM field remains, indicating the EM energy is effectively confined in waveguide.

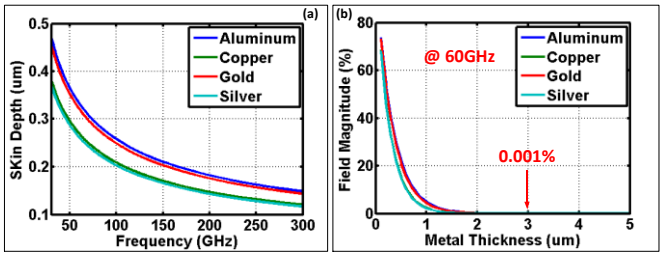

Fig. 46. (a) Skin-depth of various metal material at millimeter-wavelengths. (b) Percentage of EM field magnitude left over vs. metal thickness at 60GHz. Note that even less metal thickness is required to confine the EM field for higher frequency of operation.

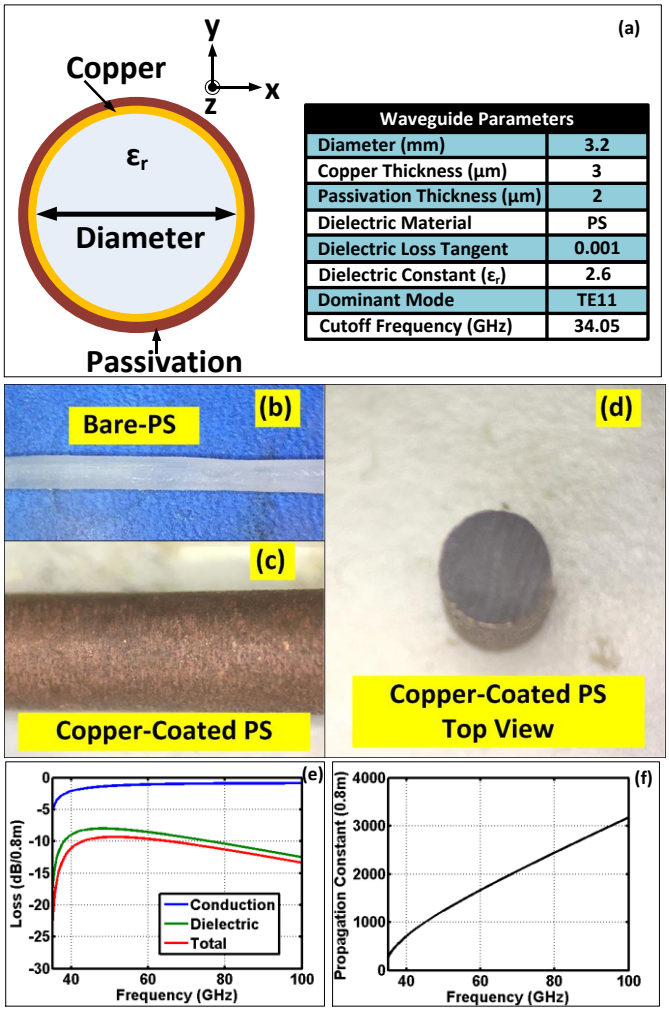

Fig. 47. (a) Cross-sectional diagram of copper-coated PS waveguide and its parameters. Direction of propagation is in the z-axis. (b) Bare-PS dielectric waveguide side view. (c) Implemented copper-coated PS waveguide side view. (d) Copper-coated PS waveguide top view. (e) Analytically determined losses for 0.8-meter. (f) Analytically determined propagation constant.

Based on this analysis, a prototype of 3μm thickness copper-coated PS waveguide is implemented, and its parameters are summarized in Fig. 47. Note that the shape of waveguide can also be circular hollow-tube with a higher cutoff frequency for the same cross-sectional diameter [66]. Although, the diameter of 3.2mm (cutoff frequency of 34.05GHz) is chosen to utilize 60GHz CMOS transceiver module designed by authors [3], in practice, higher carrier frequencies (>100GHz) with less than 2mm of cross-sectional diameter are more desirable for commercial applications as depicted in Fig. 45(b). As copper oxidizes freely in air, an extra 2μm of passivation material is deposited on top of the copper layer. According to the analytical expressions of dielectric-filled circular copper waveguide in Fig. 47(d), the total loss factor of dominant mode of propagation (TE11) over 0.8-meter distance is 9.6dB at 60GHz while the loss tangent of PS is 0.001. As the operating frequency increases, the conduction losses approach a constant value since the EM wave begins to propagates in a transverse electromagnetic (TEM) fashion. Alternatively, the dielectric losses increase with frequency and become the dominant source of loss. In Fig. 47(e), the non-linear propagation constant around the cutoff frequency indicates that the dispersion will eventually limit the data rate.

5.3 MEASUREMENT

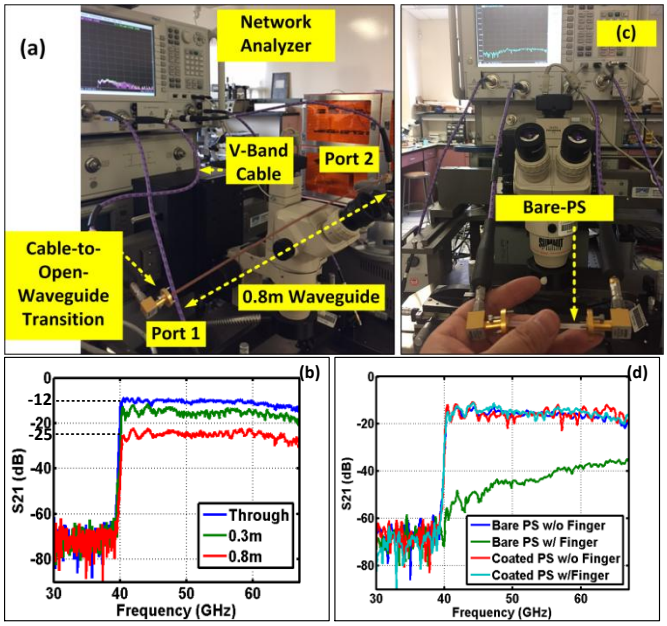

Fig. 48. (a) Waveguide characterization setup using vector network analyzer and cable-to-open-waveguide transition. (b) Measured S-parameters of copper-coated PS waveguides. (c) Measured S-parameters of bare-PS waveguide while touching the PS with finger. (d) Measured S-parameters of bare-PS and copper-coated PS with and without fingers on waveguide.

We first characterize the transmission performance of the implemented copper-coated waveguide using vector network analyzer as shown in Fig. 48(a). In this setup, a rectangular coax-to-open-waveguide transition with cutoff frequency of 40GHz is connected to a V-band cable in order to excite the copper-coated waveguide. In order to de-embed the setup losses of the V-cable and waveguide transition, a 'through' measurement of open-waveguide to open-waveguide was first performed. In Fig. 48(b), the measured data shows 12dB of loss in the 60GHz regime. Next, 0.3m and 0.8m sections of copper-coated waveguide are inserted between two open-waveguides. At 60GHz, the copper-coated waveguide exhibits 25dB of loss, which means that the true waveguide offers 13dB of loss over the 0.8m section. Compared to the analytical study of Fig. 47(d), the implemented copper-coated waveguide suffers 4dB excess

losses over the analysis. This discrepancy can be attributed to the analytical model, not including the coupling loss and surface roughness of the copper-coated waveguide. The forward transmission of a bare-PS waveguide is also measured as shown in Fig. 48(c). In this setup, fingers (very lossy) intentionally touch the waveguide to measure the performance degradation. As summarized in Fig. 48(d), when fingers touch bare-PS waveguide, insertion loss of the section increases more than 20dB, while in the copper-coated case, the added insertion losses due to contact with the finger is negligible.

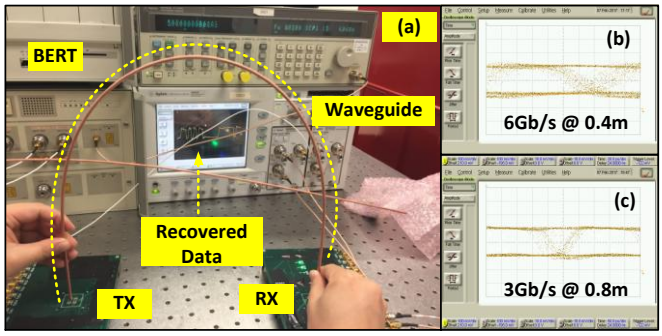

Fig. 49. (a) Data transfer measurement setup. (b) Measured 6Gb/s eye-diagram over 0.4m waveguide. (c) Measured 3Gb/s eye-diagram over 0.8m waveguide.

Employing the 60GHz CMOS transceiver reported in [44] and coupling it to the copper-coated waveguide, a high-speed wireline communication system is demonstrated as shown in Fig. 49(a). The waveguide is held by hands and placed in a U-shape to demonstrate the field confinement and flexibility. The bit-error-rate-tester (BERT) generates high-speed random data and feeds it to the CMOS transmitter (TX). Then, the TX modulates 60GHz carrier with an amplitude-shift keying modulation and transfers EM energy through the waveguide. The CMOS receiver at the opposing end captures and de-modulates the transmitted signal and provides the recovered data to scope to display an eye-diagram of the captured sequences. Fig. 49(b) and (c) show the eye-diagrams for operation at 6Gb/s over 0.4m and 3Gb/s over 0.4m which confirms that the proposed copper-coated waveguide is capable of high-speed data communication.

5.4 CONCLUSION

A low-cost metal-coated flexible dielectric waveguide is proposed for high-speed wireline communication systems. Analytical study reveals that several microns of metal coating is sufficient to confine an EM field at millimeter-wavelengths while still allowing the waveguide to remain flexible enough so it can conform to its environment. The measurements and analysis of this waveguide show a discrepancy of less than 4dB, which is attributed to coupling losses and surface roughness not captured in the analytical model. We have empirically demonstrated that the proposed waveguide supports high-speed data transmission by combining it with an existing 60GHz transceiver module. Finally, the results obtained imply that higher carrier frequencies and smaller waveguide dimensions would provide further advantages.

Chapter 6

Impulse Response Analysis of Waveguides for High-Speed Communication

6.1 INTRODUCTION

A demand in increasing bandwidth has driven researchers to explore waveguides as high-speed data communication channels [67-70]. A common philosophy relies on ideas of large available bandwidth and low-loss characteristic in millimeter-wave/terahertz domains through waveguide channels.

Waveguides are known to be dispersive or band-limited because of non-linear propagation constant (β), and bandwidth capacity is traditionally estimated through a group delay (τ_g) variation. Assuming a narrow input data bandwidth (BW) is applied through a waveguide, a group delay and pulse broadening coefficient (τ_p) at a target carrier frequency (ω_0) is expressed as,

$$\tau_g = \frac{d\beta}{d\omega}\Big|_{\omega=\omega_0} \quad \text{(s/m)} \tag{1}$$

$$\tau_p = BW \times \frac{d\tau_g}{d\omega}\Big|_{\omega=\omega_0} = BW \times \frac{d^2\beta}{d^2\omega}\Big|_{\omega=\omega_0} \quad \text{(s/m)} \tag{2}$$

,where ω is a an angular frequency. As indicated in (2), the larger the bandwidth, the higher pulse broadening will be added to an originally transmitted pulse over distance. From an input baseband pulse point of view in time domain, a first-order derivative of β simply delays, second-order derivative delays and broadens; from third-order and beyond, it delays, broadens, and distorts all together. As a communication bandwidth enters regimes much greater than multi-tens of gigabits per second (>10Gb/s), a group delay variation method not only violates a narrow

bandwidth assumption, but it also completely neglects a distortion and ISI effect.

In this paper, an impulse response analysis is introduced to analyze baseband data behavior through waveguides under a coherent based communication system. According to Maxwell's equations, an input to output relationship of waveguide is categorized as a linear time-invariant (LTI) system. In other words, if an impulse response of waveguide is known, an output can be calculated for any given input data pattern. Accordingly, the first step to design a high-speed communication system is typically determine the impulse response of a given channel [71-73]. Although there have been attempts to characterize impulse response of waveguides, they require either direct measurements or again narrow bandwidth assumption to linearize a propagation constant [74-77]. Instead, borrowing concepts from communication theory, a frequency domain convolution and multiplication method is applied by taking both negative and positive frequency regions into considerations. The proposed analysis achieves an exact expression of baseband equivalent impulse response in frequency domain and leads to a true impulse response in time domain by way of an inverse Fourier transform. As long as frequency dependent attenuation (σ) and propagation constant (β) is provided, the analysis can be applied to any shape (rectangular, circular, elliptical) or any type (dielectric, metallic) of waveguide in an arbitrary frequency range. A dielectric-filled metallic circular waveguide and air-filled metallic rectangular waveguide is presented as examples since they offer σ and β in closed-form equations.

6.2 BASEBAND EQUIVALENT IMPULSE RESPONSE

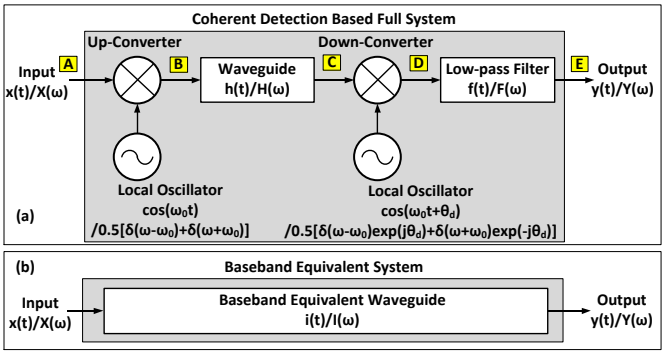

Fig. 50. (a) Coherent based full transmitter and receiver system includes up-converter, down-converter, local oscillators, and low-pass filter. Two local oscillators are assumed to be phase and frequency synchronized in the transmitter and receiver side. (b) The full system is replaced by a baseband equivalent waveguide channel as an impulse response.

A coherent detection based full system diagram is illustrated in Fig. 50(a). By splitting a signal vector space, namely in-phase and quadrature-phase, a coherent architecture can achieve an enhanced bandwidth efficiency with modulation schemes such as quadrature-phase shift keying (QPSK) and 16-quadrature amplitude shift keying (16QAM). The system diagram in Fig. 50 contains only an in-phase path, but a quadrature path could always be applied when necessary.

In the diagram, time domain and frequency domain symbols are written with lower case and upper case letters respectively. An input data $x(t)$ modulates a carrier (ω_0) via an up-converter and travels through a waveguide $h(t)$. A down-converter then de-modulates an incoming signal with a receiver side local oscillator (LO). A fixed amount of extra LO phase, which is directly calculated from a waveguide channel delay at a carrier frequency, is added to a receiver LO to synchronize a phase between transmitter and receiver. A method of synchronization is beyond the discussion of this paper, and they are assumed to be synchronized (a consequence will be explained if not synchronized). In the last stage, a low-pass filter (LPF)

filters out the residue of $2\omega_0$ component generated from the down-conversion process. An ultimate goal is to capture the non-linear property of waveguide propagation constant and translate into a baseband equivalent impulse response $i(t)$ or $I(\omega)$ model as in Fig. 50(b). With an impulse response defined, an output becomes,

$$Y(\omega) = X(\omega)I(\omega) \tag{3}$$

$$y(t) = x(t) * i(t) \tag{4}$$

, where $*$ operator indicates a convolution.

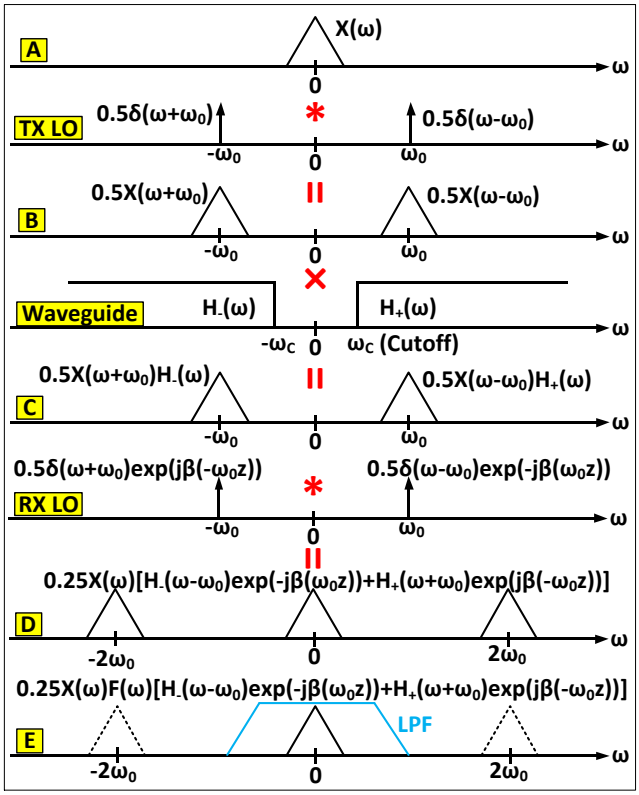

Fig. 51. The process of frequency domain calculation is shown in alphabetical order that was listed in Fig. 50(a). Note from the property of LTI system that time domain multiplication becomes frequency domain convolution, and time domain convolution becomes frequency domain multiplication.

Based on the system block diagram, the process of frequency domain computation is built in Fig. 51. After solving boundary conditions of a given waveguide, a frequency response (or commonly referred as a time-harmonic expression) of electromagnetic field propagating in z-direction can be readily characterized as,

$$H_+(\omega) = \begin{cases} e^{-\alpha(\omega)z}e^{-j\beta(\omega)z} & (\omega > 0) \\ 0 & (\omega < 0) \end{cases}$$

$$H_-(\omega) = \begin{cases} 0 & (\omega > 0) \\ e^{-\alpha(\omega)z}e^{+j\beta(\omega)z} & (\omega < 0) \end{cases}$$

$$H(\omega) = H_+(\omega) + H_-(\omega) \qquad (5)$$

,where z is the length of wave travelled [22]. $H(\omega)$ splits into (+) and (-) component to handle a conjugate symmetric property of frequency response. An attenuation constant α and propagation constant β is frequency-dependent, geometry-dependent, waveguide-type-dependent, and mode-dependent. To demonstrate this idea, an input spectrum $X(\omega)$ and waveguide frequency response $H(\omega)$ are configured arbitrarily in Fig. 51. A key message in this figure is to include and calculate a negative frequency spectral portion throughout the process. To summarize the process at each node,

$$\text{A: } X(\omega) \qquad (6)$$

$$\text{TX LO: } \frac{1}{2}[\delta(\omega + \omega_0) + \delta(\omega - \omega_0)] \qquad (7)$$

$$\text{B: } \frac{1}{2}[X(\omega + \omega_0) + X(\omega - \omega_0)] \qquad (8)$$

$$\text{C: } \frac{1}{2}[X(\omega + \omega_0)H_-(\omega) + X(\omega - \omega_0)H_+(\omega)] \qquad (9)$$

$$\text{RX LO: } \frac{1}{2}\left[\delta(\omega + \omega_0)e^{+j\beta(\omega)z} + \delta(\omega - \omega_0)e^{-j\beta(\omega)z}\right] = \frac{1}{2}\left[\delta(\omega + \omega_0)e^{+j\beta(-\omega_0)z} + \right.$$

$$\delta(\omega-\omega_0)e^{-j\beta(\omega_0)z}] \quad (10)$$

D: $$\left\{\frac{1}{2}[X(\omega+\omega_0)H_-(\omega)+X(\omega-\omega_0)H_+(\omega)]\right\} * \left\{\frac{1}{2}\left[\delta(\omega+\omega_0)e^{+j\beta(-\omega_0)z}+\delta(\omega-\omega_0)e^{-j\beta(\omega_0)z}\right]\right\} \quad (11)$$

In (10), only a fixed phase portion is extracted from $H(\omega)$ and accumulated to a receiver LO for phase synchronization. Next, (11) can be further expanded to,

$$\frac{1}{4}X(\omega)\left[H_-(\omega-\omega_0)e^{-j\beta(\omega_0)z}+H_+(\omega+\omega_0)e^{+j\beta(-\omega_0)z}\right]$$

$$+\frac{1}{4}X(\omega+2\omega_0)H_-(\omega+\omega_0)e^{+j\beta(-\omega_0)z}+\frac{1}{4}X(\omega-2\omega_0)H_+(\omega-\omega_0)e^{-j\beta(\omega_0)z} \quad (12)$$

The first term in (12) discloses that a baseband spectrum is multiplied by a sum of two frequency shifted waveguide channel response. For the latter two terms, it is clear that they are $2\omega_0$ components, and they make the system in (12) linear time-variant (LTV). Thus, from a mathematical standpoint, an LPF must fully reject the $2\omega_0$ residue in order for a baseband equivalent frequency response to remain as an LTI system. Practically speaking, the above statement is a reasonable assumption, for instance, if a carrier frequency is 100 GHz, a residue will appear at 200 GHz, which can be easily filtered out even with a one-pole LPF. Therefore, an output spectrum can be written as,

E: $$Y(\omega)=\frac{1}{4}X(\omega)F(\omega)\left[H_-(\omega-\omega_0)e^{-j\beta(\omega_0)z}+H_+(\omega+\omega_0)e^{+j\beta(-\omega_0)z}\right] \quad (13)$$

A choice of LPF could greatly affect a baseband equivalent impulse response. In order not to be dominated by a filter frequency response, only a simple one-pole R and C filter with tens of pico-seconds (ps) time constant will be used. Following the definition of impulse response, $x(t)=\delta(t)$, which is $X(\omega)=1$, can be inserted to (13), and finally a baseband equivalent impulse

response in frequency domain is derived as,

$$I(\omega) = Y(\omega)|_{X(\omega)=1} = \frac{1}{4}F(\omega)\left[H_{-}(\omega-\omega_0)e^{-j\beta(\omega_0)z} + H_{+}(\omega+\omega_0)e^{+j\beta(-\omega_0)z}\right] \quad (14)$$

There are two important things to highlight. First, a baseband equivalent impulse response in frequency domain consists of positively shifted and negatively shifted $H(\omega)$ around a carrier frequency. Second, an impulse response depends on a carrier frequency. For example, with a given geometry, dimension, and length of waveguide, as a carrier frequency increases, a modulated wave propagates closer to a transverse electromagnetic (TEM)-like mode, expecting less dispersion and distortion. So far, a mathematical framework has been developed. In-depth analysis with examples will deliver intuition in the following chapters.

6.3 Dielectric-Filled Metallic Circular Waveguide

Propagation properties of metallic circular waveguide are well-defined with closed-form equations [22]. Throughout the study, a particular diameter, waveguide length, and frequency range will be used instead of wavelength normalized parameters because of a relation to a pulse behavior in time domain. In addition, dimension and frequency are chosen in such a way that the discussion fits well with a data rate of 10Gb/s or higher using a millimeter-wave/terahertz carrier. A specific dimension and resulting characteristics for a given waveguide are summarized in Fig. 52. For a dielectric material, common inexpensive polymers (Teflon, polystyrene, polyethylene, etc) exhibit dielectric constant of 2.1~2.6 range, and they show excellent loss tangent of 0.0005~0.001 in millimeter wavelength range [18].

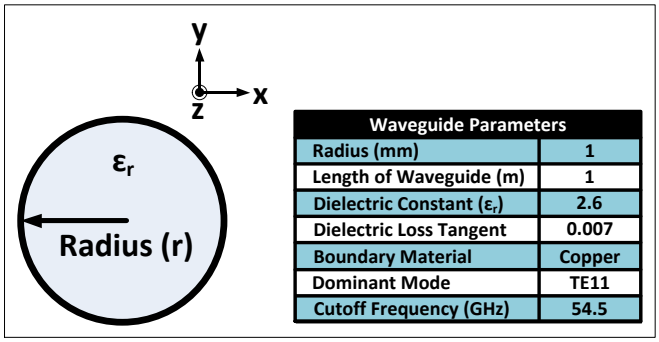

Fig. 52. Cross-section of dielectric-filled metallic circular waveguide is shown with its propagation parameters. Wave propagates along z-direction.

6.3.1 TE11 mode attenuation and propagation constant

Instead of repeating the procedure of solving Maxwell's equations, readily available attenuation and propagation constants are brought from [22],

$$\text{Wavenumber: } k = \omega\sqrt{\mu\epsilon} \tag{15}$$

$$\text{Cutoff Wavenumber: } k_{c11} = \frac{p_{11}^{'}}{r} \tag{16}$$

$$\text{Propagation Constant: } \beta_{11} = \sqrt{k^2 - k_{c11}^2} \tag{17}$$

$$\text{Conductive Atten. Constant: } \sigma_c = \frac{R_S}{rk\eta\beta}\left(k_{c11}^2 + \frac{k^2}{p_{11}^{'2}-1}\right) \tag{18}$$

$$\text{Dielectric Atten. Constant: } \sigma_d = \frac{k^2 tan\delta}{2\beta} \tag{19}$$

$$\text{Cutoff Frequency: } \omega_{c11} = \frac{k_{c11}}{\sqrt{\mu\epsilon}} \tag{20}$$

, where μ is permeability, $p_{11}^{'}$ is constant (1.841) where transverse electric (TE)11 mode satisfies boundary condition, r is radius, R_S is surface resistance of copper, η is wave impedance, $tan\delta$ is loss tangent of dielectric material. An attenuation constant is a sum of conductive and dielectric attenuation constant. Using the parameters in Fig. 52 and a waveguide channel response in (5), a

phase and magnitude response of a dielectric-filled metallic circular waveguide is plotted in Fig. 53(a) and (b). Notice how the phase is asymmetric and magnitude is symmetric around DC. In a general complex number domain, when a system or signal is a real number, the Fourier transform of it becomes conjugate symmetric. A waveguide in time domain is also a real number system, which is exactly how the frequency domain phase and magnitude response appears in Fig. 53. Below cutoff frequency, a propagation constant becomes imaginary and a wave decays exponentially without propagation. Above cutoff frequency, a circular waveguide acts as a low-pass system caused by conductive and dielectric loss, but in a pass-band region.

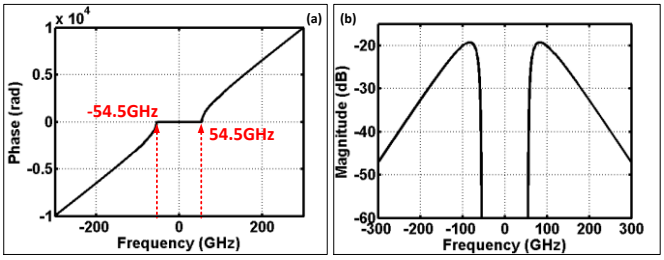

Fig. 53. (a) Circular waveguide's propagation constant. (b) Circular waveguide's magnitude response. Notice how phase is asymmetric and magnitude is symmetric around DC.

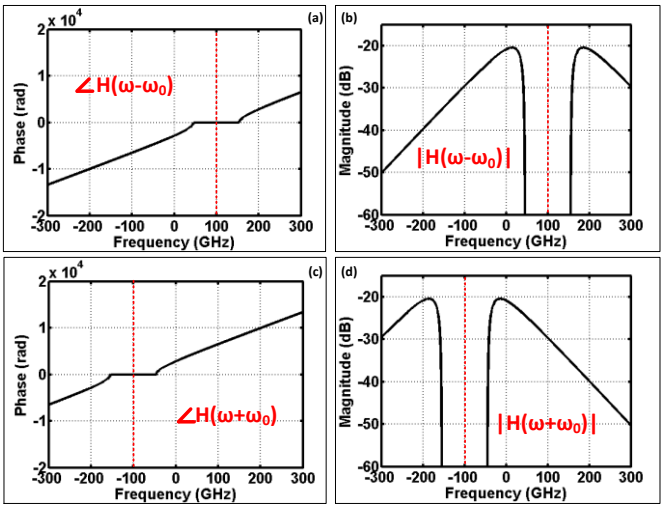

Fig. 54. Propagation constant and magnitude response is shifted around carrier frequency, 100 GHz. (a) Positively shifted propagation constant. (b) Positively shifted magnitude response. (c) Negatively shifted propagation constant. (d) Negatively shifted magnitude response.

6.3.2 Baseband equivalent impulse response in frequency domain

As a reminder from (14), an impulse response in frequency domain is a combination of two frequency response of waveguide; one with positively shifted, the other with negatively shifted around a carrier frequency. After applying the frequency response in (5) to (14), each of shifted frequency responses over 1-meter distance and resulting baseband equivalent impulse response can be derived as,

$$\frac{1}{4}H_{-}(\omega-\omega_0)e^{-j\beta(\omega_0)} = \frac{1}{4}e^{-\alpha(\omega-\omega_0)}e^{+j\beta(\omega-\omega_0)}e^{-j\beta(\omega_0)} \tag{21}$$

$$\frac{1}{4}H_{+}(\omega+\omega_0)e^{+j\beta(-\omega_0)} = \frac{1}{4}e^{-\alpha(\omega+\omega_0)}e^{-j\beta(\omega+\omega_0)}e^{+j\beta(-\omega_0)} \tag{22}$$

$$I(\omega) = \frac{1}{4}F(\omega)\left[e^{-\alpha(\omega+\omega_0)}e^{-j\beta(\omega+\omega_0)}e^{+j\beta(-\omega_0)} + e^{-\alpha(\omega-\omega_0)}e^{+j\beta(\omega-\omega_0)}e^{-j\beta(\omega_0)}\right] \tag{23}$$

Strictly speaking, (23) is only defined over $(-\omega_0+\omega_{c11} < \omega < \omega_0-\omega_{c11})$, which is a main bandwidth of interest. In the following section, the impact of carrier frequency will be studied, but for a concept demonstration at the moment, the carrier frequency is deployed at 100 GHz. As shown in Fig. 54, a down-conversion by a carrier frequency shifts the frequency response of waveguide around (+) and (-) 100 GHz while preserving its original response. Then from (23), a phase and magnitude response of baseband equivalent impulse response in frequency domain is constructed in Fig. 55. An interesting activity of magnitude response can be found in Fig. 55(b): frequency notches.

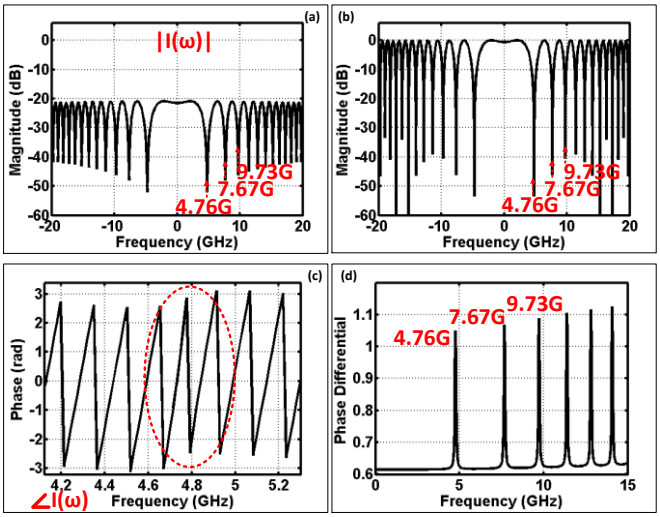

Fig. 55. (a) Magnitude response of baseband equivalent impulse response. Notice frequency notches. (b) Magnitude response of phase-only contribution. Notch frequencies exactly match. (c) Modulus of 2π in (a) is plotted. Phase discontinuity is observed around notch frequency. (d) Slope of (a) is plotted to clearly see the phase discontinuity at each notch frequency. The peaks match to the magnitude response.

Making a conclusion statement first, a major reason behind notches comes from a non-linear propagation constant of waveguide. To observe an effect of propagation constant only and prove above statement, an amplitude contribution of (23) is completely discarded as if a waveguide is lossless, and the expression is re-written as,

$$I(\omega) = e^{-j\beta(\omega+\omega_0)}e^{+j\beta(-\omega_0)} + e^{+j\beta(\omega-\omega_0)}e^{-j\beta(\omega_0)} \tag{24}$$

Then, the magnitude response of (24) is plotted in Fig. 55(b) exhibiting identical notch frequencies as in Fig. 55(a). Be aware that the final phase response of baseband equivalent impulse response is not a simple addition of two phase because the two exponential components $e^{-j\beta(\omega-\omega_0)}e^{j\beta(\omega_0)}$ and $e^{-j\beta(\omega+\omega_0)}e^{-j\beta(\omega_0)}$ are not multiplied in frequency domain. After

retrieving a phase of (23), a modulus of 2π is taken and zoomed in at the first notch frequency as in Fig. 55(c). Around the dotted circled area, the rate of phase increment per unit frequency range decreases around 4.7 GHz and increases back to a normal pace after passing the notch frequency. This behavior can be clearly seen by taking a difference of phase with respect to the difference in frequency as in Fig. 55(d). The apparent discontinuities are observed in each notch frequency in the magnitude response.

However, it may not seem obvious how the notch would occur, because all frequency components above cutoff frequency (54.5 GHz) propagate through a waveguide, and they do not work in a way of destructive interference. Focusing attention at the 4.76 GHz notch frequency, the baseband 4.76 GHz component is a result of combining 104.76 GHz (f_2) and 95.34 GHz (f_1) signal components after down-conversion as shown in Fig. 56(a). Now, two continuous waves pass through a waveguide and experience attenuation and phase delay at each frequency component f_1 and f_2. At the input of down-converter, the combined signal from f_1 and f_2 is compared with a receiver LO signal in Fig. 56(b). Comparing the phase relationship between two, they are nearly 90 degrees out of phase, which means a conversion gain for 4.76 GHz is very low, which also means majority of in-phase signal is leaked into a quadrature side. After down-conversion, the Fourier transform is taken and the power level of 4.76 GHz component is plotted in Fig. 56(c). In Fig. 56(d) and (e), a same process is performed using 101 GHz and 99 GHz components to check the power level of 1 GHz baseband component. This time, the two signals are almost in-phase, and the power level of 1 GHz component is at least 20 dB higher than 4.76 GHz component.

As stated in (3), after having established the impulse response of a waveguide, an output data spectrum can be calculated instantly by multiplying input spectrum and impulse response in

frequency domain as shown in Fig. 57. For instance, imagine a 100 ps of single pulse travels down to a waveguide with a carrier frequency of 100 GHz. In frequency domain, it means a sync function multiplies with an impulse response studied in Fig. 55. Notice the output spectrum contains notches at 4.76 GHz and 7.67 GHz below 10 GHz (data null). For applications in high-speed data communication through PCB or copper cable, discontinuities such as connectors or via usually create notches in frequency domain by a destructive interference mechanism. However for waveguides under coherent architecture, a non-linear propagation constant, which is a complicated function of waveguide geometry, length, dielectric material, and carrier frequency, generates notches in frequency domain after down-conversion. Fortunately, the proposed analysis could precisely analyze a notch behavior without needing any estimating method.

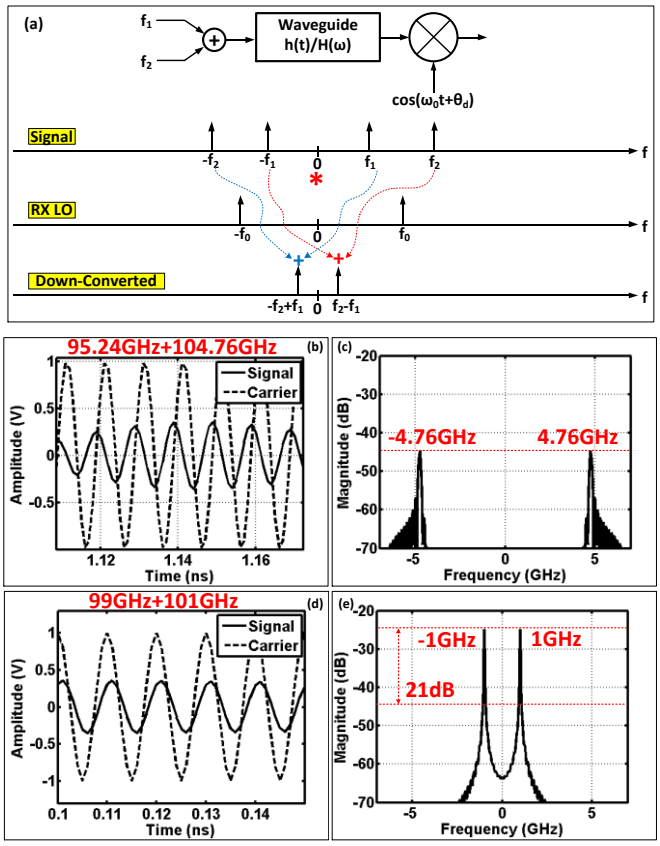

Fig. 56. (a) Two time domain frequency components are passed through down-converted by receiver LO. The diagram shows how baseband component forms after down-conversion. (b) 95.24 GHz and 104.76 GHz are generated, added, propagated through channel, and compared with a receiver LO at the input of down-converter. (c) After down-conversion, Fourier transform is taken to show the power level at 4.76 GHz. (d) Same procedure is performed using 101 GHz and 99 GHz components. (e) Power level is significantly higher (>20 dB) than 4.76 GHz case.

6.3.3 Time domain impulse response and simulation

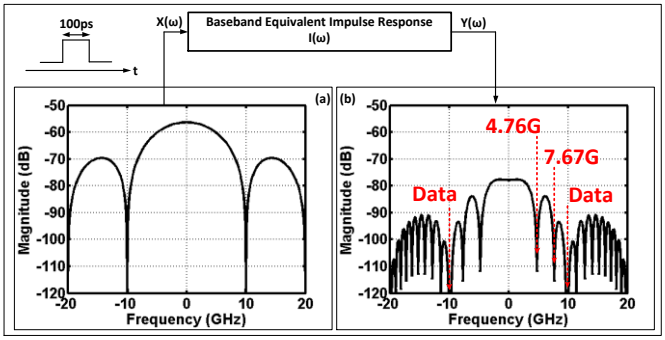

Fig. 57. (a) A 100 ps baseband pulse is generated at the input of waveguide. (b) After taking Fourier transform, input spectrum is fed into the baseband equivalent impulse response of waveguide, and the output spectrum of pulse is generated instantly by multiplying two spectrums. Notice that notches heavily affects the output spectrum.

In Fig. 58(a), an impulse response of waveguide in time domain is first calculated by taking an inverse Fourier transform of (23) in MATLAB software. Interestingly, a finite delay of modulated wave through a waveguide is also reflected in the baseband impulse response. As suggested in (4), an impulse response in time domain is now convoluted with an input pulse to generate an output pulse. Taking a closer look at Fig. 58(c), when 100 GHz of carrier frequency is used, a 1-meter length of dielectric-filled metallic circular waveguide contributes roughly 160 ps of pulse broadening as well as post-cursor and pre-cursor residue. On the other hand, a group

delay variation method in (1) and (2) estimates 82 ps of pulse broadening, which is half of what an impulse response method has predicted. To illustrate a group delay variation method briefly, a dispersion coefficient is calculated based on 10 GHz baseband equivalent bandwidth in Fig. 58(d). The graph shows a dispersion decreases as carrier frequency increases. In Fig. 58(e), a dispersion from an impulse response is compared with a group delay method with a fixed carrier frequency of 100 GHz for both cases. As expected, a group delay method increases a dispersion coefficient linearly. To be fair, for the case of impulse response, a dispersion is measured while an attenuation constant of waveguide is kept at zero, because a group delay variation method does not consider a dispersion effect from an amplitude response variation at all. At a bandwidth of 10 GHz, the difference between the two increases by 90 ps, which is close to 100% of its original bandwidth. The above analysis verifies how a group delay method is inappropriate for a wideband data communication.

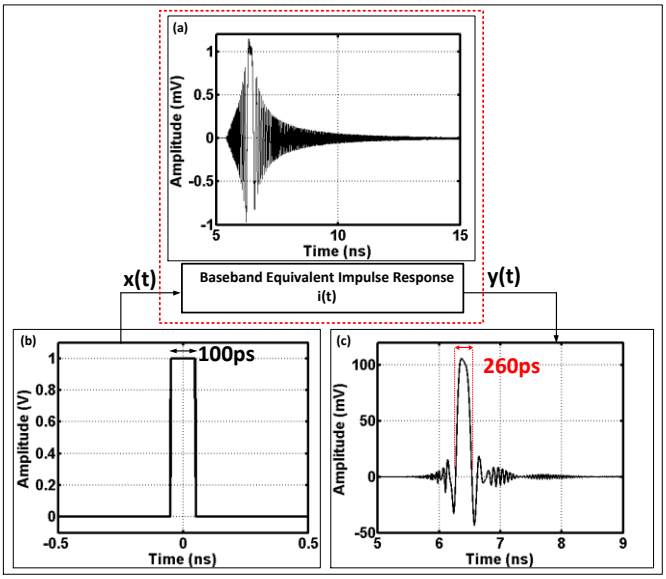

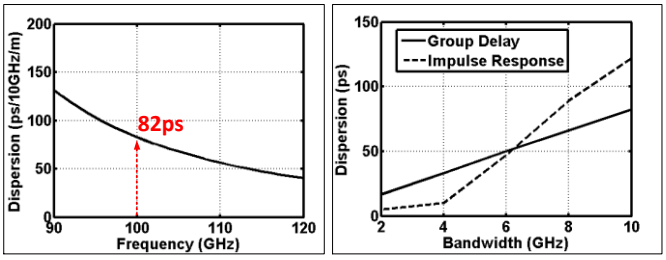

Fig. 58. (a) Time domain impulse response is calculated in MATLAB. (b) A 100 ps baseband pulse is generated. (c) Two are convoluted in time domain. A resulting pulse width at the output is increased to 260 ps. (d) Dispersion coefficient with 10 GHz baseband equivalent bandwidth using group delay variation method. (e) Dispersion comparison with group delay and impulse response method.

In order to prove the validity of the frequency domain impulse response expression in (23), a time domain simulation is conducted by stepping through each stage as in Fig. 59(a). An up-converter multiplies input pulse and carrier signal at node B, and the modulated signal undergoes dispersion and distortion at node C. A down-converter translates to a baseband with $2\omega_0$ residue at node D, and an LPF filters out the $2\omega_0$ component at node E. As a side note, one can decide to down-convert at node C by way of an envelope detector but with a cost of 400 ps pulse broadening penalty. Comparing Fig. 58(c) and Fig. 59(e), the two baseband output signals are almost identical except the fact that there is a slight residue of $2\omega_0$ component left in Fig. 59(e).

Another crucial advantage of the baseband equivalent impulse response is the ability to simulate a random bit sequence as an input and generate an eye-diagram for a given data rate as in Fig. 60. A single pulse informs on a degree of dispersion or distortion, but a measure of inter-symbol interference (ISI) requires a random bit pattern of input. After all, a waveguide transfers lots of digital data consisting of ones and zeros, and by the definition of information conveying signal, they need to be a random combination. Once an impulse response is created, a sequence

of randomly combined ones and zeros convolve with an impulse response and produce an eye-diagram. For the given waveguide parameters in Fig. 52 and carrier frequency of 100 GHz, it is obvious that 10Gb/s of data stream is not suitable without any equalization as shown in Fig. 60(d).

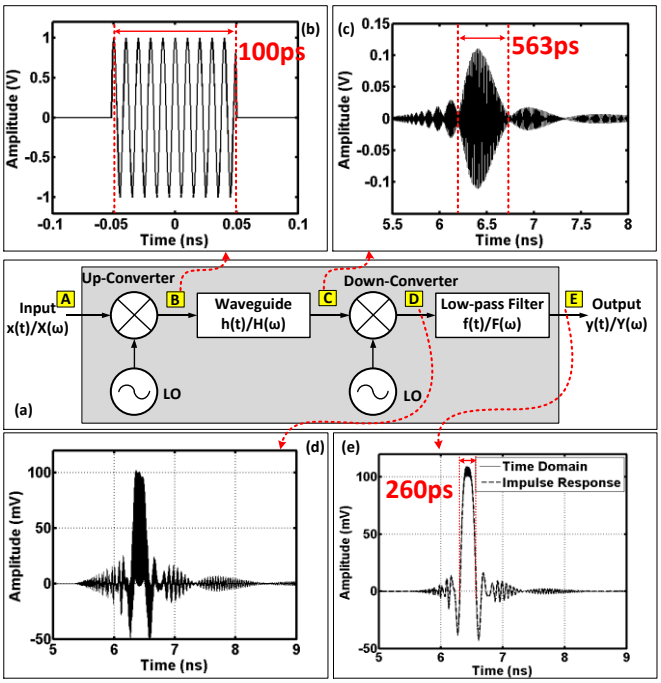

Fig. 59. (a) Block diagram. (b) Modulated pulse with 100 GHz carrier frequency. (c) Heavily dispersed modulated pulse after going through the waveguide. (d) Down-converted baseband pulse with $2\omega_0$ residue. (e) Baseband pulse after LPF.

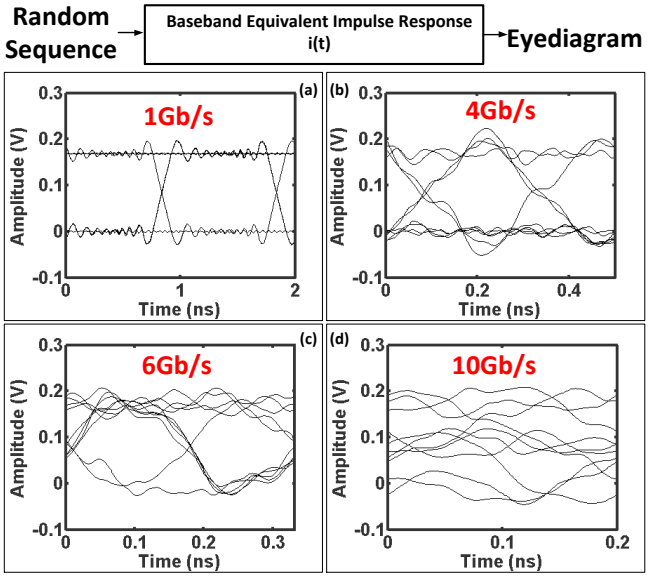

Fig. 60. (a) 1Gb/s eye-diagram. (b) 4Gb/s eye-diagram. (c) 6Gb/s eye-diagram. (d) 10Gb/s eye-diagram.

6.3.4 Effect of phase mismatch

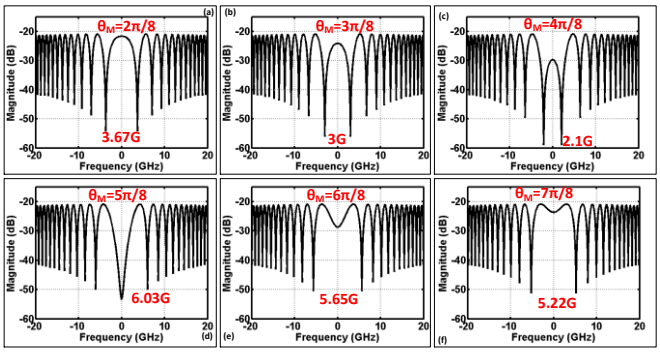

Fig. 61. (a) Impulse response when $\theta_M = \frac{2\pi}{8}$. (b) Impulse response when $\theta_M = \frac{3\pi}{8}$. (c) Impulse response when $\theta_M = \frac{4\pi}{8}$. (d) Impulse response when $\theta_M = \frac{5\pi}{8}$. (e) Impulse response when $\theta_M = \frac{6\pi}{8}$. (f) Impulse response when $\theta_M = \frac{7\pi}{8}$.

A non-linear propagation constant causes a potential catastrophe for a high-speed communication system if a phase between transmitter LO and receiver LO is not synchronized. If a propagation constant is a linear function of frequency within a bandwidth of interest, a phase

mismatch would reduce a conversion gain but not affect the bandwidth of baseband data. A simple expression can be written based on this assumption,

$$y(t) = x(t)\cos(\omega_0 t) \times \cos(\omega_0 t + \theta_M) = \frac{x(t)}{2}[\cos(\theta_M) + \cos(2\omega_0 t + \theta_M)] \quad (25)$$

, where θ_M is a phase mismatch factor in radian. After filtering out $2\omega_0$ component, a constant value of $\cos(\theta_M)$ is multiplied to a baseband signal as an indication of reduced conversion gain. However, the situation changes when a propagation constant turns into non-linear. Going back to (23), a new expression with a phase mismatch factor included is written as,

$$I(\omega) = \frac{1}{4}F(\omega)\left[e^{-\alpha(\omega+\omega_0)}e^{-j\beta(\omega+\omega_0)}e^{+j(\beta(-\omega_0)+\theta_M)} + e^{-\alpha(\omega-\omega_0)}e^{+j\beta(\omega-\omega_0)}e^{-j(\beta(\omega_0)+\theta_M)}\right] \quad (26)$$

It is difficult to grasp what may occur from (26), but an intuitive clue can be deduced from Fig. 56. Earlier, when a phase is synchronized between transmitter and receiver, a notch happens to appear at 4.76 GHz because a receiver LO (100 GHz) and 104.76 GHz + 95.24 GHz signal component is 90 degrees out of phase. It means 104.76 GHz + 95.24 GHz signal is no longer 90 degrees out of phase if a phase of receiver LO moves because of a mismatch. Consequently, as an LO phase shifts, notch frequencies also move, and this behavior repeats every π cycle of θ_M. In Fig. 61, the above statement is summarized with a magnitude response of impulse response by solving (26). As a phase mismatch increases up to $\theta_M = \frac{4\pi}{8}$, the first notch frequency moves towards DC, reducing an effective baseband equivalent bandwidth. At the same time, a magnitude of baseband portion also decreases because of the loss of conversion gain, which is

another undesirable side-effect. Passing $\theta_M = \frac{4\pi}{8}$, a notch frequency is pushed out to 6.03GHz, but now, there is also notch at DC that works as a high-pass filter for a baseband signal. Moving forward, a notch frequency again moves towards DC, but in-band ripple is reduced within 10 dB. An interesting note here is that, with a proper amount of phase mismatch such as in $\theta_M = \frac{7\pi}{8}$, a baseband signal may take advantage of a free equalization effect with a frequency peaking behavior. A non-linear propagation constant impacts not only conversion gain but also an equivalent baseband bandwidth.

6.3.5 Effect of carrier frequency

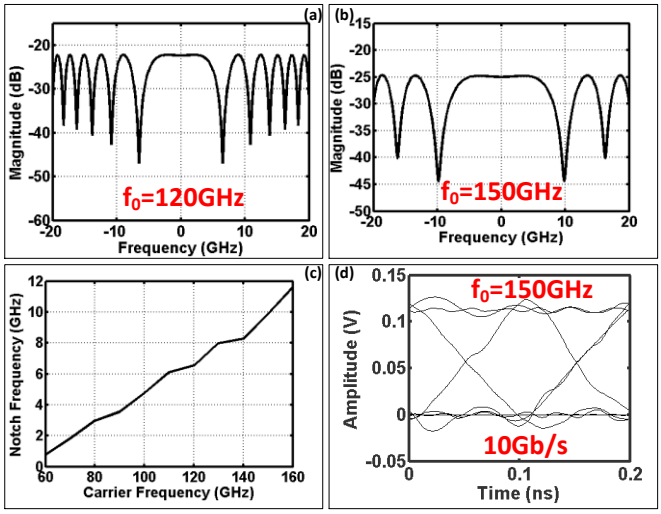

Fig. 62. (a) Frequency response with 120GHz carrier frequency. (b) Frequency response with 150GHz carrier frequency. (c) Measure of first notch frequency vs. carrier frequency. (d) 10Gb/s eye-diagram with 150GHz carrier frequency.

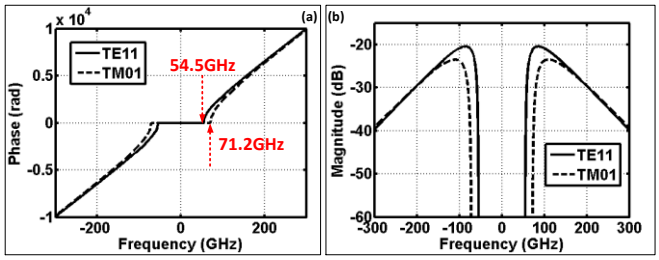

Fig. 63. (a) Phase response of TE11 and TM01 mode. (b) Magnitude response of TE11 and TM01 mode.

Increasing carrier frequency for a given waveguide improves signal integrity because a wave propagates with TEM-like mode. However, increasing carrier frequency also increases a dielectric loss and the chance of inducing higher order modes. Based on (23), an impulse response in frequency domain at 120 GHz and 150 GHz is plotted in Fig. 62(a) and (b). With 150 GHz carrier frequency, a notch frequency is pushed out to 10 GHz from 4.76 GHz compared to the 100 GHz case, but loss increases about 3 dB at the same time. In other words, increasing carrier frequency trades a baseband equivalent bandwidth with a signal-to-noise ratio. An apparent improvement of notch frequency can be seen as a carrier frequency increases in Fig. 62(c). For a random sequence testing, an eye opening for 10Gb/s data stream is clearly visible with 150 GHz carrier frequency, whereas an eye-diagram was closed when a carrier frequency is 100 GHz. The impulse response analysis allows us to figure out an exact system requirement once target performance and geometry conditions are known without building actual hardware.

6.3.6 Impact of multimode propagation

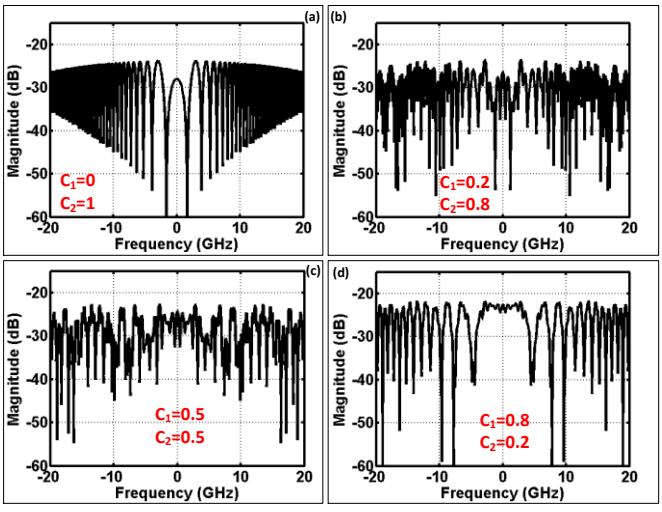

Fig. 64. Carrier frequency is 100 GHz. (a) Frequency response with C_1=0 and C_2=1. (b) Frequency response with C_1=0.2 and C_2=0.8. (c) Frequency response with C_1=0.5 and C_2=0.5. (d) Frequency response with C_1=0.8 and C_2=0.2.

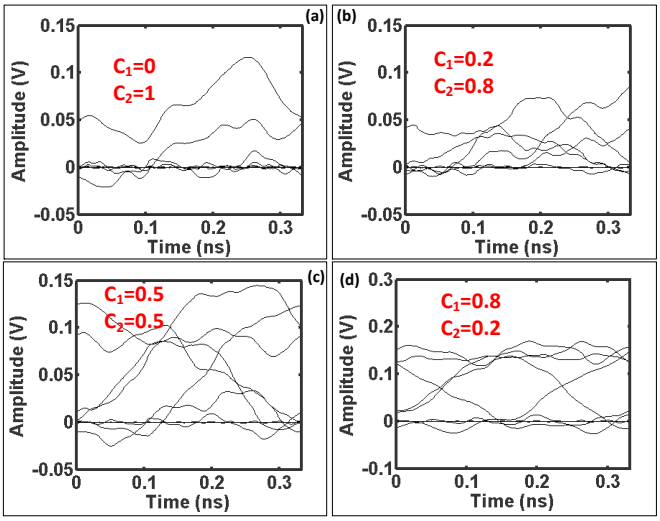

Fig. 65. Carrier frequency is 100 GHz and the data rate is 6Gb/s. (a) Eye-diagram with C_1=0 and C_2=1. (b) Eye-diagram with C_1=0.2 and C_2=0.8. (c) Eye-diagram with C_1=0.5 and C_2=0.5. (d) Eye-diagram with C_1=0.8 and C_2=0.2.

A given waveguide in Fig. 52 supports multiple mode of propagation at 100 GHz, although it may not necessarily excite all possible modes. Even if only one dominant mode is excited at the input, while a wave travels down to a waveguide, a mode conversion may occur because of non-uniform medium or bending curvature. In another case, depending on how a waveguide is excited, a multimode may or may not propagate [78]. It is not the interest of this paper to find out how a multi-mode propagation may occur or how to prevent such an event, but rather figure out how the multimode influences a baseband equivalent impulse response. For brevity, the topic is confined to a 2-mode (TE11 and TM01) propagation. To generate a transverse magnetic (TM)-01 mode, relations from (16) to (20) are re-utilized except $p_{11}^{'}$ is replaced by p_{01}, which is 2.405. As shown in Fig. 63, the 2nd mode begins at 71.2 GHz.

According to a field orthogonality theory [79], a transfer function of waveguide and its impulse response can be written as a linear superposition of two transfer functions,

$$H(\omega) = C_1 H_1(\omega) + C_2 H_2(\omega) \tag{27}$$

$$I(\omega) = C_1 I_1(\omega) + C_2 I_2(\omega) \tag{28}$$

, where $H_1(\omega)$ and $I_1(\omega)$ is a dominant mode, $H_2(\omega)$ and $I_2(\omega)$ is a second mode, and C_1 and C_2 is a constant coefficient for each mode. An expression for original waveguide frequency response and its impulse response of $H_2(\omega)$ and $I_2(\omega)$ is configured based on (5) and (23) with α and β is updated according to p_{01}. Caution is required however. In earlier development, a fixed amount of phase is added to a receiver LO to synchronize a phase between transmitter and receiver. The fixed amount of phase was calculated using a dominant mode propagation constant, and the same fixed phase will be employed for both dominant mode and the second mode, because a dominant mode is always the preferred mode. That is,

$$I_2(\omega) = \frac{1}{4} F(\omega)\left[e^{-\alpha_2(\omega+\omega_0)} e^{-j\beta_2(\omega+\omega_0)} e^{+j\beta_1(-\omega_0)} + e^{-\alpha_2(\omega-\omega_0)} e^{+j\beta_2(\omega-\omega_0)} e^{-j\beta_1(\omega_0)}\right] \tag{29}$$

, where subscript 1 and 2 means dominant mode and second mode. When $C_2 = 0$, only a dominant mode propagates, and when $C_1 = 0$, only a second mode propagates. When both are non-zero, both mode would propagate, but again, calculating each coefficient itself under certain circumstance is not the interest. It is assumed that the coefficients are given (for instance, $C_1 = 0.8$ and $C_2 = 0.2$), and they are inserted into (28) to see how impulse response responds. With a given waveguide geometry and carrier frequency, it is obvious to anticipate a multimode propagation increases a multi-path effect and corrupts a signal integrity. A few combinations of coefficients are chosen and corresponding impulse responses in frequency domain are plotted in

Fig. 64. As described in Fig. 64(a), when only a second mode propagates, the first notch in impulse response shows up at 1.7 GHz compared to 4.76 GHz in a dominant mode case, an interpretation of less baseband equivalent bandwidth. Once they propagate together, an impulse response fluctuates even at very low frequency as in Fig. 64(b) and (c). However after a certain threshold ratio of coefficients, an impulse response restores closer back to its original dominant mode response in Fig. 64(d). To glimpse how badly it influences a signal integrity, an eye-diagram test is performed at a fixed data rate of 6Gb/s. In Fig. 65(a) and (b), an eye-diagram is almost completely closed, and it starts to open in Fig. 65(c) with 0.5 of coefficient for each mode. As proven in this study, a multimode propagation is highly undesirable for a high-speed data communication. To suppress a higher order mode propagation, one can reduce a radius of waveguide at a target carrier frequency, but it will reduce a bandwidth-capacity by pulling a notch frequency towards DC. By all means, however, it is better to suppress a multimode propagation; if not, at least the amount of presence should be limited as suggested in Fig. 65(d) and Fig. 65(d).

6.4 Air-Filled Metal Rectangular Waveguide

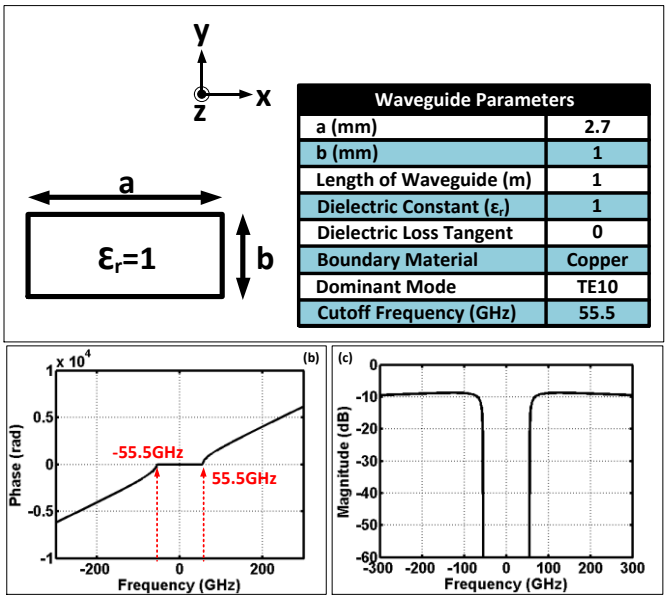

Waveguide Parameters	
a (mm)	2.7
b (mm)	1
Length of Waveguide (m)	1
Dielectric Constant (ε_r)	1
Dielectric Loss Tangent	0
Boundary Material	Copper
Dominant Mode	TE10
Cutoff Frequency (GHz)	55.5

Fig. 66. (a) Cross-section of air-filled metallic rectangular waveguide is shown with its propagation parameters. Wave propagates along z-direction. (b) Phase response. (c) Magnitude response.

An example of air-filled metal rectangular waveguide is presented in this section to demonstrate how easily a concept of impulse response applies to other types of waveguide. Just as a circular waveguide case, a rectangular waveguide parameter is summarized in Fig. 66 along with a phase and magnitude response. A dimension is decided to place a cutoff frequency at 55.5 GHz, which is close to the circular waveguide case (54.5 GHz). This time, a dielectric material is removed inside, so a loss factor primarily depends on a conductive loss. To summarize a waveguide property,

$$\text{Cutoff Wavenumber: } k_{c10} = \frac{\pi}{a} \tag{30}$$

$$\text{Propagation Constant: } \beta_{10} = \sqrt{k^2 - k_{c10}^2} \tag{31}$$

$$\text{Conductive Atten. Constant: } \sigma_c = \frac{R_S}{a^3 b k \eta \beta}(2b\pi^2 + a^3\pi^3) \tag{32}$$

$$\text{Cutoff Frequency: } \omega_{c10} = \frac{1}{a\sqrt{\mu\epsilon}} \tag{33}$$

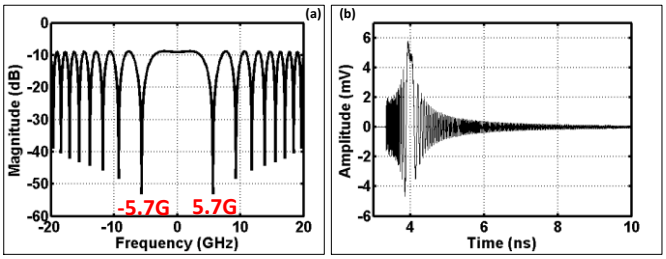

Fig. 67. (a) Baseband equivalent impulse response in frequency domain. (b) Baseband equivalent impulse response in time domain.

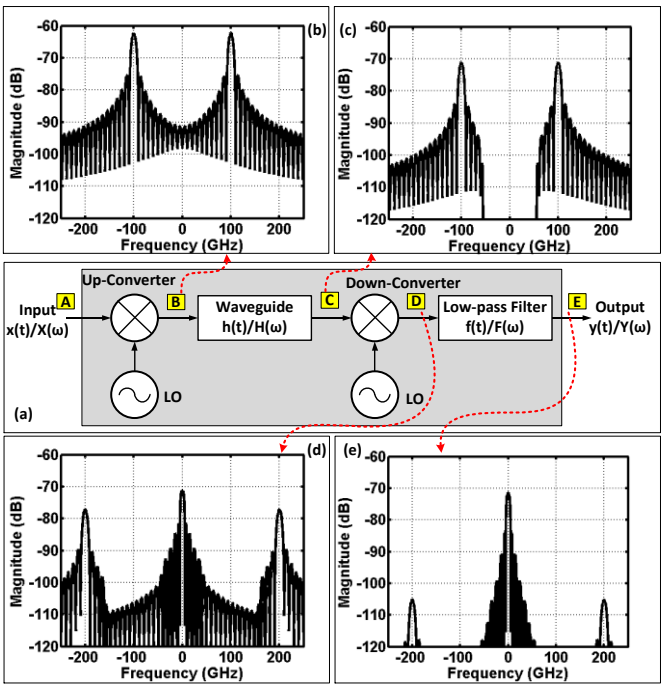

Fig. 68. (a) Block diagram. (b) Frequency domain modulated 100(ps) pulse with 100GHz carrier frequency. (c) Frequency domain modulated pulse after going through the waveguide. (d) Frequency domain down-converted baseband pulse with $2\omega_0$ residue. (e) Frequency domain baseband pulse after LPF.

Using relationships of (23), and (30) to (33) with a carrier frequency of 100 GHz, a baseband equivalent impulse response both in frequency domain and time domain is plotted in Fig. 67. A similar time domain simulation is performed as in Fig. 59, but in order to give a different perspective, each time domain signal is represented in frequency domain spectrum in Fig. 68. A single pulse with 100 ps width signal is up-converted using a 100 GHz carrier at node B, and it goes through a waveguide at node C. Notice the effect of cutoff to the modulated spectrum. After down-conversion, it generates both baseband and $2\omega_0$ spectral components, and an LPF extracts a baseband only at node D.

6.5 Conclusion

An impulse response method is introduced to analyze the information capacity of

waveguides for high-speed data communication applications. Traditional group delay variation methods can only predict pulse broadening effect when transmitted data bandwidth is narrow. Consequently, it does not fully reveal non-linear ISI effect corresponding to random baseband data sequences.

Instead, our newly proposed approach is able to capture complete non-linear behavior of baseband equivalent signal propagation under coherent communication system for any given waveguide geometry and carrier frequency, and produce impulse responses in both time and frequency domains.

Eye-diagrams are also finally constructed based on time domain impulse response for a random baseband bit sequence input, which is the most essential performance metric for quantifying data communication speed and bit error rate.

REFERENCES

[1] W. J. Dally, and J. W. Pulton, *Digital Systems Engineering*, Cambridge, 2008.

[2] E. Socher, and M.-C. F. Chang, "Can RF Help CMOS Processors?," *IEEE Communications Magazine*, vol. 45, no. 8, pp. 104–111, Aug. 2007.

[3] J. Kim, H. Hatamkhani, and C. K. Ken Yang, "A Large-Swing Transformer-Boosted Serial Link Transmitter With > VDD Swing," *IEEE J. Solid-State Circuits*, vol. 42, no. 5, pp. 1131–1142, May. 2007.

[4] Y. Tomita, M. Kibune, J. Ogawa, W. W. Walker, H. Tamura, and T. Kuroda, "A 10-Gb/s Receiver with Series Equalizer and On-Chip ISI Monitor in 0.11-µm CMOS," *IEEE J. Solid-State Circuits*, vol. 40, no. 4, pp. 986–993, Apr. 2005.

[5] J. Kim, S. Kim, W. Kim, J. Choi, H. Hwang, C. Kim, and S. Kim, "A 4-Gb/s/pin Low-Power Memory I/O Interface Using 4-Level Simultaneous Bi-Directional Signaling," *IEEE J. Solid-State Circuits*, vol. 40, no. 1, pp. 89–101, Jan. 2005.

[6] A. Amirkhani, A. Abbasfar, V. Stojanovic, and M. A. Horowitz, "Practical Limits of Multi-Tone Signaling Over High-Speed Backplane Electrical Links," *IEEE Int. Communications Conf.*, Jun. 2007, pp. 2693–2698.

[7] M.-C. F. Chang, V. P. Roychowdhury, L. Zhang, H. Shin, and Y. Qian, "RF/Wireless Interconnect for Inter- and Intra-Chip Communications," *IEEE Proceedings*, vol. 89, no. 4, pp. 456–466, Apr. 2001.

[8] S. W. Tam, E. Socher, A. Wong, and M.-C. F. Chang, "A Simultaneous Tri-Band On-Chip RF-Interconnect for Future Network-on-Chip," *IEEE VLSI Symposium on VLSI Circuits*, pp. 90–91, Jun 2009.

[9] Z. Xu, H. Shin, J. kim, M.-C. F. Chang, and C. Chien, "A 2.7Gb/s CDMA-Interconnect Transceiver Chip Set with Multi-Level Signal Data Recovery for Re-configurable VLSI Systems," *IEEE ISSCC Dig. Tech. Paper*, 2003, pp. 322–323.

[10] J. Ko, J. Kim, Z. Xu, Q. Gu, C. Chien, and M.-C. F. Chang, "An RF/Baseband FDMA-Interconnect Transceiver for Reconfigurable Multiple Access Chip-to-Chip Communication," *IEEE ISSCC Dig. Tech. Paper*, 2005, pp. 338–339.

[11] M.-C. F. Chang, J. Cong, A. Kaplan, M. Naik, G. Reinman, E. Socher, and S. W. Tam, "CMP Network-on-Chip Overlaid with Multi-band RF-interconnect," *IEEE 14th Int. Symposium on HPCA*, pp. 191–202, Feb. 2008.

[12] G. Byun, Y. Kim, J. Kim, S. W. Tam, H. H. Hsieh, P. Y. Wu, C. Jou, J. Cong, G. Reinman, and M.-C. F. Chang, "An 8.4Gb/s 2.5pJ/b Mobile Memory I/O Interface Using Simultaneous Bidirectional (Base+RF) Band Signaling," *IEEE ISSCC Dig. Tech. Papers*, 2011, pp. 488–490.

[13] G. Byun, Y. Kim, J. Kim, S. W. Tam, and M.-C F. Chang, "An Energy-Efficient and High-Speed Mobile Memory I/O Interface Using Simultaneous Bi-Directional Dual (Base+RF)-Band Signaling," *IEEE J. Solid-State Circuits*, vol. 47, no. 1, pp. 1–14, Jan. 2012.

[14] Y. Kim, G. Byun, A. Tang, C. P. Jou, H. H. Hsieh, G. Reinman, J. Cong, and M.-C. F. Chang, "An 8Gb/s/pin 4pJ/b/pin Single-T-Line Dual (Base+RF) Band Simultaneous Bidirectional Mobile Memory I/O Interface with Inter-Channel Interference Suppression," *IEEE ISSCC Dig. Tech. Papers*, 2012, pp. 50–51.

[15] J. Kennedy, R. Mooney, R. Ellis, J. Jaussi, S. Borkar, J. Choi, J. Kim, C. Kim, W. Kim, C. Kim, S. Cho, S. Loeffler, J. Hoffmann, W. Hokenmaier, R. Houghton, and T. Vogelsang, "A 3.6-Gb/s point-to-point heterogeneous-voltage-capable DRAM interface for capacity-

scalable memory subsystems," *IEEE J. Soild-State Circuits*, vol. 40, no. 1, pp. 233–244, Jan. 2005.

[16] B. Leibowitz, R. Palmer, J. Poulton, Y. Frans, S. Li, J. Wilson, M. Bucher, A. M. Fuller, J. Eyles, M. Aleksic, T. Greer, and N. M. Nguyen, "A 4.3 GB/s Mobile Memory Interface With Power-Efficient Bandwidth Scaling," *IEEE J. Solid-State Circuits*, vol. 45, no. 4, pp. 889–898, Apr. 2010.

[17] A. Tomkins, R. A. Aroca, T. Yamamoto, S. T. Nicolson, Y. Doi, S. P. Voinigescu, "A Zero-IF 60 GHz 65 nm CMOS Transceiver With Direct BPSK Modulation Demonstrating up to 6 Gb/s Data Rates Over a 2 m Wireless Link," *IEEE J. Solid-State Circuits*, vol. 44, no. 8, pp. 2085–2099, Aug. 2009.

[18] B. P. Lathi, and Z. Ding, *Modern Digital and Analog Communication Systems,* 4th ed. Oxford, 2009.

[19] H. Wang, M. Hung, Y. Yeh, and J. Lee, "A 60-GHz FSK Transceiver with Automatically-Calibrated Demodulator in 90-nm CMOS," *IEEE VLSI Symposium on VLSI Circuits*, pp. 95–96, Sep. 2010.

[20] F. Xiong, *Digital Modulation Techniques,* 2nd ed. Boston/London: Artech House, 2006.

[21] B. Razavi, RF Microelectronics, 2nd ed. Prentice Hall, 2011

[22] D. M. Pozar, Microwave Engineering, 3rd ed. Wiley, 2005

[23] K. Oh, L. Kim, K. Park, Y. Jun, J. Choi, and K. Kim, "A 5-Gb/s/pin Transceiver for DDR Memory Interface With a Crosstalk Suppression Scheme," *IEEE J. Solid-State Circuits*, vol. 44, pp. 2222–2232, Aug. 2009.

[24] K. Ha, K. Kim, S. Bae, K. Park, J. Choi, Y. Jun, and K. Kim, "A 6Gb/s/pin Pseudo-Differential Signaling Using Common-Mode Noise Rejection Techniques Without Reference Signal for DRAM Interfaces," *IEEE ISSCC Dig. Tech. Papers*, pp. 138–139, Feb. 2009.

[25] B. Saltzberg, "Performance of an Efficient Parallel Data Transmission System," *IEEE Transactions on Communications*, vol. 15, no. 6, pp. 805-811, 1967.

[26] D. H. Morgen, "Expected Crosstalk Performance of Analog Multichannel Subscriber Carrier Systems," *IEEE Transactions on Communications*, vol. 23, no. 2, pp, 240-245, 1975.

[27] S. V. Ahamed, P. P. Bohn, and N. L. Gottfried, "A Tutorial on Two-Wire Digital Transmission in the Loop Plant," *IEEE Transactions on Communications*, vol. 28, no. 11, pp. 1554-1564, 1981.

[28] P. S. Chow, J. C. Tu,, and J. M. Cioffi, "Performance Evaluation of a Multichannel Transceiver System for ADSL and VHDSL Services," *IEEE Journal on Selected Areas in Communications*, vol. 9, no. 6, pp. 909-917, 1991.

[29] P. S. Chow, J. M. Cioffi, and J. A. C. Bingham, "A Practical Discrete Multitone Transceiver Loading Algorithm for Data Transmission Over Spectrally Shaped Channels," *IEEE Transactions on Communications*, vol. 43, no. 2, pp. 773-775, 1995.

[30] M. Barton, L. Chang, and T. R. Hsing, "Performance Study of High-Speed Asymmetric Digital Subscriber Lines Technology," *IEEE Transactions on Communications*, vol. 44, no. 2, pp. 156-157, 1996.

[31] A. Amirkhany, V. Stojanovic , and M. A. Horowitz, "Multi-tone Signaling for High-Speed Backplane Electrical Links," *IEEE GLOBECOM*, vol. 2, pp. 1111-1117, 2004.

[32] T. Sartenaer, L. Vandendorpe, and J. Louveaux, "Balanced Capacity of Wireline Multiuser Channels," *IEEE Transactions on Communications*, vol 53, no. 12, pp. 2029-2042, 2005.

[33] Q. Gu, Z. Xu, J. Kim, J. Ko, and M. C. F. Chang, "Three-Dimensional Circuit Integration Based on Self-Synchronized RF-Interconnect Using Capacitive Coupling," *IEEE Symposium on VLSI Technology and Circuits*, 2004.

[34] G. Byun, Y. Kim, J. Kim, S. W. Tam, J. Cong, G. Reinman, M.C.F. Chang, "An 8.4Gb/s 2.5pJ Mobile Memory I/O Interface Using Bi-directional and Simultaneous Dual (Base+RF)-Band Signaling," *IEEE Solid-State Circuits Conference*, 2011.

[35] Y. Kim, G. Byun, A. Tang, C. Jou, H. Hsien, G. Reinman, J. Cong, and M.C.F. Chang, "An 8Gb/s/pin 4pJ/b/pin Single-T-Line Dual (Base+RF) Band Simultaneous Bidirectional Mobile Memory I/O Interface," *IEEE International Solid-State Circuits Conference*, 2012.

[36] M. Jalalifar and G. Byun, "A 14.4Gb/s/pin 230fJ/b/pin/mm Multi-Level RF-Interconnect for Global Network-on-Chip Communication," *IEEE Asian Solid-State Circuits Conference*, 2016.

[37] Y. Kim, S. Tam, G. Byun, H. Wu, L. Nan, G. Reinman, J. Cong, M. C. F. Chang, "Analysis of Noncoherent ASK Modulation-Based RF-Interconnect for Memory Interface," *IEEE journal on Emerging and Selected Topics in Circuits and Systems*, vol. 2. no. 2, pp. 200-209, 2012.

[38] S. Ibrahim, and B. Razavi, "Design Requirements of 20-Gb/s Serial Links Using Multi-Tone Signaling," *IEEE International Symposium on Circuits and Systems*, 2009.

[39] W. Cho, Y. Li, Y. Kim, P. Huang, Y. Du, S. Lee, and M. C. F. Chang, "A 5.4mW 4-Gb/s 5-Band QPSK Transceiver for Frequency-Division Multiplexing Memory Interface," *IEEE Custom Integrated Circuits Conference*, 2015.

[40] W. Cho, Y. Li, Y. Du, C. Wong, J. Du, P. Huang, S. Lee, H. Chen, C. Jou, F. Hsueh, and M. C. F. Chang, "A 38mW 40Gb/s 4-Lane Tri-Band PAM-4/16-QAM Transceiver in 28nm CMOS for High-Speed Memory Interface," *IEEE Solid-State Circuits Conference*, 2016.

[41] Y. Du, W. Cho, Y. Li, C. Wong, J. Du, P. Huang, Y. Kim, Z. Chen, S. Lee, and M.C.F. Chang, "A 16Gb/s 14.7mW Tri-Band Cognitive serial Link Transmitter with Forwarded Clock to Enable PAM-16/256-QAM and Channel Response Detection in 28nm CMOS," *IEEE Symposium on VLSI Circuits*, 2016.

[42] K. Gharibdoust, A. Tajalli, and Y. Leblebici, "Hybrid NRZ/Multi-Tone Serial Data Transceiver for Multi-Drop Memory Interfaces," *IEEE Journal of Solid-State Circuits*, vol. 50, no. 12, pp.3133-3144, 2015.

[43] K. Gharibdoust, A. Tajalli, and Y. Leblebici, "A 4x9Gb/s 1pJ/b Hybrid NRZ/Multi-Tone I/O With Crosstalk and ISI Reduction for Dense Interconnects," *IEEE Journal of Solid-State Circuit*, vol. 51, no. 4, pp. 992-1002, 2016.

[44] Y. Kim, L. Nan, J. Cong, and M. C. F. Chang, "High-Speed mm-Wave Data-Link based on Hollow Plastic Cable and CMOS Transceiver," *IEEE Microwave and Wireless Components Letter*, vol. 23. no. 12, pp. 674-676, 2013.

[45] Y. Frans, S. McLeod, H. Hedayati, M. Elzeftawi, J. Namkoong, W. Lin, J. Im, P. Upadhyaya, and K. Chang, "A 40-to-60Gb/s NRZ Transmitter With Supply-Regulated Front-End in 16nm FinFET," *IEEE Journal of Solid State Circuits*, vol. 51, no. 12, pp. 3167-3177, 2016.

[46] M. Bassi, F. Radice, M. Bruccoleri, S. Erba, and A. Mazzanti, "A High-Swing 45Gb/s Hybrid Voltage and Current-Mode PAM-4 Transmitter in 28nm CMOS FDSOI," *IEEE Journal of Solid State Circuits*, vol 51, no. 11, pp. 2702-2715, 2016.

[47] J. Han, Y. Lu, N. Sutardja, K. Jung, and E. Alon, "Design Techniques for a 60Gb/s 173mW Wireline Receiver Frontend in 65nm CMOS Technology," *IEEE Journal of Solid State Circuits*, vol. 51, no. 4, pp. 871-880, 2016.

[48] N. Kocaman, T. Ali, L. Rao, U. Singh, M. Abdul-Latif, Y. Liu, A. Hafez, H. Park, A. Vasani, Z. Huan, A. Iyer, B. Zhang, and A. Momtaz, "A 3.8mW/Gbps Quad-Channel 8.5-13Gbps Serial Link With a 5 Tap DFE and a 4 Tap Transmit FFE in 28nm CMOS," *IEEE Journal of Solid State Circuits*, vol. 41, no. 4, pp. 881-892, 2016.

[49] Y. Du, W. Cho, P. Huang, Y. Li, C. Wong, J. Du, Y. Kim, B. Hu, L. Du, C. Liu, S. J. Lee, and M. C. F. Chang, "A 16-Gb/s 14-mW Tri-Band Cognitive Serial Link Transmitter With Forwarded Clock to Enable PAM-16/256-QAM and Channel Response Detection," *IEEE Journal of Solid State Circuits*, vol. no. pp. 2016.

[50] D. Wang, B. Jacob, and S. Ng, "Memory Systems: Cache, DRAM, Disk," *Morgan Kaufmann*, 2008.

[51] D. G. Kam and J. Kim, "40-Gb/s Package Design Using Wire-Bonded Plastic Ball Grid Array," *IEEE Transactions on Advanced Packaging*, vol. 31, no. 2, pp. 258-266, 2008.

[52] K. Kawasaki, *et al.*, "A Millimeter-Wave Intra-Connect Solution," *IEEE Journal of Solid-State Circuits*, vol. 45, no. 12, pp. 2655-2664 2010.

[53] N. K. Das, *et al*., "Two Methods for the Measurement of Substrate Dielectric Constant," *IEEE Transactions on Microwave Theory and Techniques*, vol. 35, no. 7, 1987

[54] Delong Cui, et al., "A Dual 23Gb/s CMOS Transmitter/Receiver Chipset for 40Gb/s RZ-DQPSK and CS-RZ-DQPSK Optical Transmission," *ISSCC Dig. Tech. Papers*, pp. 330-331, Feb. 2012.

[55] Intersil Corporation, "piDesigning Next-Generation 40nm Active Cable Solutions to Support Thunderbolt™ Technology," White Paper, May. 2012.

[56] Tarun Gupta, et al., "A Sub-2W 10GBASE-T Analog Front-End in 40nm CMOS Process," *ISSCC Dig. Tech. Papers*, pp. 410-411, Feb. 2012.

[57] Yusuke Tanaka, et al., "A Versatile Multi-Modality Serial Link," *ISSCC Dig. Tech. Papers*, pp. 332-333, Feb. 2012.

[58] C. Yeh and F.I. Shimabukuro, "The Essence of Dielectric Waveguides," Springer 2008.

[59] Mitsunobu Miyagi and Shigeo Nishida, "Transmission Characteristics of Dielectric Tube Leaky Waveguide," *IEEE Transactions on Microwave Theory and Techniques*, Vol. 28, No. 6, pp. 536-541, Jun. 1980.

[60] C. Yeh, *et al*., "Low-loss Terahertz Ribbon Waveguide," *Applied Optics*, vol. 44, no. 28, pp. 5937-5946, 2005.

[61] W. Volkaerts, *et al.*, "An FSK Plastic Waveguide Communication Link in 40nm CMOS," *IEEE Int. Solid-State Circuits Conf.*, pp. 1-3, 2015.

[62] M. N. Afsar, "Precision Dielectric Measurements of Nonpolar Polymers in the Millimeter Wavelength Range," *IEEE Transactions on Microwave Theory and Techniques*, vol. 33, no. 12, 1985.

[63] W. M. Bruno, *et al*., "Flexible Dielectric Waveguides with Powder Cores," *IEEE Transactions on Microwave Theory and Techniques*, vol. 36, no. 5, pp. 882-890, 1988.

[64] H. Asao, *et al.*, "Metal-Plated Plastic Waveguide Filter Using Injection Molding Process," *IEEE International Microwave Symposium*, 2003.

[65] R. Zhu, *et al.*, "Rapid Prototyping Lightweight Millimeter Wave Antenna and Waveguide with Copper Plating," *International Conference on Infrared, Millimeter, and Terahertz Waves*, 2015.

[66] H. I. Song, *et al.*, "Plastic Straw: Future of High-Speed Signaling," *Nature-Scientific Report*, no. 16062, 2015.

[67] Y. Tanaka, Y. Hino, Y. Okada, T. Takeda, S. Ohashi, H. Yamagishi, K. Kawasaki, and A. Hajimiri, "A Versatile Multi-Modality Serial Link," *IEEE Int. Solid-State Circuits Conf.*, pp. 331-332, 2012.

[68] H. I. Song, H. Jin, and H. M. Bae, "Plastic Straw: Future of High-Speed Signaling," *Nature-Scientific Report*, no. 16062, 2015.

[69] F. P. Kapron and D. B. Keck, "Pulse Transmission through a Dielectric Optical Waveguide," *Applied Optics*, vol. 10, no. 7, pp. 1519-1523, 1971.

[70] N. Dolatsha, C. Chen, and A. Arbabian, "Loss and Dispersion Limitations in mm-Wave Dielectric Waveguides for High-Speed Links," *IEEE Transactions on Terahertz Science and Technology*, vol. 6, no. 4, 2016.

[71] K. Azadet, E. F. Haratsch, H. Kim, F. Saibi, J. H. Saunders, M. Shaffer, L. Song, and M. L. Yu, "Equalization and FEC Techniques for Optical Transceivers," *IEEE Journal of Solid State Circuits*, vol. 37, no. 3, pp. 317-327, 2002.

[72] M. Maeng, F. Bien, Y. Hur, H. Kim, S. Chandramouli, E. Gebara, and J. Laskar, "0.18-um CMOS Equalization Techniques for 10-Gb/s Fiber Optical Communication Links," *IEEE Transactions on Microwave Theory and Techniques*, vol. 53, no. 11, pp. 3509-3519, 2005.

[73] S. Gondi and B. Razavi, "Equalization and Clock and Data Recovery Techniques for 10-Gb/s CMOS Serial-Link Receivers," *IEEE Journal of Solid State Circuits*, vol. 42, no. 9, pp. 1999-2011, 2007.

[74] D. Gloge, "Impulse Response of Clad Optical Multimode Fibers," *The Bell System Technical Journal*, vol. 52, no. 6, 1973.

[75] J. W. Dannwolf, S. Gottfried, G. A. Sargent, and R. C. Strum, "Optical-Fiber Impulse-Response Measurement System," *IEEE Transactions on Instrumentation and Measurement*, vol. 25, no. 4, pp. 401-406, 1976.

[76] K. Okamoto, "Comparison of Calculated and Measured Impulse Responses of Optical Fibers," *Applied Optics*, vol. 18, no. 13, pp. 2199-2206, 1979.

[77] M. R. Chatterjee, and L. S. Green, "Derivation of Impulse Response and Transfer Function of an Optical Fiber Under Chromatic Dispersion and Application to a Linear Fiber-Optic Communication System," *IEEE Southern Tier Technical Conf.*, pp. 209-216, 1990

[78] R. E. Collins, "Field Theory of Guided Waves," *Wiley*, 2nd Ed., 1990.

[79] W. A. Imbriale, T. Y. Otoshi, and C. Yeh, "Power Loss for Multimode Waveguides and Its Application to Beam-waveguide System," *IEEE Transactions on Microwave Theory and Techniques*, vol. 46, no. 5, pp. 523-529, 1998.